Los Alamos National Laboratory

ACTINIDE RESEARCH QUARTERLY

2016

89 Ac | 90 Th | 91 Pa | 92 U | 93 Np | 94 Pu | 95 Am | 96 Cm | 97 Bk | 98 Cf | 99 Es | 100 Fm | 101 Md | 102 No | 103 Lr

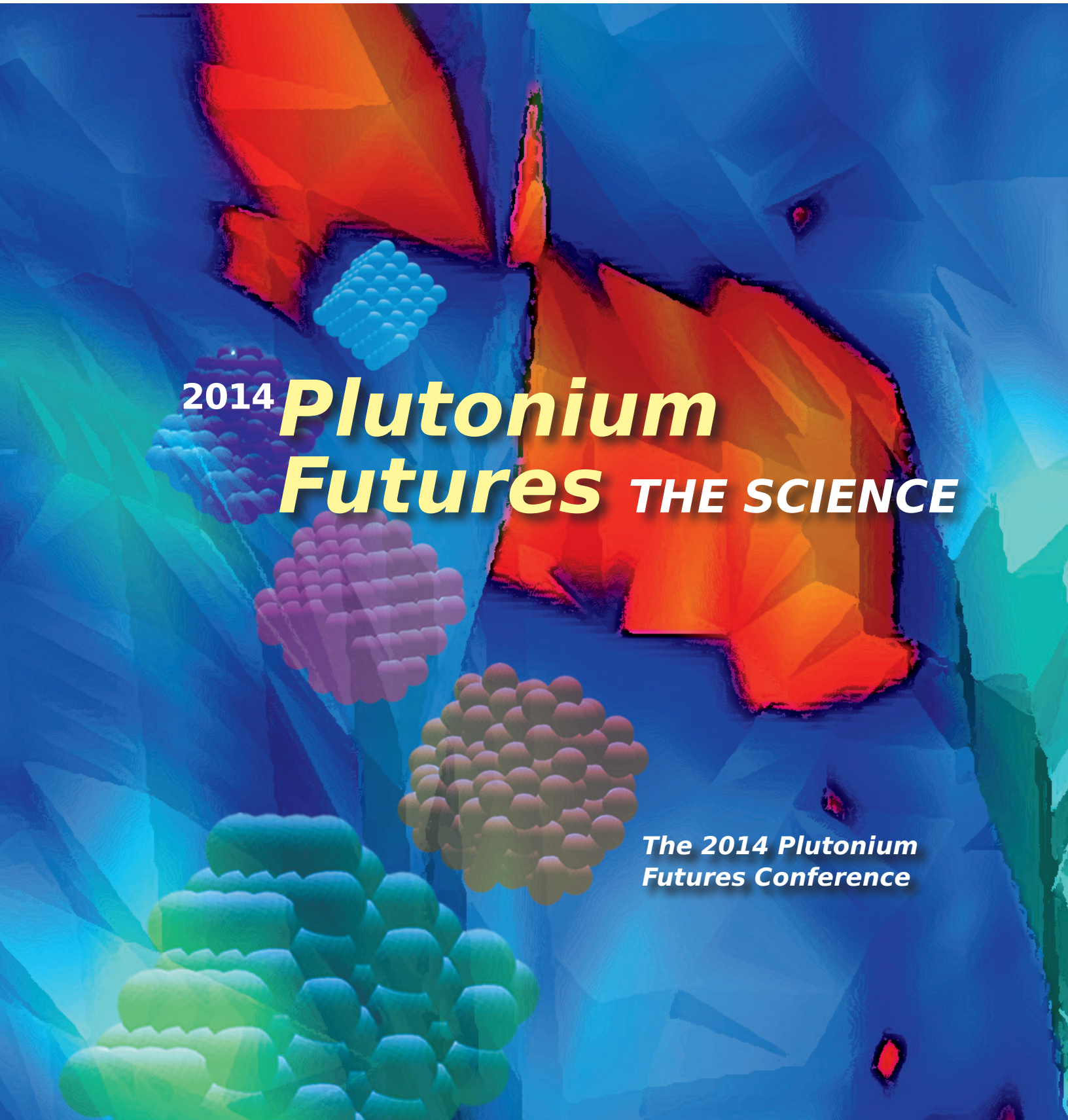

2014 Plutonium Futures THE SCIENCE

The 2014 Plutonium Futures Conference

Kerri Blobaum
General Chair, Plutonium Futures—
The Science 2014
Lawrence Livermore National Laboratory

ELEMENT 94: THE EIGHTH PLUTONIUM FUTURES—THE SCIENCE CONFERENCE

The Eighth Plutonium Futures—The Science conference was held at the Renaissance Hotel in Las Vegas, Nevada, on September 7–12, 2014. More than 230 attendees from 13 countries participated in talks and discussions centered around the latest scientific research on Element 94, as well as other closely related actinide materials.

This conference's success was the result of the hard work of many people from national laboratories, academia, and industry worldwide. These people helped select speakers and assembled the oral presentations and poster sessions. The conference was sponsored by the American Nuclear Society, whose staff did an excellent job arranging all the conference's logistics. In addition, Lawrence Livermore National Laboratory and Los Alamos National Laboratory served as conference cosponsors.

The 2014 conference focused on eight topical areas:

- Environmental Science
- Condensed Matter Physics
- Solutions and Gas-Phase Chemistry
- Metallurgy and Materials Science
- Compounds, Complexes, and Coordination Chemistry
- Nuclear Fuel Cycle
- Detection and Analysis
- Surface Science and Corrosion

Highlights from these sessions are featured as articles in this issue of *Actinide Research Quarterly*.

The conference opened with a tutorial session led by Brian Powell from Clemson University ("An Overview of Biogeochemical Reactions Controlling Pu Environmental Mobility"), Albert Migliori from Los Alamos National Laboratory ("Pu—Some Interesting Aspects of Thermodynamics and Electronic Structure"), and Andreas Kronenburg from the International Atomic Energy Agency ("Nuclear Fuels in the Eyes of a Radiochemist"). A Welcome Reception held at the National Atomic Testing Museum gave attendees an opportunity to view a collection of more than 12,000 unique artifacts related to nuclear research, development, and testing.

The conference's guest speaker for the conference banquet was Bruce Held, Associate Deputy Secretary of Energy and former clandestine operations officer for the Central Intelligence Agency. His talk, "A Spy's Admiration for Scientists and National Laboratories," was a hit with the audience!

The conference concluded with a daylong tour of the Nevada National Security Site (NNSS), formerly known as the Nevada Test Site. Attendees had the opportunity to see several well-known sites, including Mercury camp, the Sedan crater, and the Device Assembly Facility. Excellent tour guides on the buses provided commentary based on their own careers working at the NNSS.

The Plutonium Futures conference series was initiated by scientists at Los Alamos National Laboratory, with the first meeting held in 1997 in Santa Fe, New Mexico. Since then, meetings have been held in Albuquerque, New Mexico; Asilomar, California; Dijon, France; Keystone, Colorado; and Cambridge, England. The conference is organized by an International Advisory Committee, with the primary responsibility assumed by the local host. This ensures that the conference attracts researchers from around the globe and that each conference has its own international flair.

We look forward to seeing you at the next Plutonium Futures—The Science conference in Baden, Germany (September 18–22, 2016)!

Prepared by Lawrence Livermore National Laboratory under Contract DE-AC52-07NA27344.

In this issue

About the cover

The intriguing chemistry, physics, and engineering properties of plutonium are dictated primarily by its crystalline and electronic structure in elemental, molecular, and compound forms. In the foreground are colored balls stacked according to the crystalline symmetry of five solid allotropes of elemental plutonium. The background image is an intensity colormap showing "hotspots" on the electronic structural Fermi surfaces of $PuCoGa_5$. These hotspots are caused by electron scattering with magnetic spin fluctuations, a combination that generates a condition known as nesting, which may account for the material's superconductivity.

Brightening the Future of Plutonium Science by Rooting Out Assumptions Taken as Fact and Eliminating Selective Use of Inconvenient Results

Albert Migliori
G. T. Seaborg Institute
Los Alamos National Laboratory

Albert Migliori notes that plutonium's ongoing challenges are what makes this element the most interesting one after helium.

Although the experimental and computational tools scientists use today to study plutonium would seem like magic to physicists like Willy Zachariasen, plutonium science remains as complex as ever. It is not unreasonable to consider plutonium as the most interesting element after helium in its challenge to our understanding.

But what is it that we do not understand? Well, for one, the phases of plutonium—it has six, or is it five? Why the question? Why does pure δ plutonium contract when warmed—and why does it concurrently become more compressible? The phase diagram of gallium-stabilized face-centered cubic (fcc) δ plutonium—is it really stable at 300 K as Zachariasen asserted, or not, as our Russian colleagues think?

And what kinds of messes does radiation damage make of our attempts to make well-crafted measurements on a material that ages noticeably before the eyes of modern experimental capabilities? There are many, but let's explore only a few in some detail.

Phases

One reason plutonium is so interesting is that its complex 5*f* electron orbitals enable many thermodynamic phases. For our purposes, we consider a phase to be characterized by a particular arrangement of plutonium atoms that is a minimum of the free energy. It results from tension between the increasing number of configurations possible as temperature rises (which determines the entropy), against the Boltzmann-factor-driven lower probability of higher energy states.

Plutonium's many phases cannot exist without the entropy driver that accompanies increasing temperature. Why then is it expected for *ab initio* electronic structure computations to be applicable, given that such computations are always zero-temperature theories and were not possible without modern massive computational power? Although the low-temperature α phase appeared to yield nicely to this approach, the all-important higher temperature δ phase did not. This is analogous to a man looking for his wallet under a streetlight, even though he lost it down the road while in the dark.

In 1995, Per Soderlind and team at Lawrence Livermore National Laboratory used density functional theory to find computational solutions (plural) to the structure of plutonium metal. These solutions included magnetism, even though magnetism had not been previously observed. The multiple solutions would prove to be important.

A few years later, Angus Lawson—while working with Franz Trouw and his team, just barely observed the weakest signs of magnetic scattering in plutonium. From this observation, Lawson made an important conjecture: Finally incorporating the rather inconvenient measurement of Migliori and team of the softening of the elastic stiffness of δ plutonium as it contracted, opposite what almost everything else does, Lawson compared plutonium to Invar, a zero-thermal-expansion magnetic alloy that garnered Charles-Edouard Guillaume a Nobel prize in 1915 for its discovery. The mechanism required for explaining Invar required two magnetic states. Although both states were each ordinary in behavior, rising temperature meant that the higher energy state became more populated, with the properties of the alloy gently crossing over from those of one state to those of the other. Lawson was able at least to model the negative thermal expansion of δ plutonium, as well as the softening upon warming, but the magnetism was just not convincingly there.

Fast forward to 2015. Marc Janoschek at Los Alamos National Laboratory used neutrons to perform some gorgeous measurements that showed reasonably clearly for the first time two magnetic states in plutonium. However—still looking under the streetlight—calculations from the dynamical mean field theory (a theory more appropriate to relatively isolated atoms than good metals) applied to this result failed to accommodate both negative thermal expansion and the accurately observed softening upon warming. Nevertheless, these measurements may finally lead to important insights for the most mysterious δ phase.

What about plutonium's other phases? In Fig. 1, the δ' phase is rather weird. This phase becomes weirder still when it becomes clear that the abrupt (first order) thermodynamic phase changes require latent heat. However, the latent heat listed in the 1967 *Plutonium Handbook* for the δ' transition is zero! Although later work did show some signs of latent heat, it was small and not sharp in temperature. Thus, the most important indicator of a true thermodynamic phase seems to be missing. What else could it be?

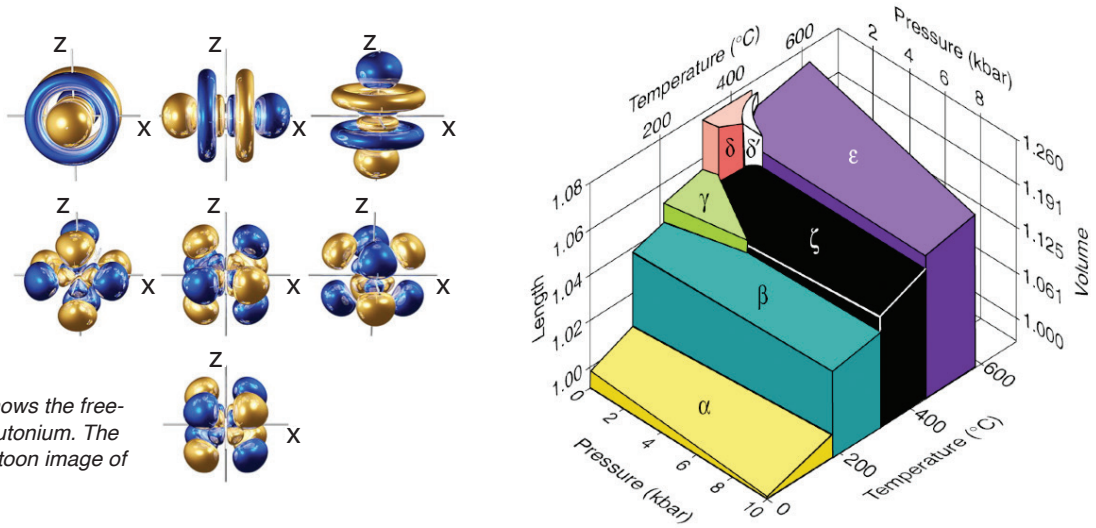

Fig. 1. The figure on the left shows the free-space 5f electron orbitals of plutonium. The figure on the right shows a cartoon image of its thermodynamic phases.

In 1973, Hassel Ledbetter and Roger Moment grew an astounding 7-mm-long single crystal of gallium-stabilized δ plutonium, a feat never repeated despite many modern attempts. Using an ultrasonic technique, the duo found that not only is δ plutonium softer than lead, its is even softer along a diagonal to the cubic axes. In fact, it has what is called a shear anisotropy greater than that of any other fcc metal. Such anisotropy is just the ticket to enable a very small force to push fcc δ plutonium into a body-centered tetragonal (bct) shape, as shown in Fig. 2. If thermodynamics can only drive fcc δ plutonium to body-centered cubic (bcc) ε plutonium, then as parts of the solid transform a huge compressive strain field develops that pushes fcc plutonium to bct plutonium until the transformation is complete. Thus, δ' plutonium might be an artifact of the uniquely and anisotropically soft δ plutonium.

Looking back on Zachariasen's x-ray measurments, we find that the x-ray diffraction data indicating the existence of δ' plutonium is an order of magnitude less precise than that for any other phase, further suggesting that δ' is an artifact. Finally, we note that δ plutonium is a close packed (fcc) or very dense structure, even though it has the lowest density of any plutonium phase. It seems from this that plutonium does not care about its volume. Morevoer, plutonium in its fcc phase finds an energy state that has an intrinsically large volume, although the element does its best to minimize such an effect by choosing a closely packed structure. Noting Janoschek's magnetic observation that seems to indicate two magnetic states for plutonium, maybe the driver for phases changes is not vibration entropy at all—perhaps it is *magnetic* entropy.

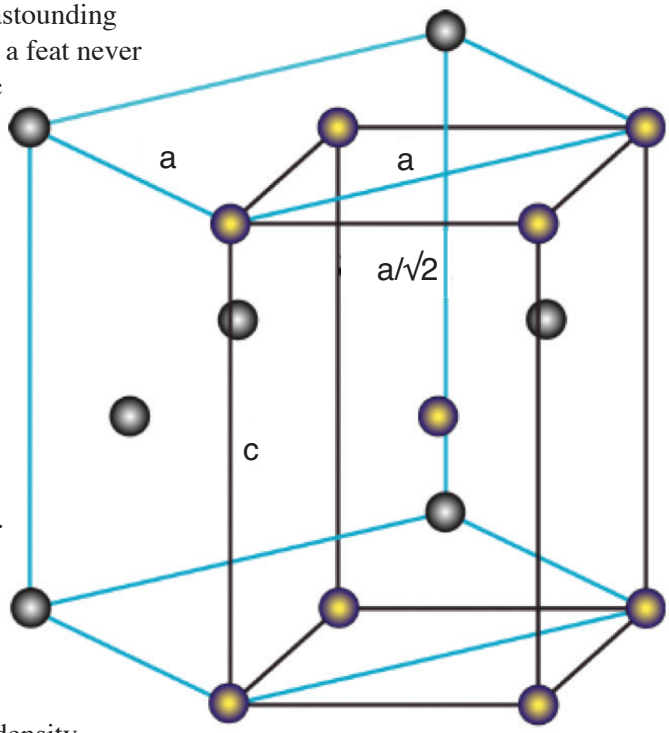

Fig. 2. This illustration shows how a face-centered cubic structure (blue) can easily morph into a body-centered tetragonal and then into a body-centered cubic structure (black) with just a little (vertical) squeezing. This is called a Bain path.

Alloy Stability

The all-important stability of gallium-stabilized δ plutonium seems to be just another area where Russia and the US disagree these days (Fig. 3). Adding a percent or so of gallium to plutonium seems to stabilize δ plutonium so that this ductile and easily worked phase can exist at 300 K. However, Russian studies contradict this.

To understand what this is about, consider that compressing δ-Pu + Ga should lead toward a higher density, which is α-Pu with a little Pu_3Ga. If heated when compressed, it makes this process even easier because the gallium can diffuse better. Thus, compressing and heating gallium-stabilized δ plutonium could drive a phase separation not possible under ambient conditions. However, this process is exactly what the Russian experiment did to bring into question the stability at room temperature of gallium-stabilized δ plutonium.

Harken back half a century to the work of Hunter Hill at Los Alamos. He showed that transforming pure plutonium among its phases as temperature changed could take weeks or even longer. Presumably, such slow kinetics is

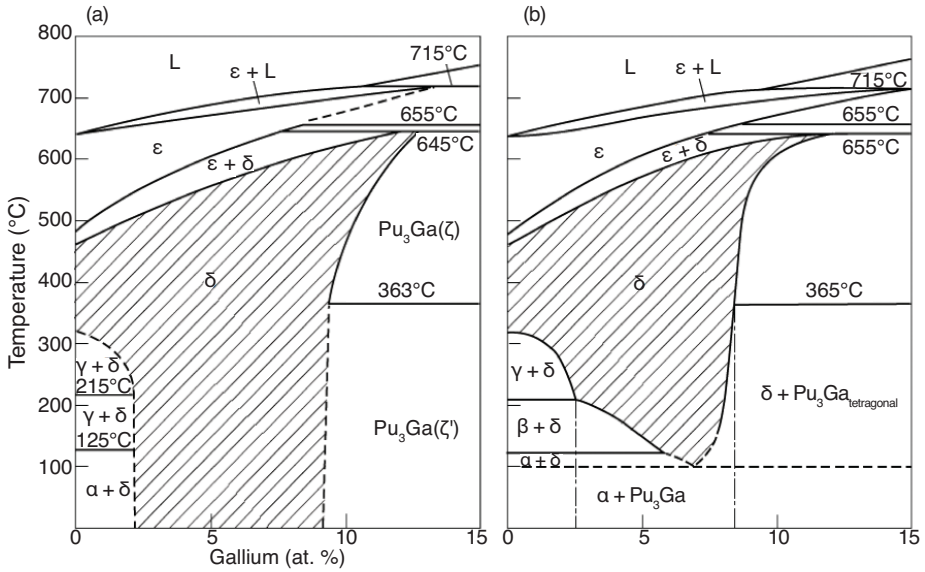

Fig. 3. The U.S. phase diagram for gallium-stabilized δ plutonium (left) and the Russian diagram (right) differ in that the Russians find δ plutonium to be unstable at 300 K.

associated with the delicate electronic structure and small energy differences among phases. Thus, forcing a destabilization of δ plutonium with temperature and pressure, combined with slow kinetics, seems a bad way to study the phase diagram. So, if this were the procedure to draw conclusions about phase stability, why would we think gallium-stabilized δ plutonium is metastable at ambient temperature? Recent measurements of the elastic stiffness with 10 parts-per-billion in sensitivity may vindicate the U.S.

Radiation and Aging

Coloring all the increasingly more accurate research into ^{239}Pu is the issue of radiation effects and "aging." This plutonium isotope is the most important because it is used in nuclear weapons and for nuclear energy. Its main decay mode is into an 86-keV uranium and a 5-MeV helium, with some 10s of keV into gamma rays. Now, consider a perfect single crystal of the mass 239 isotope of δ plutonium stabilized with 2 at.% gallium, a common room-temperature-stable (300 K) alloy. There is a lot going on.

If we imagined our crystal to be a leaky bucket, then what is in the bucket is everything that is not either a plutonium atom exactly in its correct crystallographic position or a perfectly and randomly placed gallium atom. Thus, we try to ignore everything that is not considered a "defect."

One typically ignored but important defect takes place when a plutonium atom is thermally displaced as a result of 300 K of thermal energy. It is this same thermal energy that anneals away these defects. Thus, the continious thermally activated generation and annealing of point defects ensures a steady-state defect density that rises with temperature. Room temperature is not low—it is approximately one-third of the melting temperature.

Compounding this issue are the effects of radioactive decay. The exponential decay constant for ^{239}Pu is 1.095×10^{12} seconds, corresponding to about a 24,000-year half-life. So, consider our bucket to have 10^{21} atoms of ^{239}Pu, approximately a 6-mm sphere. Each second,

10^9 atoms decay, dumping very near the decay event the 86 keV of recoil energy of the uranium, a uranium atom, and a helium atom (alpha particle). Using the very crudest estimates for heat capacity—and turning off our thinking caps—that single decay has enough energy to raise 10^6 plutonium atoms surrounding the event to above the 900 K melting point of plutonium. In approximately two weeks, every single plutonium atom has been above the melting point of plutonium about once—this creates a lot of damage.

So, is it more than the ordinary thermally activated defect density? This is an essential question for which we have little in the way of answers. Not only does the temperature rise activate any thermodynamic drivers for phase transitions, it also leaves behind forever the uranium and the helium. Thus, radioactive decay leaves behind defects, drives thermodynamics with local heating, and leaves uranium and helium atoms as impurities.

Consider for a moment the defects. Some of the radiation damage might be conjectured to look like ordinary thermally activated defects. One defect might be a vacancy (a component of so-called Freckel pairs). What is the vacancy's mobility? Can such a vacancy find another vacancy nearby and form a bigger one? Why does this not happen with thermal effects?

If a vacancy finds an interstitual plutonium (which likely is much more mobile than the vacancy), then it simply disappears. However, there are many more well-known types of radiation-induced defects. For example, amorphization is present at lower temperatures. As the temperature rises, stacking fault tetrahedara and dislocation loops can appear, followed by bubbles, voids, precipitates, and solute segregation. Temperatures closer to the melting point lead to the formation of grain-boundary helium cavities. Room-temperature delta plutonium sits just at the lower end of the range for bubble and void formation, well below the temperature necessary for forming a helium grain-boundary cavity.

Some but not all of these defects can be annealed out with temperature and time. The particular temperature dependence of changes in properties could sort this out, but it is essential to be aware of all the possibilities, rather than assuming one type dominates. For example, can a helium atom find a vacancy? At what temperatures? If so, can a helium-filled vacancy find another and coalesce? These are all important, unanswered questions. In fact, there is no solid evidence from electron microscopy photos that helium even exists in voids. Consider that ordinary metals, all of which exhibit thermally activated vacancies, do not develop voids over time. Such voids only occur as a result of intense radiation damage and gas evolution, and voids trap gas because a solid-gas interface always blocks escape of the gas and may only occur if the damage rate is high. These are just some of the assumptions and selective considerations that today cloud our understanding of aging, and a few facts that must be accommodated.

Now consider radiation-induced local heating. If the US phase diagram for Pu-Ga is correct, the alloy is stable with temperature over a broad range, and we should see no radiation-induced local heating phase changes. If the Russian diagram is correct, then δ plutonium is less stable at lower

temperatures, and so a measurement sensitive to phase changes might see those changes at temperatures below 400 K or so. Finally, the uranium and helium never go away or are affected by temperature. Thus, it is compelling to use measurements that can detect phase changes with temperature and time, without disturbing the decay processes by introducing additional decays with time as in mixing with the very short lived isotope ^{238}Pu.

Noting that density is an obvious measurement choice, it is essential to realize that little information can be gained from diffraction density measurements because they see only the atoms in the right places and fail to detect defects. Thus, immersion density is an important tool, so long as it is performed with great care and with the use of nonreactive fluids.

The same is true with respect to elastic stiffness. Today, we can see changes in elastic stiffness with an ultimate sensitivity of a part in 10^8. Because elastic moduli are sensitive to defects, impurities, and phases, their measurement as a function of temperature may be able to sort out the relative presence and contributions of the processes that contribute to aging.

But the real message is that our understanding of plutonium requires that we construct our theories using all *valid measurements* and reject ones that fail to be consistent with all relevant data and known effects.

Plutonium Isotopes Enter the Environment as a Result of the Accident at the Fukushima Daiichi Nuclear Power Plant

Jian Zheng, Keiko Tagami, Tatsuo Aono, and Shigeo Uchida
Research Center for Radiation Protection
National Institute of Radiological Sciences
Japan

Jian Zheng and his colleagues discuss some of the techniques used to determine environmental contamination from the Fukushima Daiichi energy accident.

Overview

On March 11, 2011, an earthquake and subsequent tsunami off the Pacific coast of Tohoku, Japan, triggered an energy accident at the Fukushima Daiichi Nuclear Power Plant (FDNPP). The tsunami's damage produced equipment failures in the power plant. These failures led to nuclear meltdowns and the release of radioactive materials. This accident is the largest of its type since the Chernobyl disaster of 1986.

The FDNPP consists of six boiling water reactor units. Of the four damaged reactor units (Units 1 through 4), three reactors (Units 1 through 3) were operational at the time of the earthquake responsible for the nuclear crisis. The fourth unit had been shut down since November 2010; all the unit's fuel had been removed and stored in its spent-fuel pool.

Most of the fuel in the FDNPP reactors consisted of uranium dioxide (UO_2). However, the Unit 3 reactor contained 32 mixed-oxide fuel assemblies with approximately 6% plutonium, corresponding to approximately 4% of the core loading. The reactor cores of Units 1 through 3 contained approximately 256 metric tons of nuclear fuel. The spent-fuel pools inside the four damaged reactor buildings contained an additional 461 tons of nuclear fuel. Of these buildings, the Unit 4 reactor building was the largest, containing 1331 spent nuclear fuel assemblies—this is 1.4 times the amount of fuel loaded in Units 2 and 3.

Based on this fuel configuration, there are two possible sources for radionuclides to be potentially released to the environment as a result of the FDNPP accident: (1) possible release from the damaged reactor cores of Units 1 through 3 and (2) possible release from the spent-fuel pools.

Radioactive materials were released principally during the early phase of the FDNPP accident. During this time, venting operations were conducted in Units 1, 2, and 3. Moreover, hydrogen explosions took place in the reactor buildings of Units 1 and 3. There was also a breach in the Unit 2 containment vessel. On March 15, 2011, a hydrogen explosion took place on the fourth floor of the Unit 4 reactor building. This building contained the largest spent-fuel pool. This explosion caused a fire. It has been suggested but not verified that there was a release of FPs (fission products), such as cesium-137, from the spent-fuel pool in the Unit 4 reactor building. Whether the spent-fuel pool in the Unit 4 reactor building contributed to the large amounts of FPs released remains an important issue of debate.

Source Identification and Estimation of Total Amounts of Plutonium Isotopes Released into the Environment

Although no significant increase in $^{239+240}$Pu activity in soils was found after the accident, the high contribution of global fallout plutonium in soils could hamper obtaining accurate FDNPP-derived plutonium isotopic composition in the environment. The contribution of global fallout plutonium must be kept as low as possible so that researchers can obtain accurate isotopic composition for the FDNPP-source plutonium in the environment.

We attempted to detect the FDNPP plutonium signature in litter samples taken from a forest in the Fukushima Prefecture (Fig. 1). Studies conducted by the International Atomic Energy Agency have established that the soil-plant transfer factor of plutonium is extremely low (4×10^{-3}–9×10^{-6}). Thus, the presence of global fallout plutonium in the dead leaves via the soil-plant transfer was negligible *before* the accident. We considered that the atom ratios of ^{240}Pu/^{239}Pu (0.330 ± 0.032) and ^{241}Pu/^{239}Pu (0.135 ± 0.012), as well as the ^{241}Pu/$^{239+240}$Pu activity ratio (108 ± 3) found in litter samples in the Fukushima Prefecture forest, reflected the isotopic composition of plutonium isotopes released from the FDNPP accident.

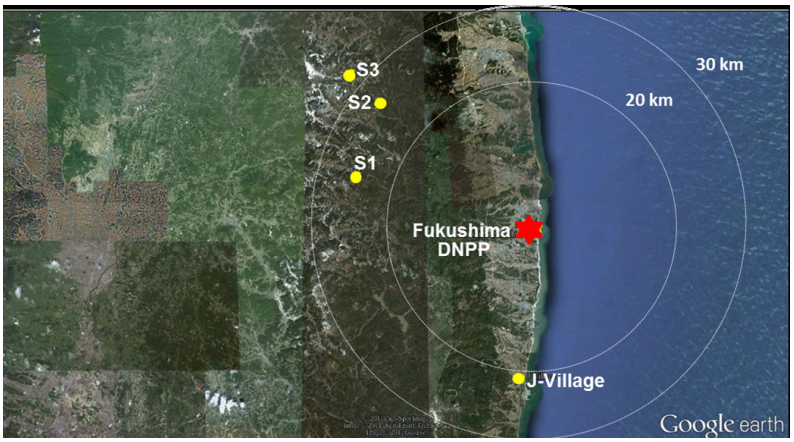

Fig. 1. This map shows the isotopic composition of the FDNPP source plutonium in forest litter samples in the Fukushima Prefecture.

As shown in Fig. 2, plutonium isotopic composition observed in surface soil samples taken from J-Village was located in the mixing line between global fallout and the FDNPP-source plutonium isotopes. This composition indicates an 87% contribution from FDNPP-source plutonium and a 13% contribution from global fallout.

Recently, the Japan Atomic Energy Agency conducted a detailed estimation of fuel composition in the FDNPP in March 2011. This estimation used the

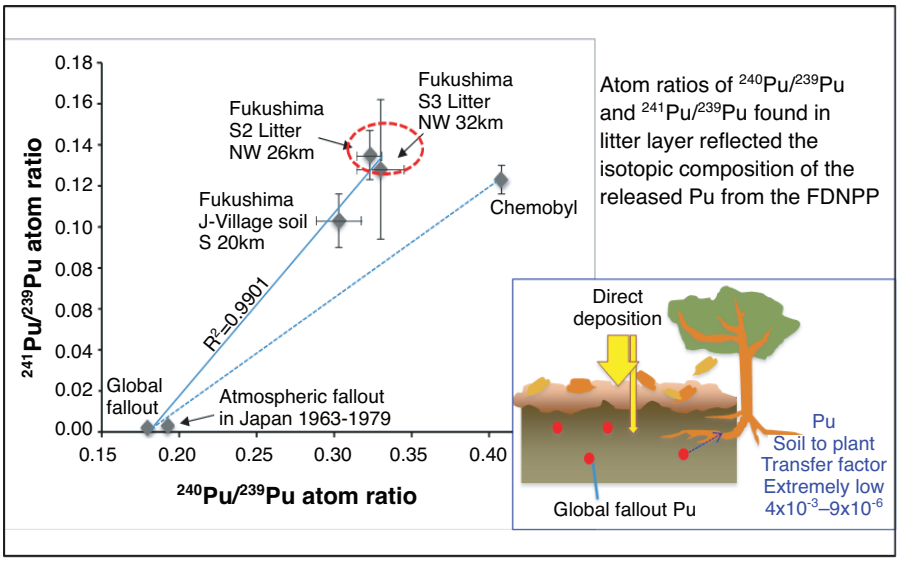

Fig. 2. This plot and inset show a comparison of isotopic composition with those of the Chernobyl accident and global fallout sources.

ORIGEN2 code and the fuel burn-up data from TEPCO. Scientists estimated fuel inventory in each reactor core (Units 1–3), in each spent-fuel pool in the reactor buildings for Units 1–3, and in the largest spent-fuel pool in the Unit 4 reactor building. These estimates were then used to derive the accurate plutonium isotopic composition of the damaged reactor cores and the spent-fuel pools.

As shown in Fig. 3, the maximum atom ratio of $^{240}Pu/^{239}Pu$ (0.330 ± 0.032) observed in the environment (litter samples in the Fukushima forest) was in good agreement with the plutonium isotopic composition in the damaged reactor cores, but it was much lower than the $^{240}Pu/^{239}Pu$ atom ratios in the spent-fuel pools. Regarding the $^{241}Pu/^{239}Pu$ atom ratio, the value (0.135 ± 0.012) observed in the environment (litter samples in the Fukushima forest) was also close to those values observed in the damaged reactor cores, although these proved lower than the values observed in the spent-fuel pools. This comparison indicated that plutonium isotopes were released from the damaged reactors but not from the spent-fuel pools. This conclusion was further supported by data for the $^{238}Pu/^{239+240}Pu$ activity ratio. The highest $^{238}Pu/^{239+240}Pu$ activity ratio observed in soil samples collected about 500 meters north-northwest of the stacks of reactor Units 1 and 2 was consistent with those in the damaged reactor cores. However, the activity ratios were significantly lower than those in the spent-fuel pools.

Table 1 lists measurements of plutonium isotopes and ^{137}Cs in environmental samples. These measurements were used to determine the amounts of plutonium isotopes released into the environment. Our estimates are very close to those estimated by METI (Minister of Economy, Trade and Industry) and about four orders of magnitude lower than those of the Chernobyl accident. Although the inventories of plutonium isotopes (^{238}Pu, $^{239+240}Pu$, and ^{241}Pu) in the reactors in the FDNPP were 3.5–10 times higher than those in the Chernobyl Unit 4 reactor, the percentages of core inventory released for all plutonium isotopes—were approximately five orders of magnitude lower than those of the Chernobyl accident.

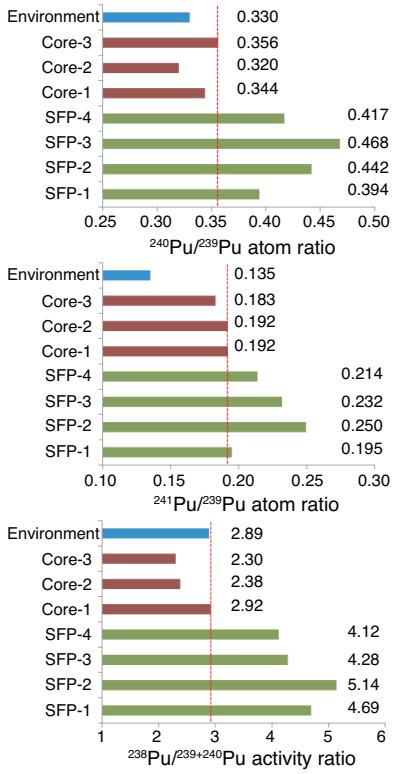

Fig. 3. These graphs compare plutonium isotopic compositions in environmental samples, the damaged reactor cores, and the spent-fuel pools at the FDNPP.

Table 1. Estimated amounts of plutonium isotopes released from the FDNPP accident and a comparison with Chernobyl.

		FDNPP accident	
	Chernobyl	**METI calculated**	**Estimated in this study**
Amounts released (Bq)			
Pu-239+240 Pu-241 Pu-238	8.7×10^{13} 7.2×10^{15} 3.5×10^{13}	6.4×10^{9} 1.2×10^{12} 1.9×10^{10}	$1.0\times10^{9} – 2.4\times10^{9}$ $1.1\times10^{11} – 2.6\times10^{11}$ $2.9\times10^{9} – 6.9\times10^{9}$
Pu inventories at reactors at the time of accident initiation (Bq)			
Pu-239+240 Pu-241 Pu-238	2.4×10^{15} 1.9×10^{17} 1.0×10^{15}	--- --- ---	8.3×10^{15} 7.0×10^{17} 1.1×10^{16}
Percentage of core inventory released (%)			
Pu-239+240 Pu-241 Pu-238	3.5 3.5 3.5	--- --- ---	$1.2\times10^{-5} – 2.9\times10^{-5}$ $1.6\times10^{-5} – 3.7\times10^{-5}$ $2.0\times10^{-5} – 4.7\times10^{-5}$

Acknowledgments

This work was supported by Grant-in-Aid for Scientific Research on Innovative Areas Grant Number 24110004 and partly supported by the Agency for Natural Resources and Energy, the Ministry of Economy, Trade and Industry (METI), Japan.

With respect to the marine environment, information is generally quite limited regarding the source identification and distribution of plutonium isotopes after the FDNPP accident. We reported the first dataset on the distribution of plutonium isotopes in surface sediments in the Pacific 30 kilometers off the Fukushima coast after the accident. We analyzed activities of $^{239+240}$Pu and ^{241}Pu, as well as the atom ratios of ^{240}Pu/^{239}Pu and ^{241}Pu/^{239}Pu in surface sediments collected in July–August 2011. From this analysis we estimated the extent of possible environmental plutonium contamination.

We concluded that immediate plutonium contamination from the FDNPP accident was not observed in marine sediments outside the 30-kilometer zone. To understand fully this possible contamination of plutonium isotopes as a result of the FDNPP accident, we recently conducted a comprehensive investigation regarding the contamination sources and the distribution of radioactive cesium and plutonium isotopes in marine sediments inside the 30-kilometer zone of the FDNPP in the western North Pacific coastal waters.

Plutonium isotopes (^{239}Pu, ^{240}Pu, and ^{241}Pu) and radiocesium isotopes (^{134}Cs and ^{137}Cs) in the samples were determined. The high activities of radiocesium and the ^{134}Cs/^{137}Cs activity ratios with values around 1 (decay corrected to 15 March 2011) suggested that these samples were contaminated by Fukushima-released radionuclides. However, the activities of $^{239+240}$Pu and ^{241}Pu were low compared with the background level before the FDNPP accident.

The plutonium atom ratios (^{240}Pu/^{239}Pu and ^{241}Pu/^{239}Pu) suggested that global fallout and the Pacific Proving Ground close-in fallout are the main sources of plutonium contamination in the marine sediments (Fig. 4). Because the plutonium isotopes are particle-reactive and can be easily incorporated with the marine sediments, we concluded that the release of plutonium isotopes from the FDNPP accident to the costal marine environment was negligible.

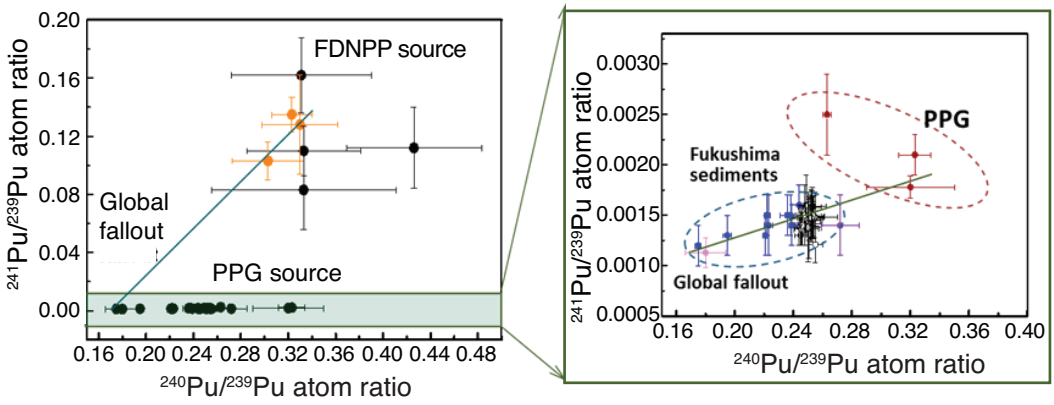

Fig. 4. This mixing plot shows ^{241}Pu/^{239}Pu atom ratio vs. ^{240}Pu/^{239}Pu atom ratio in the Fukushima sediments, as compared with the plutonium compositions of global fallout, the FDNPP release, and the Pacific Proving Ground close-in fallout. The closed pink circle represents the global fallout; the closed blue circles represent the surface sediment samples collected outside the 30-km zone; the open black circles represent the vertical distributed sediment samples within the 30-km zone; the closed violet circle represents the Sagami Bay sediment sample; and the closed wine circles represent the Pacific Proving Ground source.

Presently, more than 300,000 tons of radioactive liquid waste are stored in large tanks within the FDNPP site boundary. The total amounts of ^{238}Pu, $^{239+240}$Pu, and ^{241}Pu contained in this boundary were estimated to be 3×10^{8} Bq, 1×10^{8} Bq, and 1×10^{10} Bq, respectively. Future earthquakes and other unexpected events could create leaks in the storage tanks, as well as introduce new plutonium contamination into the sea. Therefore, we recommend that plutonium isotopes in the marine environment, particularly in the trench and at coastal sites near the FDNPP site, should be continuously investigated.

Plutonium Containment at the Waste Isolation Pilot Plant

Don Reed
Actinide Chemistry and Repository Science Program Team
Repository Science and Operations
Los Alamos National Laboratory

Plutonium—it is by far the radioactive contaminant of most concern not only in the permanent disposal of nuclear waste but also in the subsurface remediation of Department of Energy sites. Plutonium possesses a combination of distinct characteristics. It has a complex environmental chemistry, which makes its migration behavior very difficult for scientists to reliably predict. It possesses a high radiotoxicity that drives very stringent regulatory requirements. And it has a strong connection to nuclear weapons, giving the element a highly negative public perception and driving concern for plutonium contamination. For these reasons, we must understand the site-relevant chemistry of this actinide, since this is needed to provide a strong scientific basis for the safety case of permanent nuclear repositories, as well as site cleanup and containment strategies where plutonium contamination is known to exist.

Don Reed discusses his team's ongoing efforts to make a well-supported safety case for WIPP to contain plutonium.

WIPP: A Cornerstone of the DOE Waste Cleanup Effort

A repository in the bedded salt formation in southeastern New Mexico, the Waste Isolation Pilot Plant (WIPP) was licensed in 1998 by the Environmental Protection Agency as an important component of the Department of Energy's strategy in safely disposing of nuclear waste (Fig. 1). WIPP was specifically designed to accept transuranic (TRU) waste.

Also sometimes known as intermediate-level nuclear waste, TRU waste has the following regulatory definition: radioactive waste which has been contaminated with alpha-emitting transuranic radionuclides possessing half-lives great than 20 years and in concentrations greater than 100 nCi/g (3.7 MBq/kg). Such waste has been generated during weapons production throughout the Department of Energy complex. The waste consists of solidified waste streams that are byproducts of weapons complex activities, such as cut up gloveboxes, decommissioned labs, and used laboratory equipment, that meets regulatory criteria and is packaged in iron containers and boxes for transport and placement in WIPP.

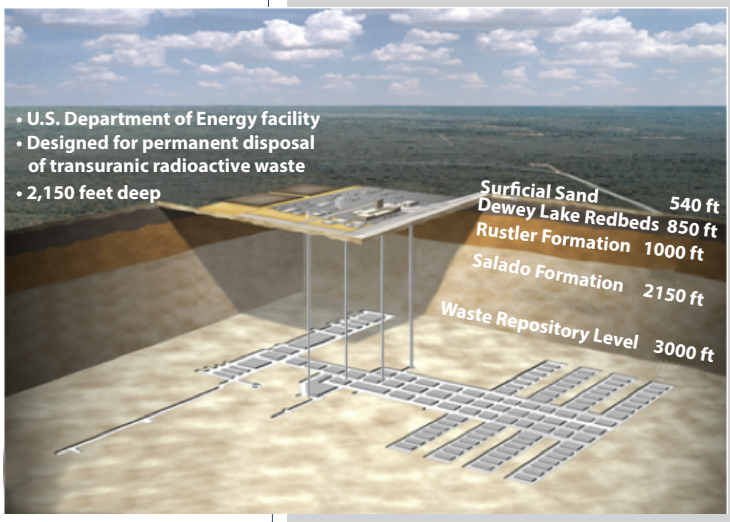

Fig. 1. This image shows WIPP's design and configuration. Six of the eight panels shown in this design are already full. More than 86,000 transuranic waste containers have been emplaced.

In this context, WIPP provides a means to permanently dispose of highly contaminated waste. It represents a cost-effective solution to the alternative, which consists of storing and managing such waste in surface facilities for a span of many years. At this time, there is no permanent disposal option for spent fuel and high-level nuclear waste (HLW) in the United States. Furthermore, there are no operational spent fuel/HLW repositories worldwide, although a number of countries are moving steadily toward licensing such sites.

The Actinide Chemistry and Repository Science Program Team

Researchers at Los Alamos National Laboratory have significantly contributed to the licensing of WIPP by performing numerous laboratory studies dating back to the early 1990s. Since 2005, the Actinide Chemistry and Repository Science Program (ACRSP) team at Los Alamos has operated offsite nuclear laboratories at the Carlsbad Environmental Monitoring and Research Center. This center is a university institute operated by New Mexico State University. Managed by Don Reed, the ACRSP team (Fig. 2) was originally part of the Laboratory's Earth and Environmental Sciences Division before it was reorganized into Environmental Programs in the summer of 2013.

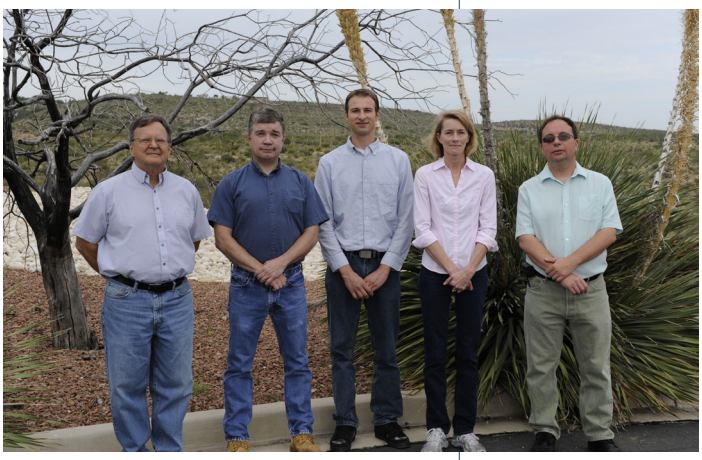

Fig. 2. Pictured from left to right are Don Reed, Mike Richmann, Tim Dittrich, Julie Swanson, and Jef Lucchini. Dittrich is a postdoc; all the others are staff members.

The primary mission of the ACRSP team is to support WIPP recertification efforts. The team does this by performing actinide experimental studies that support the long-term safety case. Directly supported by the Department of Energy's Carlsbad Field Office as part of EM-20, much of the team's work is performed collaboratively over the years with university partners at Arizona State University, Illinois Institute of Technology, Texas A&M, University of Notre Dame, Florida State University, Florida International University, and New Mexico State University. Such work has received much international visibility, resulting in collaborations with the Institute for Nuclear Waste Disposal (INE) and the Helmholtz-Zentrum Dresden-Rossendorf (HZDR), both in Germany. The ACRSP team is also active in the Nuclear Energy Agency Salt Club and the Thermodynamic Database Project

Addressing WIPP Misconceptions

There are often misconceptions about the core safety case for a salt-based repository like the WIPP because many are more familiar with HLW repository concepts that are typically sites in open-system geologies in which release is by interconnected groundwater pathways. In a salt concept, self-sealing occurs relatively rapidly (less than 200 years), leading to a sealed repository horizon with no interconnected groundwater pathways for release. In WIPP's case, the expected scenario is that the repository remains sealed throughout its repository lifetime and brine saturation does not occur. Under this expected scenario, there should be no release of TRU from the WIPP repository.

However, human-intrusion scenarios, such as drilling for various reasons through the repository horizon, can introduce brine into the repository, leading to the solubilization of the plutonium present and its subsequent release to the accessible environment. Regulations dictate that we must address even low-probability scenarios, driving the need to investigate and understand the plutonium solution chemistry in the brines that could

be introduced and used to predict, with confidence, the concentration of mobile plutonium species that could be present. In this regulatory context, The Department of Energy must show that the repository works as prescribed, even during the worst-case scenario of brine intrusion and release.

One of the most important contributions made by the ACRSP team was to experimentally investigate the speciation of plutonium for the low-probability event of brine inundation to support current performance assessment (PA) predictions. Current projections indicate that approximately 12,000 kilograms of plutonium (approximately 75% by mass Pu-239, approximately 14% Pu-242, and approximately 5% Pu-240) will be emplaced during the operational lifetime of WIPP. Furthermore, more than 75% of this plutonium is already at WIPP. Although plutonium and americium initially have a relatively equal contribution to potential release from the site, plutonium very quickly becomes the dominant contributor to potential release because it has a much longer half-life and, for this reason, is the predominant actinide of concern over the repository's lifetime.

There are three main considerations for defining the speciation of plutonium at WIPP: (1) the oxidation state distribution, (2) the solubility of each oxidation state that may be present, and (3) the contribution of plutonium colloids to the amount of plutonium that can be mobile.

Plutonium in the environment can exist as Pu^{3+}, Pu^{4+}, PuO_2^{+} and PuO_2^{2+} complexes. Under moderately alkaline conditions, such as those expected at WIPP, the higher-valent PuO_2^{+} and PuO_2^{2+} complexes are predicted to be highly soluble, whereas the Pu^{3+} and Pu^{4+} species are expected to be barely soluble. Research at Los Alamos has demonstrated that the excess iron at WIPP—it is present as container material and as part of the TRU waste—leads to the relatively rapid reduction of higher-valent plutonium under a wide range of possible conditions. This work was confirmed using XANES analysis (Fig. 3) and aqueous extraction techniques. Although Pu(III) species predominated under the specific conditions of these Los Alamos experiments, this key result supports the WIPP PA position that the plutonium "speciates" as Pu(III) and Pu(IV) species because a number of pathways that would likely stabilize Pu(IV) relative to Pu(III) were not addressed. Most importantly, these key results eliminate concern that higher-valent species, specifically Pu(V) and Pu(VI), with their with their much higher solubility—can persist in the expected WIPP environment (although they may be initially present in the waste).

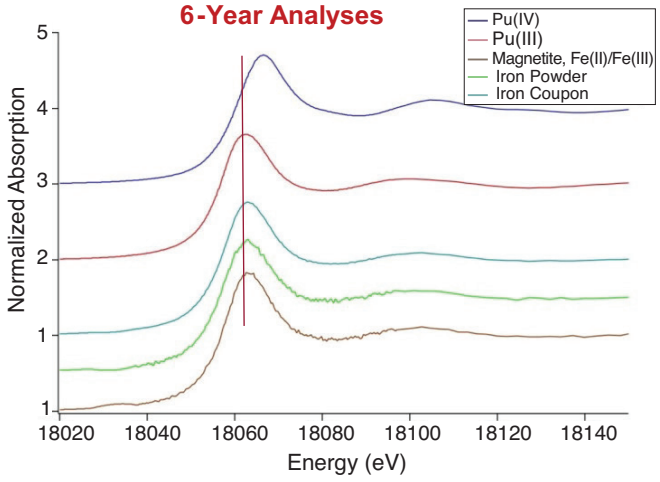

Fig. 3. This graph plots XANES analysis of plutonium precipitates after six years, along with Pu(IV)O_2 and Pu(III)F_3 standards (top two spectra). These data show that the Pu(III) phases—which were initially dissolved Pu(VI)—are predominant. These results confirm the important effect of reduced iron on the plutonium chemistry and the brine system's redox environment.

It is difficult to experimentally measure the oxidation-state specific solubility of plutonium in the +III and +IV oxidation states because of the complexity associated with stabilizing and isolating each oxidation state. For this reason, WIPP has used redox-invariant analogs. Americium and neodymium are the analogs for Pu(III), with thorium the analog for Pu(IV). To overcome modeling difficulties associated with the complexity of the brine,

the ACRSP team performed a series of site-specific experiments to measure the solubility of thorium and neodymium. The team conducted these multiyear, long-term experiments over a relatively wide pH range. The results of these experiments confirm that the solubility of Pu(III), with current WIPP PA assumptions, is defined by an EDTA (ethylenediaminetetraacetic acid) complex rather than the hydroxide precipitate. Moreover, Pu(IV) solubility—based on the thorium analog—is controlled by an oxy-hydroxide phase that tends toward the formation of less than 10-nanometer colloidal species with high long-term metastability. Although these data support current modeling efforts, such data remain somewhat unsatisfactory because they overpredict the expected solubility of plutonium. Thus, the team plans to perform additional experiments with plutonium directly and use other analogs, such as americium for Pu(III) and Np(IV) for Pu(IV), to better link to the expect plutonium chemistry.

Plutonium colloids represent the third contribution to mobile plutonium concentration. In light of recent literature results and new WIPP-specific data, the team re-examined the mineral, intrinsic, and microbial contributions to the WIPP mobile colloidal actinide source-term model. These experiments indicate that nanosized intrinsic colloids (typically less than 10 nanometers) are almost always present in brine, even after multiyear equilibrium times. Only mineral colloids associated with Fe(II) colloidal species were observed in the team's experiments.

The team also determined the biosorption of actinides toward WIPP-indigenous microorganisms and used the results to update the bio-colloid model. These biosorption experiments were performed using halophilic bacteria (*Chromohalobacter* sp.) and archaea (*Halobacterium noricense*) with Nd(III) and Th(IV) as analogs for Pu(III) and Pu(IV). Although significant association was noted, it proved difficult to separate sorptive processes from bio-mediated precipitation of the actinide phases. These new data, which remain incomplete, nevertheless provide significant improvement in understanding the potential contribution of colloidal species to the WIPP actinide source term.

In Closing

ACRSP research has made and continues to make key contributions to what is a well-supported WIPP safety case for the long-term containment of plutonium in a salt repository. However, there remain many aspects of plutonium chemistry under these relatively complex conditions that are not fully understood. Such understanding is critically needed because the use of a salt-repository concept for a spent fuel/HLW nuclear waste repository is still under consideration.

The Department of Energy continues to support this research, with additional plutonium speciation studies already underway. WIPP is currently shut down as a result of operational issues. Although these issues are certainly significant and must be resolved, they do not negatively impact the core safety basis for the long-term containment of plutonium. A salt-repository concept remains a viable approach to permanently dispose of plutonium-containing nuclear waste.

Developing a Smaller Scale Plutonium-Analysis Capability

Pam Thompson and Phil Kaye
Atomic Weapons Establishment
United Kingdom

Around the world, nuclear facilities capable of chemically analyzing bulk actinide materials are reaching the end of their operational lives. Replacing such facilities is prohibitively expensive, given today's ever-tightening regulations and modern safety standards. Rather than try to replace such facilities, we are working on a completely different approach, one that we address in this article.

Current nuclear chemical analysis laboratories handle and store significant inventories of fissile material. Such laboratories (Fig. 1) contain suites of gloveboxes and fume hoods with associated extract systems. Much of the instrumentation has been customized to easily interface with the containment. Current analyses use strong acids that create problems because they corrode gloveboxes and pipework (Fig. 2). These analyses also generate significant quantities of radioactive waste.

Our approach is to develop analytical methods that use much smaller amounts of actinide material, lowering the quantity of material used and thus enabling the use of laboratories where such work could not be performed otherwise. One possible approach is to use smaller scale automated techniques, solid-sampling methods, and commercial off-the-shelf equipment. This new type of facility would be categorized as a radiological-level facility, one with a small nuclear annex containing a minimal number of generic gloveboxes and fume hoods.

Scientists are also investigating ways to improve analytical techniques. Improved techniques would have various benefits, such as the ability to handle limited amounts of plutonium while minimizing sample inventory and containment requirements, increasing safety, and reducing costs associated with the design of future capabilities. Key analytes of interest being studied to date are plutonium content, trace elements, and trace radioelements.

Analysis Requirements

Key analysis requirements are for plutonium, gallium, uranium, neptunium, and trace element assays. An assay consists of determining a metal's purity, a key measurement of material quality. Plutonium alloyed with gallium retains the structure of the high-temperature delta phase when it cools to room temperature, thus exploiting its more favorable physical properties. As a radioactive material, plutonium over time produces decay products, such as uranium, americium, and neptunium.

Trace elements are of interest for several reasons. In some instances, they may act to alter the stability of the different metallurgical phases of plutonium, with adverse impact on the ability of the final product to meet specifications. In other cases, their presence may be indicative of problems with the material production and recycling processes.

Pam Thompson proposes facilities designed for smaller scale pluonium analysis.

Fig. 1. This photo shows a typical actinide analysis facility, which consists of suites of gloveboxes and fume hoods.

Fig. 2. Acidic fumes in the glovebox exhaust contributed to the corrosion in this extract ductwork.

Fig. 3. This glovebox-contained autotitrator system is used to perform plutonium assay measurements.

Current Methods

The current method used to conduct plutonium assay at the Atomic Weapons Establishment (AWE) is a modified version of the Corpel redox titrimetric process (Fig. 3). Using this method, we can determine plutonium with a standard error of 0.05% without systematic bias. Contained in a glovebox, this system is semi-automated to minimize variations and reduce operator error. An ideal system would reduce the amount of handled plutonium and minimize the complexity of the analytical equipment.

Before analysis, gallium and uranium must be purified by using ion-exchange chromatography to chemically separate the elements. The resultant analytical solution is then spiked with an internal standard (zinc for gallium; yttrium for uranium), transferred to a fume hood, and placed in a doubly sealed sample cell. It is here that the solution is then analysed for gallium content by using wavelength dispersive x-ray fluorescence (WDXRF). To measure neptunium content, a separate solution is analysed with high-resolution gamma spectrometry (HRGS).

Although WDXRF provides a precision of less than 1% relative standard deviation (RSD), this technique requires duplicate samples of approximately 1 gram each. These samples are dissolved in glassware, which if it breaks would cause considerable contamination. Table 1 lists amounts of duplicate material required for typical analyses.

Table 1. Material required for typical analysis (g, duplicate analysis).

Current Assay ISO	Am	Ga	U	Np	Si	Trace Elements	Total
	2.5	2	2	2	0.2	0.5	5.2
Proposed Assay ISO	Am	Ga	U	Np	Si	Trace Elements	
	0.6	0.6	0.6	0.6	0.2	0.05	0.85

To determine trace elements, 0.5 gram of plutonium was dissolved and diluted in acid to generate a 50 parts-per-million (ppm) solution. This solution was then measured on a glovebox-interfaced high-resolution inductively coupled plasma mass spectrometer (ICP-MS). It is important throughout the process to use ultra-high-purity acids and clean labware to prevent saturation from contaminants.

Fig. 4. The TIMS can quantify plutonium and uranium in comparable precisions while using smaller analytical samples.

Proposed Methods

Using isotope dilution thermal ionization mass spectrometry (ID-TIMS) to quantify plutonium and uranium should allow the achievement of comparable precisions while using smaller analytical samples (Fig. 4). Plutonium ID-TIMS requires a sample of approximately 20 µg of plutonium. A solution of plutonium alloy is spiked with Pu-242 and U-233 tracers, oxidized with nitric acid, and converted to the chloride form. Now containing Pu(IV), U(VI), and Am(III), this solution is loaded onto an AG1-X8 anion-exchange resin column.

Pu(IV) and U(VI) are retained on the column, whereas Am(III) is eluted with concentrated hydrochloric acid and discarded. The Pu(IV) is then reduced to Pu(III) by adding a solution of 10% hydrobromic acid in concentrated hydrochloric acid. Uranium (VI) is then recovered by elution with 0.1 M hydrochloric acid. Plutonium solutions are converted to the nitrate form and diluted to 1 ppm of plutonium. One microliter of this solution is loaded onto rhenium filaments before TIMS analysis. Figure 5 visually illustrates this process.

To perform gallium analysis, an isotope dilution ICP-MS (ID-ICP-MS) method is under development. The current anion-exchange separation method is not suitable for use with standalone ICP-MS techniques. Its limited efficiency leads to significant plutonium content in the analytical solution.

The method chosen for actinide extraction is Eichrom TRU Spec™ resin [supported octyl(phenyl)-N,N-di-isobutyl carbamoyl phosphine oxide (CMPO)]. Unlike most extractants, this resin can reversibly extract trivalent actinides, such as americium, in addition to the higher valent species more common in plutonium and uranium. As such, this resin offers the best decontamination of the eluted solution.

One-half of a milligram of plutonium in 2 M hydrochloric acid is taken in duplicate. One duplicate is spiked with a Ga-71 enriched solution (~99% Ga-71) to a level at which the expected concentrations of the Ga-69 and Ga-71 isotopes are approximately equal. Both solutions are then treated with 0.4 milliliters of 16 M nitric acid and left to stand overnight. During this period, the nitric acid oxidizes the Pu(III) to Pu(IV).

The following day, the solutions are heated to ensure equilibration of the gallium isotopes and oxidation of the plutonium. After heating, the samples are diluted to 4 M nitric acid and added to the column. The retained plutonium can be seen as a green band at the top of the resin. The gallium is then eluted with 4 M nitric acid. The separated solution is diluted to 10–15 ppb of gallium and analysed on a glovebox-interfaced Thermo Element2 High-Resolution ICP-MS.

To determine separation efficiency, solutions were analysed using HRGS and alpha spectrometry. The results indicate that 10,000-fold decontamination had been achieved by the separation, with average solution activities below 1 kBq after separation. Further dilution required for ICP-MS analysis reduces this activity to below 50 Bq in solution, making the process useable with normal uncontained ICP-MS equipment. Gallium recovery in the samples was analysed by ICP-MS, using normal trace elemental methods; greater than 95% of the gallium was recovered from the separation.

For trace elements in plutonium, there have been studies carried out to adapt the plutonium oxalate precipitation (POP) separation method, which is used currently at AWE. This method involved dissolving 0.5-gram samples in hydrochloric acid. Hydroxylamine hydrochloride is added to stabilize the Pu(III) oxidation state. The plutonium is then precipitated as Pu(III) after the addition of oxalate (Fig. 6). Centrifugation is used to separate the oxalate precipitate, and ICP-optial emission spectroscopy (ICP-OES) is used to recover the supernatant for analysis.

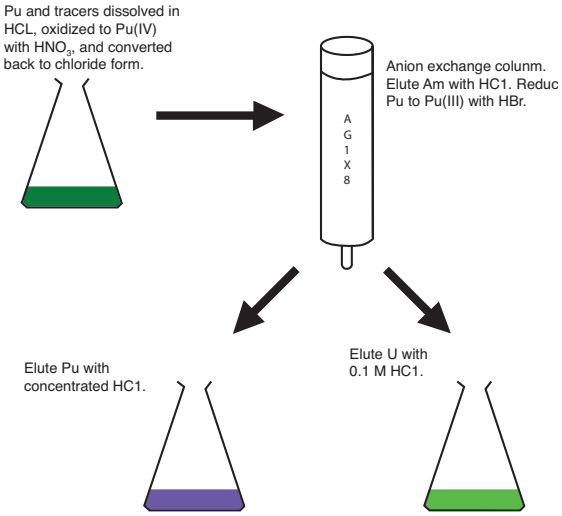

Fig. 5. This illustration outlines the ID-TIMS separation scheme.

Fig. 6. This test tube holds Pu(III) oxalate precipitate.

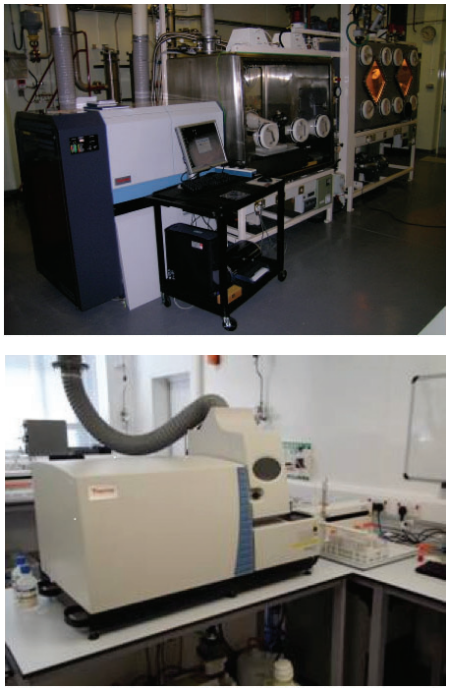

Fig. 7. Note the difference in space requirements and complexity of installation for a glovebox-contained High-Resolution ICP-MS and a commercially available ICP-MS.

To check the viability of a smaller scale process using ICP-MS analysis, 0.5-ml aliquots of these solutions were added to 20-ml of ultra-high-purity 5% nitric acid, with indium added at 1 ppb as an internal standard. The samples were then analysed by glovebox-interfaced a High-Resolution ICP-MS. Figure 7 shows examples of a glovebox containing High-Resolution ICP-MS and an uncontained quadrupole ICP-MS that would be suitable for this small-scale method.

The obtained results did not differ significantly from the established values for a control material for most analytes. Differences were observed for silicon, calcium, and lead. Of these, only silicon is required for plutonium certification. If this result cannot be improved, we will seek an alternative technique.

The initial sample was diluted to the equivalent of 4 g of plutonium, which (using the demonstrated 99.8% decontamination) results in a total plutonium activity in the ICP-MS solution of 10 kBq. We anticipate that a safety justification will be made for analysis of solutions at this level into uncontained instruments.

Conclusion

Initial studies indicate that it is possible to significantly reduce the amount of plutonium required in the analytical processes used for material certification measurements. However, all these techniques are still at the development stage. A considerable amount of further work is required to fully qualify them.

Smaller scale techniques should simplify the containment requirements for routine analysis of plutonium in future analytical laboratories. Such techniques will enable the use of commercial spectrometers. Whilst this should result in reduced costs for new laboratories, R&D is required to show that the results from such techniques are satisfactory for surveillance and nuclear forensics activities, if the ability to perform wet chemistry on bulk quantities of plutonium is given up on cost and health and safety grounds.

The Dynamics and Freeze Frames of Magnetic Fluctuations in Plutonium-Based Materials

Matthias J. Graf
Theoretical Division
Los Alamos National Laboratory

Per Söderlind
Condensed Matter and Materials Division
Lawrence Livermore National Laboratory

Matthias Graf discusses plutonium-based materials and their proximity to magnetism.

A key nuclear material, plutonium metal also happens to have made life difficult but interesting for scientists who have tried to understand and predict its properties and electronic structure. Plutonium metal certainly does not give up its secrets easily.

After decades of experimental probing and computational modeling of elemental plutonium, researchers may at last have come one step closer to revealing the existence of magnetic spin fluctuations in this class of materials. A common thread of our research of plutonium-based materials is their proximity to magnetism, as well as the presence of quantum spin fluctuations controlled by strong spin-orbit coupling. In the normal state, these fluctuations lead to renormalization of electron bands, as well as the redistribution of spectral weight, in particular near the Fermi energy, the highest energy level for electrons in the filled Fermi sea at absolute zero temperature. Hence, spin fluctuations even may be responsible for unconventional superconductivity in the intermetallic actinide $PuCoGa_5$.

Around defects, such fluctuations can induce magnetism because defects break the translational symmetry of the ground state like rocks in the sea break waves—both leave their marks. Thus, density-functional-theory calculations used to predict antiferromagnetism in the Pu-Ga alloy system and in magnetically disordered plutonium may correspond to the freeze-frame pictures of rapidly fluctuating magnetic moments.

Introduction

The concept of spin fluctuations in actinide metals has been around for a while—it is one based on the interpretation of various old and new experiments. Think of spin fluctuations as the "glue" for correlated interactions between electrons and how they collectively coordinate their behavior. An oversimplified picture would have them as the jiggling and wiggling of subatomic magnets made of electrons. Inelastic neutron scattering can probe such fluctuations on a fast timescale of nanoseconds.

Recent reports by Los Alamos scientists of their observation with inelastic neutron scattering in gallium-stabilized δ-Pu will once and for all put an end to the long-standing debate of whether elemental plutonium or Pu-Ga alloys are magnetic (they are). Whether this metal has propensity toward magnetism is all relative and seems to depend on the timescale of the experimental probe. An analog in our everyday world would be the shutter-time of a photo camera—the longer the exposure time, the blurrier and more smeared out the resultant picture. Since $PuCoGa_5$ is considered a close relative of elemental plutonium, this result further suggests that superconductivity is magnetically mediated in $PuCoGa_5$.

A fascinating problem indeed, plutonium's proximity to magnetism with static long-range order may one day shed light on its many mysteries. For example, little is known about the spectral function of electronic excitations in plutonium materials or the mechanism and symmetry of superconducting pairing in $PuCoGa_5$, which has the highest superconducting transition temperature of 18.5 K (or –254.5°C) above absolute zero temperature of any actinide material.

Over the years, our groups and others at Los Alamos National Laboratory and Lawrence Livermore National Laboratory have performed density-functional-theory (DFT) calculations of the electronic band structure to provide much-needed guidance for (1) stabilizing antiferromagnetism in Pu-Ga alloys at low temperatures, (2) ascertaining the peak-dip-hump structure in photoemission experiments of the spectral function of electrons, and (3) identifying the pairing symmetry in the multiband superconductor $PuCoGa_5$, where interband pairing with nodal gap functions may exist. Confirming such unconventional superconductivity would place $PuCoGa_5$ in the same class of high-temperature superconductors as the copper-oxides and iron-pnictides, which are generally thought to be controlled by spin fluctuations.

Antiferromagnetism in the Pu-Ga Alloy

Disorder-Induced Static Magnetism

Contrary to many experimental observations until now, DFT predicts the formation of long-range ordered spin and orbital moments in plutonium metal. The upper bound for the "nearly static" magnetic moment in δ-Pu was determined to be less than 0.001 μ_{Bohr}. This determination by muons indicated that δ-Pu is paramagnetic at timescales longer than a few microseconds, because there is no measureable net magnetism. Alternatively, the moment could be much larger on shorter timescales but averaging out to near zero during a typical measurement with "slow" time-resolving probes. Using the camera analogy again, it would be like taking a picture of a fast-moving object with a slow shutter. The fact that the spin and orbital moments are predicted to cancel each other because of their antiparallel alignment may also explain many observations of plutonium's nonmagnetic nature.

To reconcile DFT predictions with experiments, it is possible to either include temporal fluctuations within various dynamical mean-field theory approaches, as pioneered by the Rutgers group, or propose spatial fluctuations within a disorder moment model. Consider the disorder model as a poor-man's solution to treating the effects of magnetic fluctuations within a static mean-field theory—it mimics in real space time averages of dynamic fluctuations or freeze frames of almost perfectly cancelling random orientations of magnetic moments. Although a simpler model, the static magnetic disorder may capture most of the essential physics of the electronic structure in plutonium.

Crystalline-perfect antiferromagnetic δ-phase plutonium is mechanically unstable against shear deformations and cannot exist at low temperatures, although DFT calculations predict that such a magnetic configuration

does not have the lowest ground-state energy. These observations are fully consistent with the elemental δ-Pu not existing at lower temperatures; it is only stabilized thermally, where the static DFT model predicts magnetic disorder. In Figure 1, we see the mechanical instability for the face-centered cubic (fcc) phase occurring for a tetragonal distortion with a c/a axial ratio less than the ideal 1.414.

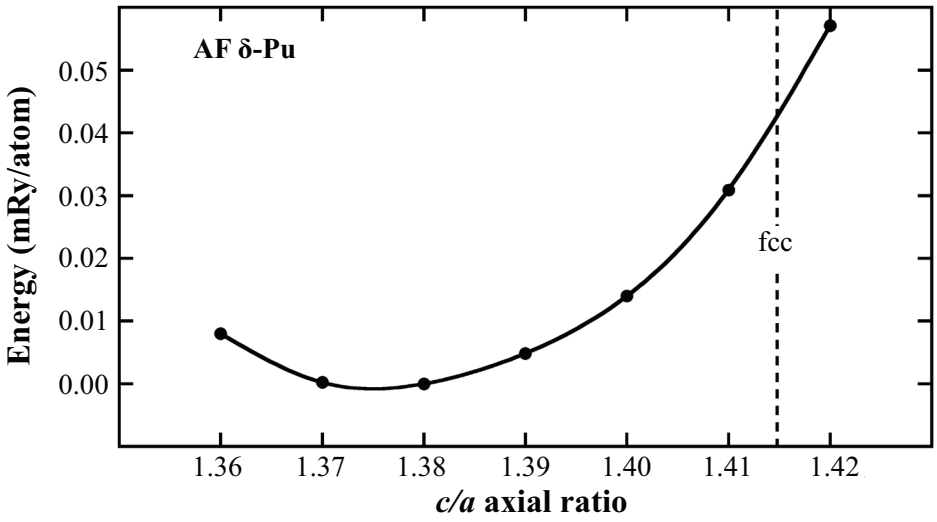

Fig. 1. This graph shows the ground-state energy of elemental δ-phase plutonium with long-range antiferromagnetic order. Signaling the mechanical instability is the minimum at a small lattice parameter ratio c/a compared to the experimental value of the fcc crystal structure.

A possible way around this problem is to recall that measurements are performed on gallium-stabilized δ-phase plutonium rather than elemental δ-phase plutonium. The latter exists only at high temperatures between 600 and 800 Kelvin. Gallium acts like a defect in the plutonium host crystal. By breaking the symmetry of the ground state of elemental δ-phase plutonium, it induces local magnetic moments in its vicinity (Fig. 2). At sufficiently large gallium concentration, the antiferromagnetic puddles start to overlap and long-range magnetic order becomes stable. DFT calculations perfectly capture this experimentally known behavior.

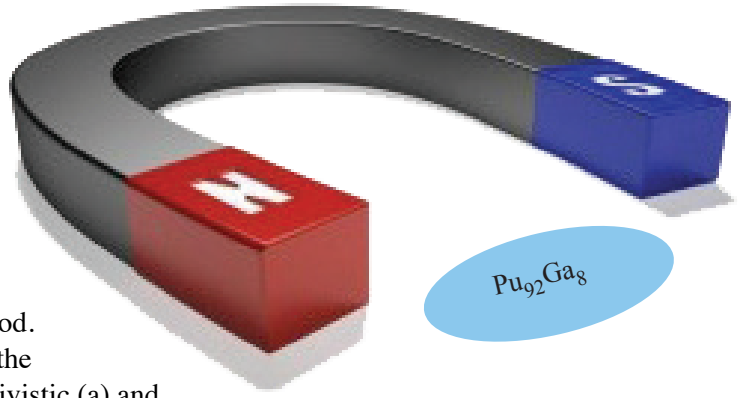

Fig. 2. This image of a horseshoe magnet illustrates the defect-induced magnetic moment in the alloy $Pu_{92}Ga_8$.

To determine if such defect-induced, long-range magnetic order is possible within a static mean-field treatment, we include spin–orbit interaction in the DFT electronic structure calculation within a super-cell method. The total energy curves as a function of the *c/a* ratio of the lattice parameters (Fig. 3), with results from scalar relativistic (a) and spin–orbit-interaction calculations (b). Notice that including spin-orbit interaction stabilizes the fcc structure at approximately 8% gallium and higher. For the 12% gallium alloy, we find that adding orbital polarization (SO + OP, dashed line) does not significantly affect the results and conclusion. This is in contrast to elemental δ-Pu, where it is very important.

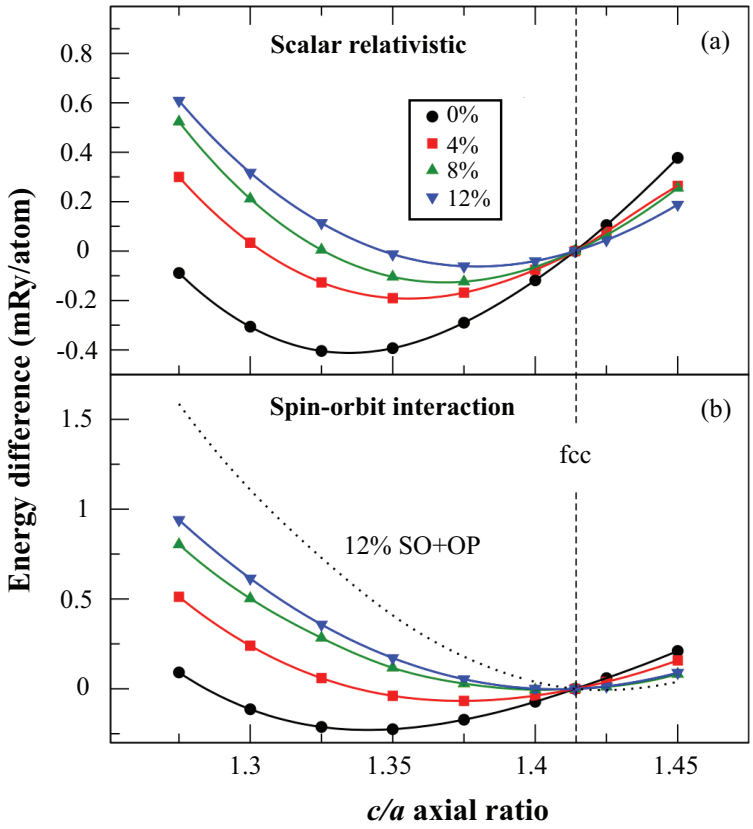

Fig. 3. These graphs show calculated self-consistent full-potential linearized muffin-tin orbital (FPLMTO) total energies, relative to that of fcc, as functions of axial c/a ratio for unalloyed plutonium and three Pu–Ga alloys. The upper panel (a) shows results from a scalar relativistic treatment. The lower panel (b) includes in the calculations the spin-orbit interaction. For comparison, one set of calculations (12% gallium) is performed, including orbital polarization (dotted line, no symbols) in panel (b). The vertical dashed line indicates the fcc crystal structure. Lines connecting the symbols are guides for the eye only.

Spin Fluctuations in $PuCoGa_5$

Peak-Dip-Hump Feature in the Spectral Function of the Normal State

In previous work, we presented evidence for the importance of the dynamics of spin fluctuations in the normal state of the isostructural superconductors $PuCoIn_5$, $PuCoGa_5$, and $PuRhGa_5$. We used first-principles DFT electronic structure calculations as input for the multiband spin susceptibility in a self-consistent quasiparticle-GW approximation of the correlated electron self-energy. This is a perturbative dynamical mean-field theory incorporating the dynamic and momentum-dependent correlation effects in the self-energy.

In the normal state, we discovered the presence of a strong peak at approximately 0.5 eV in the mean-field self-energy, with an energy scale set by the spin-orbit-split *5f* electron states. Further, these particle-hole fluctuations couple to the single-particle spectrum, giving rise to the peak-dip-hump feature in the photoemission spectrum, which is otherwise characteristic of the coexistence of itinerant and localized electronic states. The redistribution of states with a peak at the Fermi energy leads to mass enhancement of the itinerant electrons. When combined with additional enhancement as a result of electron-phonon coupling, such mass renormalization is in fair agreement with low-temperature measurements of the Sommerfeld coefficient in the specific heat.

Multiband Superconductivity with Nodal Gap Functions

We still do not know the nature of the pairing in the unconventional superconductor $PuCoGa_5$. Thus, it is quite natural to draw analogies with the copper-oxide high-temperature superconductors. In such superconductors, power laws in the temperature behavior of many physical observables are consistent with d-wave pairing and nodes in the gap function on the Fermi surface. Because we lack phase-sensitive probes that keep us from determining the sign of the gap function in $PuCoGa_5$, virtually all experiments are interpreted in terms of an oversimplified single-band d-wave theory of superconductivity. A theory that also accounts remarkably well for reported power laws in temperature of thermodynamic measurements, as well as for Andreev reflection in point-contact spectroscopy.

Taken together, these measurements point toward the existence of nodal quasiparticle states. It is important to question if other pairing symmetries within a multiband theory of superconductivity can equally describe existing experiments, as well as propose discriminating future experiments. It is thus natural to explore the mechanism of spin fluctuations as the mediating glue for spin-singlet superconductivity in this material.

As we know from our earlier work, $PuCoGa_5$ possesses a strong particle-hole continuum spectrum of spin fluctuations in the normal state. This spectrum might give rise to unconventional pairing and even exotic pairing symmetries in a multiband scenario of superconductivity, considering the presence of anisotropic three-dimensional (3D) and quasi-2D Fermi surfaces shown in Fig. 4. Therefore, a study of the magnetic spin susceptibility may provide the answer to the question of whether the spin-fluctuation theory of superconductivity can account for gapless behavior or nodal quasiparticle states in the excitation spectrum. For comparison, the existence of nodal quasiparticle states is well established in copper-oxide and some heavy-fermion superconductors but not in iron-pnictide superconductors.

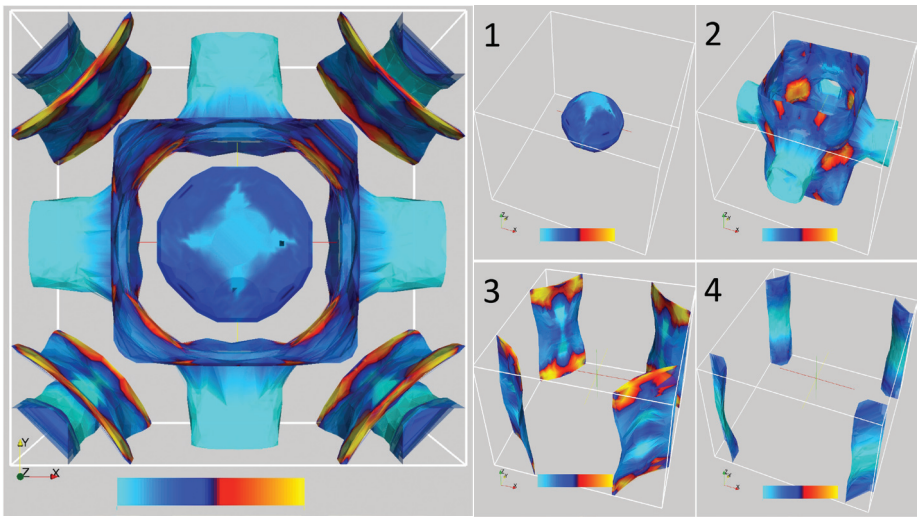

Fig. 4. The electronic hotspots on the Fermi surfaces of $PuCoGa_5$ with two 3D hole pockets near the Γ point (center) and two quasi-2D electron pockets near the M point (corner). The left panel shows a top view of the Fermi surfaces. The right panel consists of 3D views of each Fermi surface, as labeled by its band index (1–4). Areas of increased nesting—that is, electronic hotspots on the Fermi surface, are shown in yellow in the colormap, ranging from turquois to blue to red to yellow. The colormap depicts the hotspot values of the joint density of states (JDOS) at the dominant nesting vector Q = (π, π, π) obtained from the DFT band structure. Nesting is strongest between bands 2 and 3 (yellow hotspots), suggesting spin-fluctuation-mediated interband scattering with the possibility of interband pairing.

Electronic Hotspots, Nesting, and Maps of Joint Density of States

Our previous DFT studies of the magnetic spin susceptibility suggest the existence of nodal d- or $s^{\pm}$-wave gap functions in this material—these studies assume that superconductivity is mediated by spin fluctuations. In Fig. 4, our material-specific calculations paint a picture of the dominant Fermi surface hotspots; i.e., interband scattering channels, as can be seen from the colormap of the joint density of states (JDOS), superimposed onto the Fermi surfaces. The JDOS describe the scattering condition of electrons between Fermi surfaces caused by spin fluctuations with scattering wave vector q, which must satisfy both momentum and energy conservation (nesting). The intensity of the JDOS is a rough measure of the static magnetic spin susceptibility $\chi^0(q, \Omega=0)$.

A clearer picture of the dominant nesting vectors can be gleaned by analyzing the static spin susceptibility $\chi^0(q, \Omega=0)$ shown in Fig. 5. The relevant hotspots responsible for Fermi surface nesting are primarily aligned along the wave vector $Q = (\pi, \pi, \pi)$. For ease of comparison, a 3D visualization of the hotspots for each Fermi surface is given in the right-hand-side panels of Fig. 4. A Fermi surface degeneracy caused by nesting may induce a sign-reversal of the gap function similar to the high-temperature copper-oxide superconductors or iron-based pnictides. Such a result is consistent with calculations of the spin susceptibility shown in Fig. 5.

A closer inspection of the right-hand-side panels in Fig. 4 shows that the dominant nesting at wave vector $Q = (\pi, \pi, \pi)$ occurs between Fermi surfaces of bands 2 and 3, which exhibit the highest JDOS in the intensity colormap (yellow). To a lesser extent, Fermi surface nesting also occurs between bands 1 and 4.

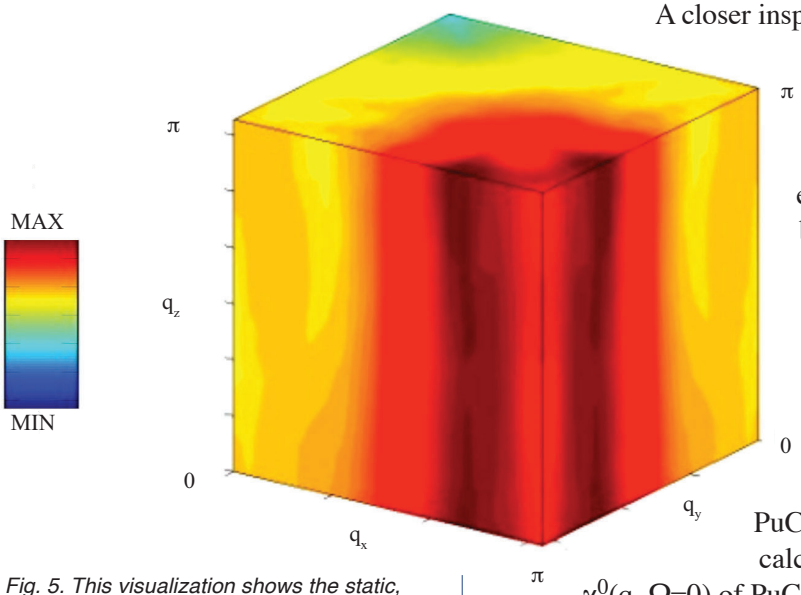

Fig. 5. This visualization shows the static, bare magnetic spin susceptibility χ0(q, Ω=0) of $PuCoGa_5$ in momentum transfer or q space. The highest intensity occurs near the nesting wave vectors $Q \sim (\pi, \pi, q_z)$, which dominate the pairing interaction.

Magnetic Spin Susceptibility

As mentioned before, the measured anomalous temperature behavior of the spin-lattice-relaxation rate $1/t_1$ in the normal state indicates that spin fluctuations play an important role for superconductivity in $PuCoGa_5$. Figure 5 shows a volume-rendered, DFT-calculated unrenormalized static spin susceptibility $\chi^0(q, \Omega=0)$ of $PuCoGa_5$. This figure shows the highest intensities occurring in the vicinity of the nesting wave vectors $Q \sim (\pi, \pi, q_z)$ with $0<q_z<\pi$. Taken at face value, this result points toward more 3D-like superconductivity, although the pairing gap function is quasi-2D.

The DFT-calculated nesting is consistent with both nodal d- and $s^{\pm}$-wave pairing. The key result is that both nodal d- and nodal $s^{\pm}$-wave gaps support the existence of nodal quasiparticles, which should be observable in momentum- and energy-dependent magnetic resonance spectra of inelastic neutron scattering. A nodal $s^{\pm}$ state is also consistent with reports of the signature of Andreev reflection and a zero-bias voltage peak in $PuCoGa_5$.

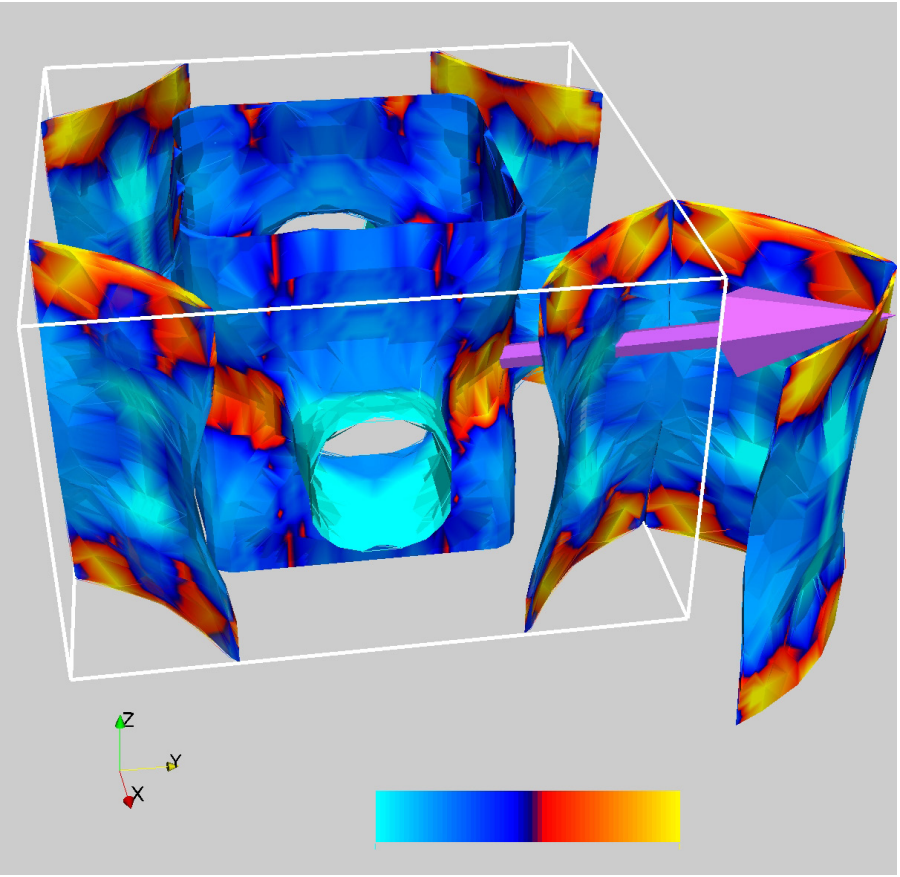

Fig. 6. This image shows the nesting vector (magenta arrow) between Fermi surfaces of bands 2 and 3 with vector Q≈(π, π, π). As before, the superimposed intensity colormap visualizes the JDOS at the nesting vector (π, π, π).*

So far, these signatures have been interpreted as evidence for $d_{x^2-y^2}$ symmetry within a single-band model, but a more complex scenario emerges when accounting for multiband superconductivity.

Hotspots and Nesting Wave Vector

As shown in Fig. 6, the nesting vector between the Fermi surfaces of bands 2 and 3 is shown connecting two selected hotspots. The JDOS were calculated for nesting vector Q=(π, π, π). For illustration purposes, we drew a magenta vector connecting Fermi surfaces 2 (hole pocket) and 3 (electron pocket) (see Fig. 4) with nesting vector Q*=0.95(π, π, π). As before, we refer to areas of increased nesting on the Fermi surface as electronic hotspots.

Conclusions

In a Pu-Ga alloy, freeze frames of fluctuating spins can give rise to antiferromagnetic puddles in the vicinity of gallium defects, such as were recently observed with inelastic neutron scattering. Increasing gallium concentration causes the puddles to start to overlap. Moreover, at sufficiently high concentration long-range antiferromagnetism becomes established—this phenomenon may have been observed in various magnetization measurements.

Acknowledgments

We are grateful to our long-term collaborators Tanmoy Das, Alexander Landa, and Jian-Xin Zhu for many helpful discussions. The work at LANL was supported over the years by the U.S. Department of Energy under Contract No. DE-AC52-06NA25396 through the LDRD program and the Office of Basic Energy Sciences (BES), Division of Materials Sciences and Engineering. We gratefully acknowledge computing allocations by the National Energy Research Scientific Computing Center, a BES facility, under Contract No. DE-AC02-05CH11231. The work at Lawrence Livermore National Laboratory was performed under the auspices of the U.S. Department of Energy under Contract No. DE-AC52-07NA2734.

In the intermetallic actinide $PuCoGa_5$, dynamic spin fluctuations arise from spin-orbit split *5f* states in the density of states with particle-hole transitions between *5f–5f* and *3d–5f* states. Our calculations suggest the possibility of unconventional superconductivity in $PuCoGa_5$ with nodal d- or $s^{\pm}$-wave gap functions. The symmetry of these functions is caused by spin-fluctuation-mediated Cooper pairing, dominated by nesting around the wave vector $Q \sim (\pi, \pi, \pi)$. As is known from other multiband materials and model systems, such nesting prefers interband pairing with sign-changing gaps. We have identified a common thread between $PuCoGa_5$ and other unconventional superconductors, where spin fluctuations are also thought to be at work. Future systematic studies are required to address the evolution of the spin resonance, spectral function, and gap structure upon entering the superconducting state in this multiband actinide superconductor.

Conducting a Thermal Analytical Study Regarding the Phase Stability of Unalloyed and Alloyed Plutonium

Sue M. Ennaceur
Atomic Weapons Establishment
United Kingdom

Sue Ennaceur discusses reaction parameters that yield reproducible results on phase transformation kinetics and reaction mechanisms.

Plutonium metallurgy remains an active area of research today. Even after decades of study, we still do not fully understand the response of plutonium and its alloys to thermal processes and pressure.

Six allotropic forms, coupled with the complexity of phase transformations, make plutonium a difficult material to control during the manufacturing process. The phase composition and density of plutonium and its alloys, particularly after heating or cooling through phase transformations, are extremely sensitive to many internal and external variables. We must have a fundamental understanding of the phase transformation pathways, including individual process steps along with their kinetics, energy requirements, and history. Such an understanding will lead to a full appreciation of the conditions necessary to initiate and drive the transformations possible in plutonium components.

To achieve such an understanding, research continues into comprehending the lack of reproducibility during plutonium phase transformations. Central to such comprehension is establishing reproducible and valid nonisothermal methods to investigate the kinetics and the reaction mechanisms for solid-solid phase transformations in plutonium.

Over the past few years, the focus of my work at the Atomic Weapons Establishment (AWE) has been to establish conditions for reproducible reaction parameters for solid-phase transformations. Here I present a careful study that revealed thermal-cycling protocols that produce uniquely reproducible results. I then used these protocols as a basis to explore the phase stability of plutonium and its alloys in which the composition included metastable components—that is, phases of plutonium not thermodynamically stable at the temperature of interest. This work produced for the first time a reproducible and complete understanding of the transformation kinetics and reaction mechanisms in the plutonium-gallium alloys studied here.

Background

Plutonium remains a challenging material to study in its elemental form, but even more so when complicated by the effects of chemical additions and impurities, differences in production, heat treatment conditions, and the consequences of its radioactive decay. Plutonium's uniquely complex character is clearly evidenced by its ability to adopt as many as six different allotropic forms between room temperature and its melting point at 640°C (Fig. 1).

The transformation from one crystal structure to the next occurs readily for relatively small changes in temperature and pressure, with large differences in the properties of the phases. On the one hand, the ambient-temperature α-phase (monoclinic) has a high density, is hard and

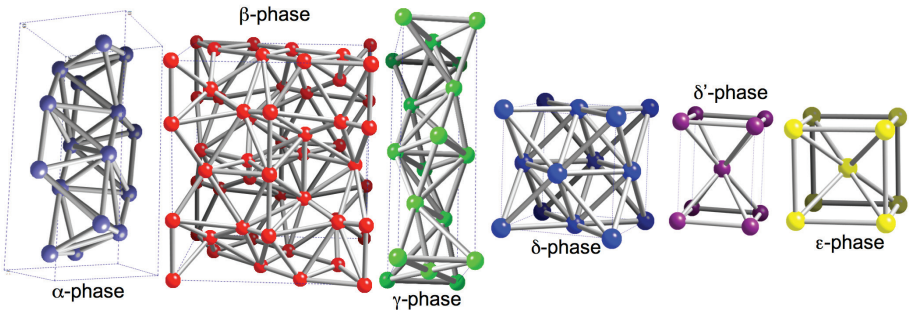

Fig. 1. This illustration shows the six different allotropic forms adopted by unalloyed plutonium between room temperature and its melting point at 640°C.

brittle, and consequently is difficult to manufacture. On the other hand, the high-temperature δ-phase (face-centered cubic, or fcc) is soft and ductile with a 20% lower density than the α-phase.

Stabilizing the metallurgically desirable fcc δ-phase from ambient temperature to 450°C can be achieved by alloying plutonium with a few atomic percent of an element such as gallium, aluminium, cerium, or americium. Such stabilization not only eliminates issues associated with considerable changes in physical properties that arise while thermally processing plutonium (such as volume changes that would cause shrinkage and cracking during cooling from the melt) but also retains the ductility so important for manufacturing processes.

The α-phase (monoclinic) may be induced to form within the stabilized δ-phase, depending on the degree of the alloy's homogeneity and the alloying content, thermal treatment, temperature, and applied pressure. Because of the large differences in properties between α- and δ-phase plutonium, we must fully understand the conditions that cause the α-phase to form from the δ-phase, as well as the effect on properties.

State and history strongly influence the controlling factors and mechanisms behind the transformation of a specific plutonium alloy and phase. Each sample of plutonium is unique to a certain degree, depending on the specific material production and processing conditions, the homogeneity, the grain size, the variations and distribution of impurities and defects, and history.

Measuring How the δ-Phase of Plutonium Responds to Temperature

Work first began by developing an essential precursor to an accurate descriptor of gallium-stabilized δ-phase behavior under changing conditions of temperature and pressure. Applying a systematic study using differential scanning calorimetry (DSC), I, for the first time, established a set of reproducible reference conditions designed to determine the phase-transformation parameters, reaction kinetics, and mechanisms in a reference gallium-stabilized δ-plutonium alloy. The intent was to compare such results against the reaction mechanisms and behavior of other plutonium alloys of different chemical compositions and conditioning. My end goal was to understand further the effects of impurities and different thermal treatments on phase transformations in gallium-stabilized δ-plutonium.

Once reproducibility was established, it was possible to perform studies on two homogeneous fully δ-phase stabilized Pu-Ga alloys of different composition: a plutonium 1 atomic % gallium alloy (Pu-1 at.% gallium) and a plutonium 2 atomic % gallium alloy (Pu-2 at.% gallium). These alloys were chosen because they just straddle an important boundary in how they respond to modest cooling.

A partial transformation of the δ-phase to α-phase occurs upon cooling the alloys to subambient temperatures. This phase is referred to as α'-phase; its only difference from the α-phase of the unalloyed plutonium is that its lattice is expanded by gallium atoms occupying substitutional positions.

In a number of comprehensive studies conducted by Kerri Blobaum and Jason Jeffries and their colleagues at Lawrence Livermore National Laboratory (LLNL), it was found that the α'-phase, which is induced by low-temperature conditioning in Pu-2 at.% gallium alloys, will revert directly to the δ–phase via a martensitic cascading transformation mechanism. This mechanism is evidenced by a series of endothermic peaks.

Not so straightforward is the transformation back to δ-phase of α'-phase induced in Pu-1 at.% gallium alloys following low-temperature treatment. It has been shown to occur via two competing mechanisms, one a more complex process. As for Pu-2 at.% gallium, one mechanism is a direct path of α'-phase to δ-phase (martensitic), thereby recovering completely from the low-temperature anneal. The other, more-complex, mechanism requires taking the alloy quite far up in temperature. As shown in Fig. 2, this is an indirect path, one from α'-phase to β-phase to γ-phase and finally to the desired δ-phase (following a series of nucleation and growth mechanisms) such that only a high-temperature anneal fully recovers the fcc phase.

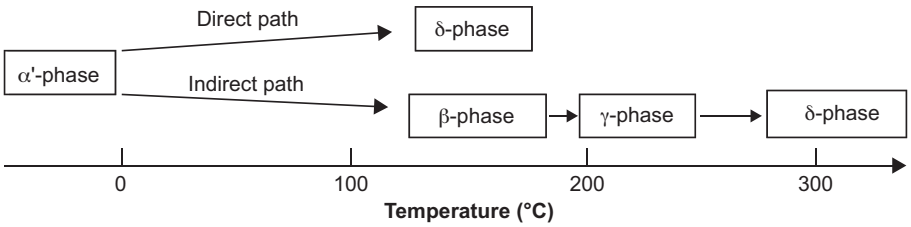

Fig. 2. This diagram shows the competing direct and indirect reverse transformation paths of low-temperature-induced α'-phase back to the δ-phase.

Isothermal XRD (x-ray diffraction) measurements, combined with simulations (CALPHAD method) conducted by Aurelien Perron at LLNL and Brice Ravat and his colleagues at France's Atomic Energy and Alternative Energies Commission, revealed that time-dependant gallium diffusion governed the competition between direct and indirect reversion of α'-phase back to δ-phase. Thermodynamic calculations showed that the direct reversion path would become more favorable as the heating rate increased. The reason for such favorability is that the process would afford less time for the gallium atoms to diffuse.

Advantages of Differential Scanning Calorimetry

The work conducted at AWE has demonstrated the advantages of using DSC to differentiate between the different mechanisms and transformation paths of α'-phase induced in Pu-1 at.% gallium alloys, following low-temperature treatment. The isothermal and athermal character of the

different mechanisms can be used to distinguish between them. Thus, a different mechanism (a martensitic or a nucleation and growth mechanism) and transformation path (direct or indirect) may be favored by conducting recovery anneals, inducing isothermal transformation, and optimizing the heating rates for each transformation.

Determining the transformation path is a necessary ingredient in ascertaining the useful range of temperatures for a stabilized δ-phase alloy-manufactured component to remain free of α'-phase. It provides an understanding as to whether the induced α'-phase transforms directly back to the δ-phase and thus has only a short-lived impact on the alloy's material properties or if it is likely to cause greater, longer-term impact by requiring heating to higher temperatures (360°C) and several phase transformations to revert back to the δ-phase.

The Effects of Pressure

Part of this research involved exploring some effects of pressure, with complicated results warranting further study. Because the α'-phase is so much denser than all the others, it is expected that pressure would disturb thermodynamic stability, which in turn would drive an alloy toward the α'-phase. When subjecting the alloys to compressive pressure between 100 and 300 MPa, a significant percentage of the α'-phase—not surprisingly—was induced in the just-barely-stable Pu-1 at.% gallium-alloy specimens, whereas no detectable levels of α'-phase were recorded in specimens of the Pu-2 at.% gallium alloy.

However, when thermally recycling the specimens from ambient temperature to temperatures within the β-phase stability range, the α'-phase was also detected in the Pu-2 at.% gallium alloy. Furthermore, a significant increase in α'-phase was recorded as both alloys were subjected to an increasing number of thermal cycles (Fig. 3). The increase in α'-phase content reached a plateau after a given number of cycles for each alloy. The Pu-2 at.% gallium alloy does not appear to have initially transformed under the applied compressive stress.

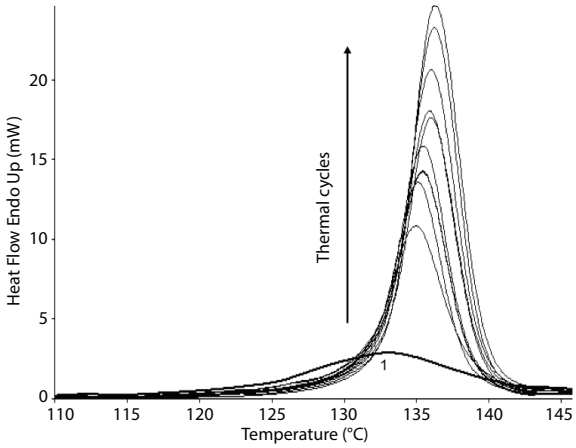

Fig. 3. These DSC thermograms are for the same specimen of Pu-1 at.% gallium alloy. They reveal an increase in α'-phase as a function of thermal cycling after the specimen was subjected to compressive stress in the 100–300 MPa range.

However, there was a hidden effect in that the alloy apparently had been seeded with α'-phase embryos that produce increasing amounts of α'-phase when given sufficient stimulus. Initiated by compressive pressure in the 100–300 MPa range, the transformation of δ-phase to α'-phase has the characteristics of a martensitic mechanism, with the α'-phase forming by short bursts that appear to be driven by stress. Generating the stress that drives the transformation required heating the specimens through the α'-phase to β-phase transformation, followed by cooling the specimens through β-phase to α'-phase transformation, with the associated large-volume changes. Inducing compressive pressure in the 100–300 MPa range and thermal cycling caused the transformation of the α'-phase to follow an indirect path to the δ-phase in the Pu-1 at.% gallium and Pu-2 at.% gallium alloys.

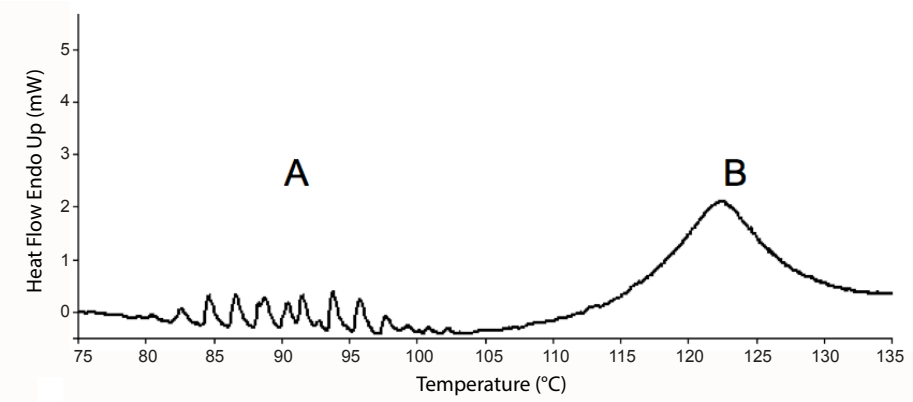

Fig. 4. This DSC thermogram shows (A) the direct α'–δ phase (burst) transformation and (B) indirect α'–β phase transformation in a specimen of the Pu-2 at.% gallium alloy after being subjected to compressive stress of 600±50 MPa.

Increasing the compressive pressure to 600±50 MPa induced a significant increase in the percentage of α'-phase in the Pu-1 at.% gallium alloy. However, thermally cycling the specimens decreased the α'-phase content to levels comparable to that obtained for the lower pressure regime followed by thermal cycling. Transformed via heating to the β-phase (following the indirect transformation path), more than 20% of the α'-phase appears to have reverted back to the δ-phase when cooled to ambient temperatures.

The α'-phase formed by increasing compressive pressure to 600±50MPa in specimens of Pu-2 at.% gallium alloy. Thermal analysis revealed that two different transformations were occurring, with (1) a portion of the α'-phase formed in the Pu-2 at.% gallium alloy transforming directly back to the δ-phase and (2) the remainder transforming to the β-phase (indirect path), as shown in Fig. 4. Furthermore, approximately 50% of the β-phase that formed appeared to have reverted back to the δ-phase upon cooling the specimens to ambient temperatures. It would appear that the α'-phase formed as a consequence of the increase in compressive pressure has different degrees of stability, which may be dependent on the microenvironment of the α'-phase particles formed and the capacity of the δ-phase matrix to accommodate the induced α'-phase.

Further Reading

S. S. Hecker and M. F. Stevens, "Mechanical Behaviour of Plutonium and its Alloys," *Los Alamos Science* **26**, Los Alamos National Laboratory (2000).

J. N. Mitchell, M. Stan, D. S. Schwartz, and C. J. Boehlert, "Phase Stability and Phase Transformations in Plutonium and Plutonium-gallium Alloys," *Metall, Mater, Trans.* **35A**, 2278 (2004).

J. R. Jeffries, K. J. M. Blobaum, M. A. Wall, and A. J. Schwartz, "Reproducible Phase Transformation in a Single Pu-1.9 at.% Ga specimen," *J. Nucl. Mater.* **384**, 222–225 (2009).

A. Perron, B. Ravat, B. Oudot, F. Lalire, K. Mouturat, and F. Delaunay, "Phase Transformations in Pu-Ga alloy, Synergy between Simulations and Experiments to Elucidate Direct and Indirect Reversion Competition," *Acta. Mater.* **61**, 7109 (2013).

B. Ravat, B. Oudot, A. Perron, F. Lalire, and F. Delaunay, "Phase Transformations in PuGa 1at.% Alloy, Study of Whole Reversion Process Following Martensitic Transformations," *J. Alloys and Compounds* **580**, 298–309 (2013).

S. M. Ennaceur, "Methodology for Describing the α ↔ β Phase Transformation in Plutonium," *Thermochim. Acta* **539**, 84–91 (2012).

S. M. Ennaceur, "A Differential Scanning Calorimetry Study of the Kinetics of the β → γ Phase Transformation in Plutonium," *Thermochimica Acta* **547**, 99–105 (2012).

S. M. Ennaceur, "The Effects of Thermal Conditioning and Recovery Processes on the δ → γ Phase Transformation Mechanisms in Plutonium," *Thermochim. Acta* **565**, 151–158 (2013).

S. M. Ennaceur, "Phase Stability of α-Phase in a Pu-1 at.% Ga Alloy Following Low Temperature Treatment, *Thermochim. Acta* **593**, 22–29 (2014).

Element 94: The Eighth Plutonium Futures—The Science Conference

September 7–12, 2014
Renaissance Hotel, Las Vegas, Nevada

230 attendees from 13 countries

Sponsored by the American Nuclear Society
Cosponsored by Lawrence Livermore National Laboratory and Los Alamos National Laboratory

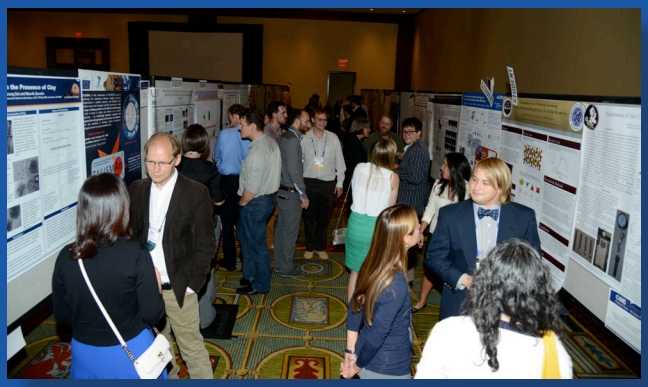

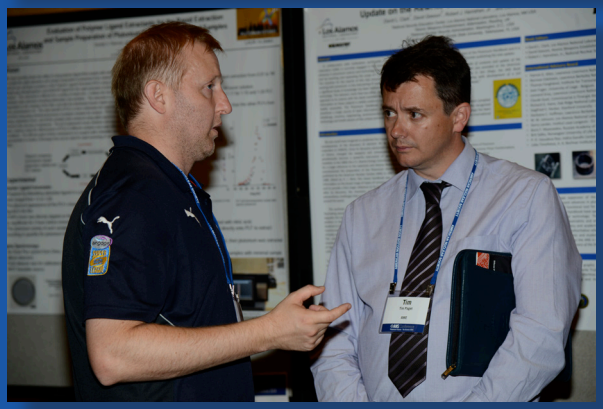


ANS Conference
Plutonium Futures - The Science 2014
Metallurgy and Materials S
10:20 a.m.-12:00 p.m.
Metallurgy and Materials S
1:00 p.m.-3.00 p.m.
Metallurgy and Materials S
3:20 p.m.-5:00 p.m.


AMERICAN NUCLEAR SOCIETY


AMERICAN NUCLEAR SOCIETY



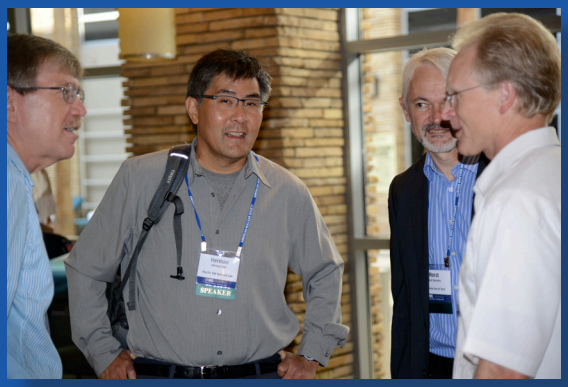






RENAISSANCE


SPEAKER


AMERICAN NUCLEAR SOCIETY


Atomic Testing Museum


WESTGATE


AMERICAN NUCLEAR SOCIETY

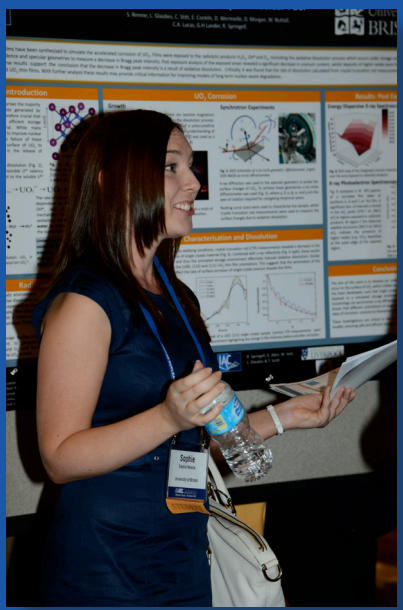

Plutonium Complexation with Natural Organic Matter

Mark A. Boggs, Harris E. Mason, Zurong Dai, Mavrik Zavarin, and Annie B. Kersting
Glenn T. Seaborg Institute
Physical & Life Sciences
Lawrence Livermore National Laboratory

Plutonium speciation and reactive transport in complex biogeochemical environments remains an important area of study. Such study is particularly important because countries such as the United States are developing safe and effective long-term storage repositories for nuclear waste. Moreover, such countries also wish to implement the best methods designed to clean up currently contaminated environments.

One example of a contaminated site is the Nevada National Security Site (NNSS), located in Nevada. This site has released approximately 4.8 x 10^{18} becquerel of plutonium into the subsurface. Recent field studies conducted at NNSS, as well as at Rocky Flats in Colorado, have attributed higher-than-predicted plutonium mobility resulting from a high concentration of dissolved organic matter in the water. Such studies highlight the importance of understanding how different sources of organic matter influence plutonium environmental behavior.

Classification of Humic Substances

Humic substances are naturally occurring large organic molecules derived from organic matter degrading in the environment. Two major classifications of humic substances are humic acid (HA) and fulvic acid (FA), which are differentiated from one another by their solubility properties at different pH levels. HA is insoluble at low pH, whereas FA is soluble at all pHs. In addition to solubility, HA has greater carbon content and is generally larger than FA.

The structure and composition of HA and FA varies from source to source, but compositionally they consist mostly of carbon, hydrogen, and oxygen; in some cases there can be found small amounts of nitrogen, phosphorous, or sulfur. Humic substances contain carboxylic acid groups that can form strong complexes with metals, including radionuclides. Such complexes have increased solubility and make the metals more mobile in the environment.

Comparing Fungal Siderophores such as Desferrioxamine B with Humic Substances

A number of bacteria and fungi produce strong metal complexants called siderophores, primarily as a tool to solubilize iron necessary for their metabolic activity. In contrast to the carboxylic acid functional groups of HA and FA, fungal siderophores such as desferrioxamine B (DFOB) contain hydroxamic acid functional groups (Fig. 1). Although siderophores are designed for iron complexation, they can also form strong complexes with most metals.

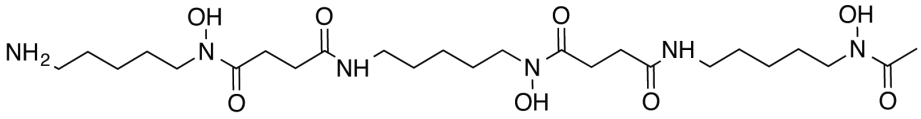

Fig. 1. The structure of desferrioxamine B.

Mark Boggs discusses the complexity of plutonium chemistry in the environment and the need to study directly plutonium complexes.

A phyllosilicate clay mineral, montmorillonite [$(Na,Ca)_{0.33}(Al,Mg)_2(Si_4O_{10})(OH)_2 \cdot nH_2O$] consists of two tetrahedral sheets on either side of an octahedral sheet. In addition to being ubiquitous in the environment, montmorillonite is a primary component of bentonite, a natural-rock material many countries have proposed as backfill for long-term radioactive waste disposal sites. Although it is known that plutonium sorbs readily to montmorillonite, it is unknown what effect natural organic matter may have on sorption of plutonium in the presence of montmorillonite. The work presented in this article examines the effect of naturally occurring organic matter on sorption of Pu(IV) to montmorillonite.

Plutonium-IV and Montmorillonite

Figure 2 compares the sorption of Pu(IV) to montmorillonite in both the absence and presence of organic substances. In the absence of any complexing ligands, sorption is greatest between pH 4 and 6. Sorption decreases under alkaline conditions, which may be attributed to Pu(IV) hydrolysis and the formation of aqueous carbonate complexes at higher pH.

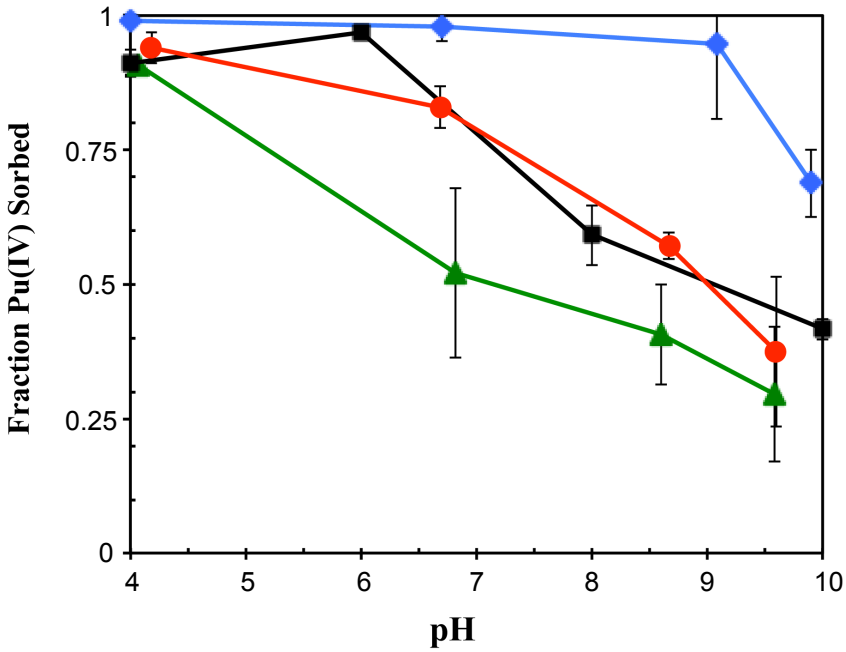

Fig. 2. This graph shows the fraction of Pu(IV) sorbed to montmorillonite as a function of pH. Shown are data with no complexant (black squares), 0.8 ppm HA (green triangles), 0.8 ppm FA (red circles), and 0.8 ppm DFOB (blue diamonds).

The presence of HA significantly decreased the total sorption of Pu(IV) to montmorillonite. At a pH greater than 6, total Pu(IV) sorption to montmorillonite decreased by 20 to 50% relative to the binary system. At pH 6, a nearly 50% decrease in Pu(IV) sorption is observed. The observed decrease in Pu(IV) sorption to montmorillonite at pH greater than 4 is most likely the result of greater stability of the Pu(IV)-HA aqueous complex relative to Pu(IV) surface species. In these experiments, the presence of HA resulted in increased aqueous plutonium concentrations compared to the HA-free system.

Compared to the binary system at near neutral pH, sorption of Pu(IV) to montmorillonite in the presence of FA resulted in only a minimal decrease in Pu(IV) surface sorption. No decrease in Pu(IV) sorption relative to the

binary system was observed in the Pu(IV)-FA-montmorillonite system at neutral pH, although the overall trend remained consistent with Pu(IV)-HA results. Humic acid decreased Pu(IV) surface sorption to a greater extent than FA at pH greater than 4. This decrease was attributed to Pu(IV)-HA metal complexes being stronger than Pu(IV)-FA.

In contrast to the behavior of the HA and FA, the DFOB system showed an increase in sorption compared to the binary system at pH greater than 4, providing evidence for the formation of ternary sorption complexes.

X-ray diffraction (XRD) enabled further analyzes of the interaction between montmorillonite and DFOB. Figure 3 shows the resultant XRD patterns obtained from 3° to 10° (2θ). In these diffraction patterns, a dominant peak and a broad shoulder occurs at low angle in the patterns of DFOB concentration lower than 1000 parts per million (indicated by upward arrowheads). The dominant peaks are representative of the basal spacing of the predominant clay, d_{001}, that can be determined according to Bragg's law:

$$2d\sin\theta = \lambda ,$$

where θ is the diffraction angle, d is the spacing between crystal planes, and λ is the wavelength of the x-ray source [for copper target: λ ($K_{\alpha 1,2}$) = 1.5418 Å]. An increased basal spacing of d_{001} was observed once the DFOB concentrations were increased to greater than 10 parts per million. A maximum distance of 18.5 Å occurred at 10 000 parts per million DFOB. No evidence of secondary mineral formation was observed, suggesting the montmorillonite was not altered during the experiment. These results suggest that the DFOB is contained primarily within an expanding clay interlayer. Both DFOB and Pu(IV)-DFOB remained in the clay interlayer over the timeframe of these experiments.

The exact mechanism of DFOB accumulation in the montmorillonite interlayer remains uncertain. Pu-DFOB complexes tend to be positively charged. Such complexes may use a cation exchange mechanism to access the interlayer. Very high adsorption of inorganic cations has been previously observed with clays. Although little is currently known about the structure of Pu-DFOB complexes, changes in DFOB structure—from linear to cyclical—may also increase a structure's ability to access the interlayer.

A powerful technique, nuclear magnetic resonance (NMR) spectroscopy can analyze samples under a range of conditions and environments. Paramagnets such as plutonium are typically considered hindrances to NMR analysis because of the possibility of signal broadening and large changes in chemical shifts. If used properly, as in this study, such paramagnetic effects can be used to gain structural information on organometallic complexes.

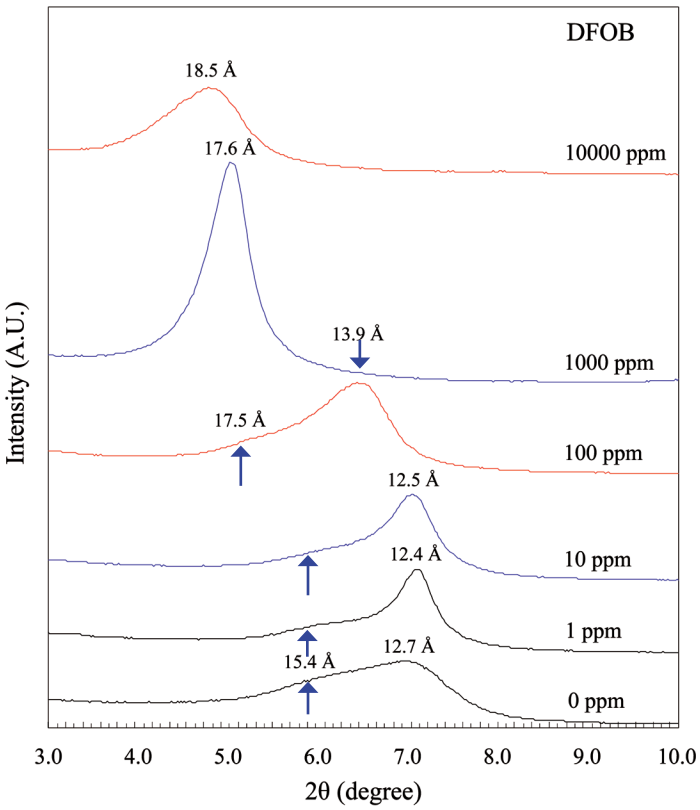

Fig. 3. These x-ray diffraction patterns show 5 mg of sodium montmorillonite in 1.0 mL of 0.01 NaCl with 0-ppm DFOB (green), 1-ppm DFOB (mocha), 10-ppm DFOB (blue), 100-ppm DFOB (red), 1000-ppm DFOB (purple), and 10,000-ppm DFOB (yellow).

Because the effects of paramagnetic relaxation decrease with distance from the metal center, tracking paramagnet effects serves as a powerful method that can help researchers better understand metal binding and elucidate structural information.

We investigated Pu(IV)-DFOB complexes formed at pH 1.0 and pH 6.0 in aqueous media. Line broadening was observed in both Pu(IV) complexes, compared to the uncomplexed sample, although it was more pronounced in the pH 6.0 species. The line broadening primarily affects protons located near the complexing hydroxamate groups, which are located at 2.5, 2.8, and 3.6 parts per millions in uncomplexed DFOB. Such broadening can be attributed to the paramagnetic nature of Pu(IV). The increase in broadening for the pH 6.0 species can be caused by an additional metal in the complex or a decrease in the plutonium oxygen bond distance, indicating the possible presence of a dimeric Pu(IV)-DFOB species.

Complexation with Pu(IV) resulted in an increase in the signal from the amine protons, indicating a decrease in ^{1}H exchange rate with the aqueous solution. Such a decrease is attributed to the low solution pH and the proximity of the protons to a large metal, such as plutonium. Taken from one-dimensional experiments, proton peak assignments were used, in conjunction with 2D $^{13}C\{^{1}H\}$ heteronuclear multiple quantum correlation spectroscopy (HMQC) and ^{1}H-^{1}H correlation spectroscopy (COSY), to correlate the ^{1}H and ^{13}C to determine peak assignments and qualitative structural information.

Figure 4 shows the ^{1}H-^{1}H phase-sensitive COSY spectra investigated for the uncomplexed DFOB and the two Pu(IV)-DFOB complexes.

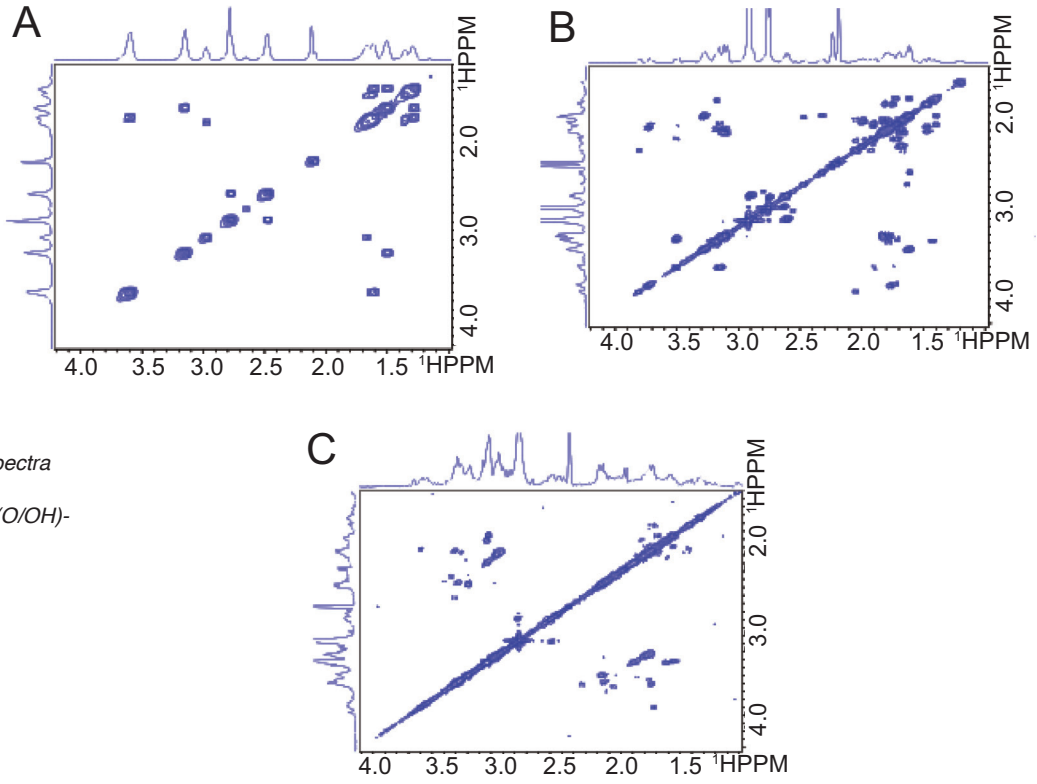

Fig. 4. ^{1}H-^{1}H phase-sensitive COSY Spectra for (A) uncomplexed DFOB, (B) Pu(IV) H_2DFOB^{4+}, and (C) Pu(IV)DFOB-di-μ-(O/OH)-Pu(IV)DFOB.

Using 2D ^{1}H-^{1}H phase-sensitive COSY, the proton peaks in each complex were identified by comparing them with uncomplexed DFOB. Comparing the COSY spectra, it can be seen that the majority of the correlations between the ^{1}H peaks remain constant with and without plutonium complexation, although peak splitting and shifting are observed. Shifts caused by plutonium's paramagnetic nature are observed primarily in the protons located closest to the binding hydroxamate groups at circa 3.5 and 1.5 parts per million; these increase for the higher pH complex.

Peak splitting occurring in the Pu-DFOB complexes was relatively minor and is associated with the rearrangement of the carbon backbone after complexation. Combining these results with those of HMQC and x-ray absorption spectroscopy, we successfully identified two distinct Pu(IV)-DFOB complexes: (1) $Pu(IV)H_2DFOB^{4+}$ (Fig. 5) at pH 1.0 and (2) the dimeric Pu(IV)DFOB-di-μ-(O/OH)-Pu(IV)DFOB at pH 6.0.

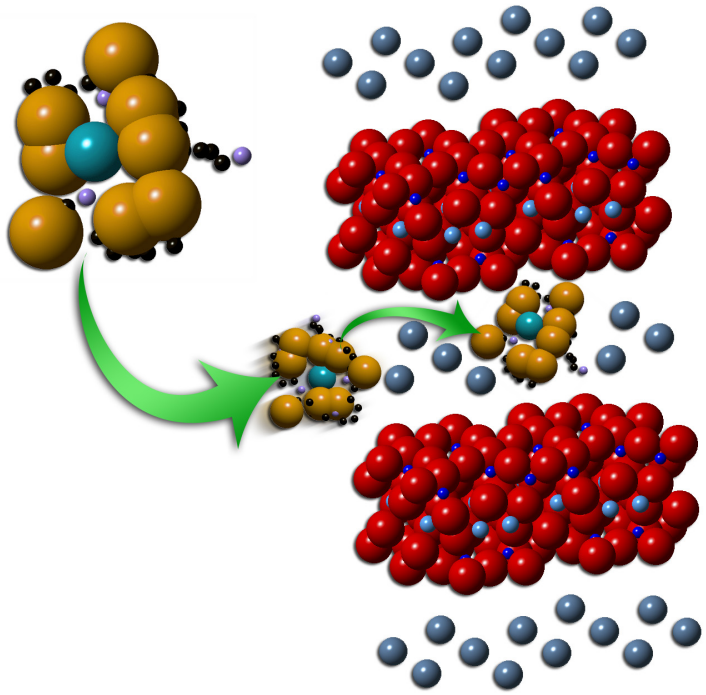

Fig. 5. This illustration shows sorption of the $Pu(IV)H_2DFOB^{4+}$ complex into the montmorillonite interlayer.

Conclusion

We have observed differences in Pu(IV) sorption to montmorillonite in the presence of organic matter. These differences are dependent on pH, as well as the metal ligand complex's stability. In the HA and FA systems, the Pu(IV) sorption processes are predominately controlled by competition between binary surface sorption and aqueous complexation. Sorption of DFOB is controlled by interactions with the interlayer of montmorillonite.

The intercalation of DFOB and the Pu(IV)-DFOB complex into the layered structure of montmorillonite suggests that both Pu(IV) and DFOB

Acknowledgments

This work was supported by the Subsurface Biogeochemical Research Program of the U.S. Department of Energy's Office of Biological and Environmental Research. This paper was prepared by Lawrence Livermore National Laboratory under Contract DE-AC52-07NA27344. LLNL-JRNL-665914.

will remain irreversibly bound. Note that colloid-facilitated plutonium transport may be enhanced if the Pu(IV)-DFOB complex is irreversibly bound in the clay interlayer and inaccessible to desorption processes. Using NMR, we have characterized two distinct Pu-DFOB complexes under low and neutral pH conditions. The stability of these complexes will ultimately determine their mobility and availability in the biosphere.

These studies highlight the complexity of plutonium chemistry in the environment and the need to directly study plutonium complexes, particularly from the standpoint of plutonium mobilization by a broad range of natural organic compounds.

Further Reading

M. A. Boggs, H. Mason, Y. Arai, B. A. Powell, A. B. Kersting, and M. Zavarin, "Nuclear Magnetic Resonance Spectroscopy of Aqueous Plutonium(IV) Desferrioxamine B Complexes," *European Journal of Inorganic Chemistry* **21**, 3312–3321 (2014).

M. A. Boggs, Z. Dai, A. B. Kersting, and M. Zavarin, "Plutonium(IV) Sorption to Montmorillonite in the Presence of Organic Matter," *Journal of Environmental Radioactivity* **141**, 90-96 doi: 10.1016/j.jenvrad.2014.12.005 (2015).

An Overview of Geochemical Reactions Controlling Plutonium's Environmental Mobility

Brian A. Powell
Environmental Engineering and Earth Sciences
Clemson University

One of the largest and most technically challenging projects in actinide science is the cleaning up of legacy wastes from weapons production at Department of Energy sites [National Research Council, 2000]. This cleanup effort involves stabilizing radionuclide-bearing wastes in engineered materials, such as glass, ceramics, and cement, so that they are suitable for long-term isolation and remediating environmental systems that have suffered as a result of the disposal of radioactive waste into unlined or minimally engineered seepage basins. Another issue is addressing largescale nuclear disasters at places such as Windscale (England, 1957), Chernobyl (Russia, 1986), Three-Mile Island (United States, 1979), and Fukushima Daiichi (Japan, 2011). All these disasters have produced widespread radionuclide environmental contamination.

Overview of Plutonium and its Environmental and Health Effects

Although high-specific-activity fission products make up most of the radionuclide releases, plutonium and other actinides are included and present significant long-term health risks. Similarly, evaluations of longterm radiotoxicity in spent nuclear fuel have indicated that long-lived and abundant isotopes such as ^{237}Np and ^{239}Pu represent major long-term dose contributors. As reported by Kersting [2013], plutonium's global inventory in 2010 was 1900 tons. This inventory is expected to rise by 70 to 90 tons every year. To determine effective remediation strategies for existing contamination and to design effective radionuclide waste disposal systems, researchers must gain a detailed understanding of the fundamental chemical, biological, and physical processes that control the mobility of plutonium and other actinides in both engineered and natural systems.

Plutonium remains one of the most complicated elements on the periodic table. Under environmental conditions, plutonium has four accessible oxidation states (III–VI). Under specific conditions, these four states can exist simultaneously [Cleveland, 1979].

Figure 1 shows a general simulation of the variability in plutonium's redox speciation in natural waters. Although these simulations are based on generic water chemistries, the results demonstrate the wide range of oxidation-state distributions expected in natural waters. This sensitivity to redox speciation complicates predictions of plutonium mobility in environmental systems because such mobility is profoundly influenced by oxidation state [Kersting, 2013; Maher et al., 2012; Choppin et al., 1997; Silva and Nitsche, 1995].

Further complicating matters are variations expected for each oxidation state with respect to aqueous speciation, solubility, direct/indirect biological interactions, and interactions with mineral phases. In general, Pu(IV) is

Brian Powell provides a detailed overview of geochemical reactions controlling plutonium's environmental mobility.

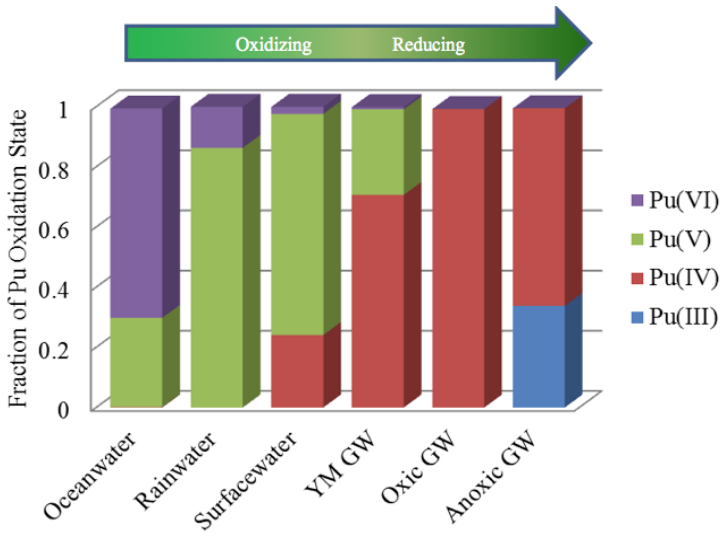

Fig. 1. This graph plots the simulated fraction of plutonium's oxidation state in various natural waters. The composition of the natural waters was taken from mean values reported by Silva and Nitsche. Modeling was performed using Geochemistry Workbench and the combined V8 R6 database at Lawrence Livermore National Laboratory.

expected to be very immobile in the environment as a result of the low solubility of PuO_2(s) and the strong affinity of Pu(IV) aqueous ions for mineral surfaces. Conversely, Pu(V) is expected to be mobile as a result of the dominance of the PuO_2 + dioxycation in aqueous systems. Such systems exhibit low complexation affinity and sorption affinity. Historically, it has been assumed that the following limit plutonium's environmental mobility: thermodynamic favorability, low solubility, and high-sorption affinities of Pu(IV). Further, this thermodynamic favorability of Pu(IV) has led to an observed dominance of Pu(IV) in environmental systems. This assumption has been challenged by those who have observed far-field, kilometer-scale subsurface transport of plutonium [Cleveland and Rees, 1981; Kersting et al., 1999; Santschi et al., 2002; Novikov et al., 2006].

A compete discussion of these field observations and the associated conceptual models of plutonium reactive transport is beyond the scope of this article, so our primary focus is on the environmental implications of (1) plutonium oxidation-reduction reactions at solid-water interfaces and (2) intrinsic plutonium colloid formation in aqueous systems and at solid water interfaces.

Plutonium Oxidation/Reduction Reactions at Solid-Water Interfaces

Several studies have shown that minerals may facilitate surfacemediated reduction of Pu(V) to Pu(IV). While examining Pu(V) sorption to the ferric oxyhydroxide mineral goethite [α-FeOOH), early observations were made by Kenney-Kennicutt and Morse [1985] and Sanchez et al. [1985]. Confounding these facts is that stoichiometric goethite contains *no* ferrous iron, which is required for Pu(V) reduction by iron. However, sufficient trace-level ferrous iron could have been present to Fig. 1. This graph plots the simulated fraction of plutonium's oxidation state in various natural waters. The composition of the natural waters was taken from mean values reported by Silva and Nitsche. Modeling was performed using Geochemistry Workbench and the combined V8 R6 database at Lawrence Livermore National Laboratory. First/Second Quarters 2016 47 facilitate reduction of the ultratrace (10^{-14} M to 10^{-9} M) concentrations of plutonium used in these experiments. This idea is supported by a more recent determination of the Pu(V) reduction kinetics on ferric iron minerals, along with observations of very rapid Pu(V) reduction on mixed valence ferrous/ferric iron minerals such as magnetite [Powell et al., 2004; Powell et al., 2005; Romanchuk et al., 2011].

Recent studies have also observed Pu(V) reduction to Pu(IV) on minerals that are considered oxidizing or nonreactive [Powell et al., 2006; Hixon et al., 2013]. Duff et al. [1999] performed an initial analysis of Pu(V) sorption to a rancieite mineral phase [$(Ca, Mn)Mn_4O_9 \cdot 3H_2O$] and Keeney-Kennicutt and

Morse [1985] and Romanchuk et al., [2011] within a thin section of tuff. This experiment yielded oxidation to Pu(VI) over the course of six months. After an additional two years of aging, Pu(IV) was the dominant oxidation state on the sample [Powell et al., 2006]. These results indicate that Pu(V) was initially oxidized. Over time, however, Pu(IV) was the dominant oxidation state. Similar observations were made using a pure pyrolusite [MnO_2(s)] mineral to simulate the ranciete phase [Powell et al., 2006].

Observations of unexpected redox reactions have enabled researchers to develop multiple working hypotheses to describe the mechanism of Pu(V) reduction on mineral surfaces. Such hypotheses include the following:

- Reduction by Fe(II) or Mn(II) within the mineral [Sanchez et al., 1985; Powell et al., 2004; Powell et al., 2005].
- Reduction based on a thermodynamic favorability of Pu(IV) surface complexes, wherein the reduction potential of the Pu(V)/Pu(IV) surface complexes are sufficiently elevated to facilitate reduction via the oxidation of water and subsequent formation of hydrolyzed Pu(IV) surface complexes [Powell et al., 2005; Hixon et al., 2013].
- Self-reduction via reaction with byproducts of alpha radiolysis [Sanchez et al., 1985; Hixon et al., 2013].
- Disproportionation of Pu(V) as the concentration of plutonium at the solid-water interface increases via sorption [Keeney-Kennicutt and Morse, 1985; Sanchez et al., 1985; Romanchuk et al., 2011].

A broad range of ongoing work consists of determining the dominant reactions responsible for the observed Pu(V) reduction. Given the relative mobility of Pu(V), reduction to Pu(IV) will reduce plutonium's mobility in the environment. Thus, developing an accurate model of plutonium's environmental mobility necessitates that we quantify the oxidation and reduction rates and mechanisms.

As described above, plutonium's surface-mediated reduction has been used to evaluate plutonium migration in the vadose zone by using a series of field lysimeters at the Savannah River Site [Kaplan et al., 2004]. To accurately describe plutonium's transport, both the reduction of Pu(V) to Pu(IV) and the reoxidation of Pu(IV) were dynamically included in the model. The rate of Pu(V) reduction was five orders of magnitude faster than the rate of reoxidation, consistent with the dominance of Pu(IV) surface complexes in the above-discussed studies with pure mineral phases. The reoxidation of Pu(IV) was proposed to be caused by an influx of oxidizing rainwater passing through the system. This proposal is consistent with the simulations shown in Fig. 2, as well as general observations of Pu(V) dominance in natural waters. Examining and quantifying these dynamic redox processes is a fascinating topic of ongoing work, particularly with respect to quantifying slow but potentially significant plutonium (and other actinide) desorption processes [Keeney-Kennicutt and Morse, 1985; Orlandini et al., 1986; Penrose et al., 1987; Choppin and Kobashi, 1990].

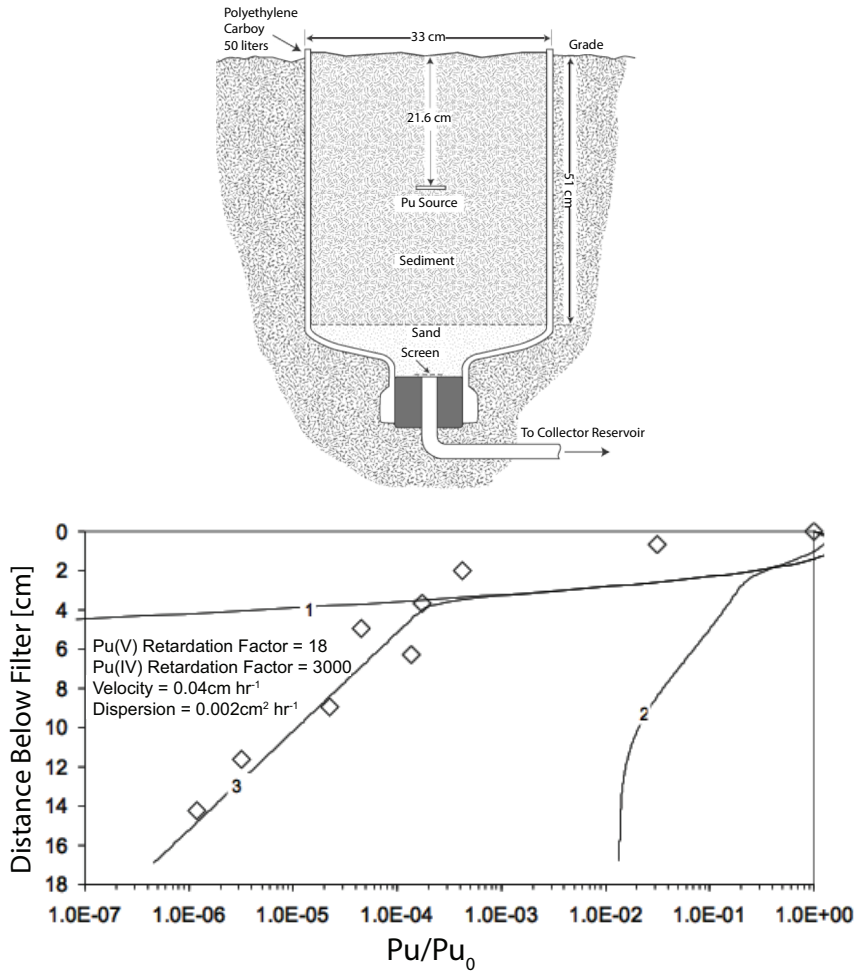

Fig. 2. This schematic shows field lysimeters used in plutonium vadose zone transport experiments (top) and plutonium soil concentrations below the source after 12 years of exposure (bottom). The solid line represents a reactive transport model fit to the data. Solid-line figures reprinted with the permission of Kaplan et al. (Copyright © 2004 by the American Chemical Society.)

Intrinsic Plutonium Nanocolloids in Aqueous Systems and Solid-Water Interfaces

As described previously, the observed dominance of Pu(IV) in environmental systems implies that plutonium essentially would be immobile in the subsurface. However, there has been a paradigm shift in our understanding of plutonium's mobility based on observations of colloidal transport at several field sites. For example, Kersting et al. [1999] observed kilometer-scale transport of plutonium at the Nevada Nuclear Security Site (NNSS). They also observed zeolites and clay mineral colloids within the same filtration size fraction as the plutonium. There was a similar observation of kilometer-scale transport of plutonium at the Mayak facility in Russia [Novikov et al., 2009]. In this case, plutonium was found primarily associated with iron oxide colloids. In both cases, plutonium is associated with an inorganic mineral colloid and generally referred to as a pseudocolloid. The term pseudocolloid can also be used to describe plutonium associated with organic colloidal particles, such as those observed at the Rocky Flats Environmental Technology Site [Santschi et al., 2002; Xu et al., 2008].

We use the term "pseudocolloid" to differentiate plutonium associated with natural colloids from "intrinsic" plutonium colloids, which result from Pu(IV) hydrolysis and condensation in aqueous solutions. Knope and Soderholm [2012] recently published an excellent review of the complicated series of reactions progressing through actinide hydrates, mononuclear hydrolysis products, and polynuclear complexes (likely oligomeric species that form intrinsic plutonium colloids). The large differences observed in plutonium solubility may be caused by the forming of intrinsic plutonium colloids and associated redox equilibrium between colloidal $PuO_2(s)$ and hyperstoichiometric PuO_{2+x} [Neck et al., 2007; Neck and Kim, 2001].

There are several ongoing efforts aimed at understanding the nature of intrinsic plutonium colloids to evaluate plutonium's fundamental solution chemistry, as well as to evaluate the potential environmental mobility of intrinsic plutonium colloids. In one effort, Powell et al. observed the formation of 2–5-nanometer-diameter intrinsic plutonium "nanocolloids" during the rapid neutralizing of a Pu(IV) solution. They used High-Resolution Transmission Electron Microscopy (Fig. 3) to confirm the expected Fm3m space group of the $PuO_2(s)$ structure. These nanocolloids were similar in both appearance and size to those previously observed [Haire et al., 1971] and to the $[Pu_{38}O_{56}Cl_{54}(H_2O)_8]^{14-}$ nanoclusters recently reported by Soderholm et al. [2008]. These results suggest that macroscale $PuO_2(s)$ may consist of an aggregated mass of crystalline, nano-sized plutonium clusters and/or colloids as opposed to a polymeric structure as previously reported [Neck et al., 2007; Rai and Swanson, 1981; Rai, 1982; Rai, 1984].

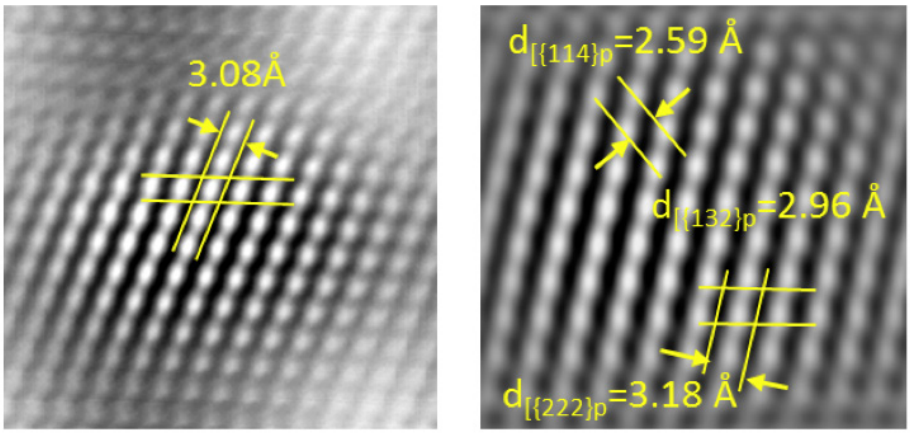

Fig. 3. This high-resolution Transmission electron micrograph image shows (left) an intrinsic plutonium nanocolloid and (right) an intrinsic plutonium nanocolloid associated with the iron oxyhydroxide mineral goethite. These figures are reprinted with the permission of Powell et al. (Copyright © 2004 by the American Chemical Society.)

The observation of intrinsic plutonium nanocolloids in aqueous solutions leads to the need to study the environmental mobility of these nanocolloids with the same approach used to study plutonium pseudocolloids. Possibly facilitating the formation of plutonium nanocolloids are (1) the circumneutral pH range of natural systems and (2) plutonium's relatively high concentrations in the source zones of contaminated sites. However, intrinsic plutonium colloids have an approximate point-of-zero charge of 8, implying that at circumneutral pH ranges the colloids will be significantly aggregated and thus are likely to be immobilized by aggregate deposition.

Such limited mobility was confirmed when researchers examined the transport of intrinsic plutonium nanocolloids through alluvium obtained from NNSS [Abdel-Fattah et al., 2013].

However, a significant fraction of plutonium was observed in the effluent when intrinsic plutonium colloids were equilibrated with smectite colloids and then passed through an alluvium column. Thus, it seems that plutonium intrinsic colloids are strongly associated with natural smectite colloids.

There were also similar observations made of a strong interaction between intrinsic plutonium colloids and goethite. According to these observations, an epitaxial distortion of the typical fluorite-type, face-centered-cubic PuO_2 to a body-centered cubic structure indicative of Pu_4O_7 of the Pu nanocolloids occurred on the goethite surface. This observation implies that there may be stronger binding of plutonium intrinsic colloids to goethite, as opposed to other minerals such as quartz [Powell et al., 2011] and hematite [Romanchuk et al., 2013] in which the epitaxial distortion was not observed. These studies imply that intrinsic plutonium colloids may strongly associate with mineral colloids to form a potentially mobile, hybrid pseudocolloid.

Analogous to the observations with monomeric Pu(IV), there are two conflicting conceptual models for subsurface transport of intrinsic plutonium colloids. Transport could be retarded if the plutonium colloids are associated with the subsurface rock or soil matrix. Moreover, transport could be enhanced if the plutonium colloids are associated with mobile mineral colloids. Additional studies could determine the molecular-scale behavior that controls plutonium's association with one phase over another.

Summary

Plutonium's geochemical behavior is governed by a complicated and coupled set of redox, hydrolysis, sorption, and precipitation reactions. As a result of controlled laboratory experiments with pure mineral phases and natural soils, we have developed conceptual models that help explain observations of plutonium's field-scale migration. However, we have not yet obtained a molecular-level understanding of the dominant processes controlling plutonium reactivity at solid-water interfaces, as well as the subsequent influences on plutonium migration. Significant knowledge gaps remain in our understanding of how plutonium transport in the environment is influenced by formation of plutonium intrinsic colloids, surface-mediated plutonium oxidation/reduction reactions, complexation with naturally occurring organic compounds, and interactions with microorganisms.

Publications Cited

Abdel-Fattah, A.I., et al., "Dispersion Stability and Electrokinetic Properties of Intrinsic Plutonium Colloids: Implications for Subsurface Transport," *Environmental Science & Technology*, 2013. **47**(11): 5626–5634.

Begg, J.D., M. Zavarin, and A.B. Kersting, "Plutonium Desorption from Mineral Surfaces at Environmental Concentrations of Hydrogen Peroxide," *Environmental Science & Technology*, 2014. **48**(11): 6201–6210.

Choppin, G.R., A.H. Bond, and P.M. Hromadka, “Redox speciation of plutonium,” *Journal of Radioanalytical and Nuclear Chemistry*, 1997. **219**(2): 203–210.

Choppin, G.R. and A. Kobashi, “Distribution of Pu(V) and Pu(Vi) in Seawater,” *Marine Chemistry*, 1990. **30**(1–3): 241–247.

Cleveland, J.M., *The Chemistry of Plutonium*. 1979, La Grange Park, IL: American Nuclear Society.

Cleveland, J.M. and T.F. Rees, “Characterization of Plutonium in Maxey Flats Radioactive Trench Leachates,” *Science*, 1981. **212**(4502): 1506–1509.

Duff, M.C., et al., “Mineral associations and average oxidation states of sorbed Pu on tuff,” *Environmental Science & Technology*, 1999. **33**(13): 2163–2169.

Haire, R.G., et al., “Aging of hydrous plutonium dioxide,” *Journal of Electron Microscopy*, 1971. **20**(1): 8–16.

Hixon, A.E., Y. Arai, and B.A. Powell, “Examination of the effect of alpha radiolysis on plutonium(V) sorption to quartz using multiple plutonium isotopes,” *Journal of Colloid and Interface Science*, 2013. **403**: 105–112.

Kaplan, D.I., et al., “Influence of oxidation states on plutonium mobility during long-term transport through an unsaturated subsurface environment,” *Environmental Science & Technology*, 2004. **38**(19): 5053–5058.

Keeney-Kennicutt, W.L. and J.W. Morse, “The redox chemistry of $Pu(V)O_2^+$ interaction with common mineral surfaces in dilute solutions and seawater,” *Geochimica et Cosmochimica Acta*, 1985. **49**(12): 2577–2588.

Kersting, A.B., “Plutonium Transport in the Environment,” *Inorganic Chemistry*, 2013. **52**(7): 3533–3546.

Kersting, A.B., et al., “Migration of plutonium in ground water at the Nevada Test Site,” *Nature*, 1999. **397**(6714): 56–59.

Knope, K.E. and L. Soderholm, “Solution and Solid-State Structural Chemistry of Actinide Hydrates and Their Hydrolysis and Condensation Products,” *Chemical Reviews*, 2012. **113**(2): 944–994.

Lu, N., et al., “Reversibility of sorption of plutonium-239 onto hematite and goethite colloids,” *Radiochimica Acta*, 1998. **83**(4): 167–173.

Lu, N., et al., “Sorption kinetics and impact of temperature, ionic strength and colloid concentration on the adsorption of plutonium-239 by inorganic colloids,” *Radiochimica Acta*, 2003. **91**: 713–720.

Maher, K., J.R. Bargar, and G.E. Brown, “Environmental Speciation of Actinides,” *Inorganic Chemistry*, 2012. **52**(7): 3510–3532.

Neck, V., et al., “Solubility and redox reactions of Pu(IV) hydrous oxide: Evidence for the formation of PuO_{2+x}(s, hyd),” *Radiochimica Acta*, 2007. **95**(4): 193–207.

Neck, V. and J.I. Kim, “Solubility and hydrolysis of tetravalent actinides,” *Radiochimica Acta*, 2001. **89**(1): 1–16.

Novikov, A.P., et al., “Evolution of actinide partitioning with colloidal matter collected at PA “Mayak” site as studied by sequential extraction,” *Journal of Radioanalytical and Nuclear Chemistry*, 2009. **280**(3): 629–634.

Novikov, A.P., et al., “Colloid transport of plutonium in the far-field of the Mayak Production Association, Russia,” *Science*, 2006. **314**(5799): 638–641.

NRC, *US Department of Energy's Environmental Management Science Program: Research Needs in Subsurface Science* 2000, National Academy of Sciences: Washington, DC.

Further Reading

A. B. Kersting, "Plutonium Transport in the Environment," *Inorg. Chem.* **52(7)**, 3533–3546 (2013).

H. Geckeis, J. Lützenkirchen, R. Polly, T. Rabung, and M. Scmidt, "Mineral–Water Interface Reactions of Actinides," *Chemical Reviews* **113(2)**, 1016–1062 (2013).

K. E. Knope and L. Soderholm, "Solution and Solid-State Structural Chemistry of Actinide Hydrates and Their Hydrolysis and Condensation Products," *Chemical Reviews* **113(2**), 944–994 (2013).

K. Maher, J. R. Bargar, and G. E. Brown, "Environmental Speciation of Actinides," *Inorganic Chemistry* **52(7)**, 3510–3532 (2012).

R. J. Silva and H. Nitsche, "Actinide Environmental Chemistry," *Radiochimica Acta* **70-1**, 377–396 (1995).

Actinide Nanoparticle Research, Springer-Verlag Berlin Heidelberg, 2011 (DOI 10.1007/978-3-642-11432-8_13).

Orlandini, K.A., W.R. Penrose, and D.M. Nelson, "Pu(V) as the Stable Form of Oxidized Plutonium in Natural-Waters," *Marine Chemistry*, 1986. **18**(1): 49–57.

Penrose, W.R., et al., "The Reduction of Plutonium(V) by Aquatic Sediments," *Journal of Environmental Radioactivity*, 1987. **5**(3): 169–184.

Powell, B.A., et al., "Stabilization of Plutonium Nano-Colloids by Epitaxial Distortion on Mineral Surfaces," *Environmental Science & Technology*, 2011. **45**(7): 2698–2703.

Powell, B.A., et al., "Plutonium oxidation and subsequent reduction by Mn(IV) minerals in Yucca Mountain tuff," *Environmental Science & Technology*, 2006. **40**(11): 3508–14.

Powell, B.A., et al., "$Pu(V)O_2^+$ adsorption and reduction by synthetic magnetite (Fe3O4)," *Environmental Science & Technology*, 2004. **38**(22): 6016–6024.

Powell, B.A., et al., "$Pu(V)O_2^+$ adsorption and reduction by synthetic hematite and goethite," *Environmental Science & Technology*, 2005. **39**(7): 2107–2114.

Rai, D. and J.L. Swanson, "Properties of Plutonium(Iv) Polymer of Environmental Importance," *Nuclear Technology*, 1981. **54**(1): 107–112.

Rai, D., "Crystallinity and Solubility of Pu(IV) Oxide and Hydrous Oxide in Aqed Aqueous Solutions," *Radiochimica Acta*, 1982. **30**: 213–216.

Rai, D., "Solubility Product of Pu(IV) hydrous Oxide and Equilibrium Constants of Pu(IV)/Pu(V), Pu(IV)/Pu(VI), and Pu(V)/Pu(VI) Couples," *Radiochimica Acta*, 1984. **35**: 97–106.

Romanchuk, A.Y., S.N. Kalmykov, and R.A. Aliev, "Plutonium sorption onto hematite colloids at femto- and nanomolar concentrations," *Radiochimica Acta*, 2011. **99**(3): 137–144.

Romanchuk, A.Y., et al., "Formation of crystalline $PuO_{2+x}{\cdot}nH_2O$ nanoparticles upon sorption of Pu(V,VI) onto hematite," *Geochimica et Cosmochimica Acta*, 2013. **121**: 29–40.

Sanchez, A.L., J.W. Murray, and T.H. Sibley, "The Adsorption of Plutonium-Iv and Plutonium-V on Goethite," *Geochimica et Cosmochimica Acta*, 1985. **49**(11): 2297–2307.

Santschi, P.H., K.A. Roberts, and L.D. Guo, "Organic mature of colloidal actinides transported in surface water environments," *Environmental Science & Technology*, 2002. **36**(17): 3711–3719.

Silva, R.J. and H. Nitsche, Actinide environmental chemistry. *Radiochimica Acta*, 1995. **70-1**: 377–396.

Soderholm, L., et al., "The structure of the plutonium oxide nanocluster $[Pu_{38}O_{56}Cl_{54}(H_2O)_{(8)}]^{14-}$," *Angewandte Chemie-International Edition*, 2008. **47**(2): 298–302.

Tinnacher, R.M., et al., "Kinetics of neptunium(V) sorption and desorption on goethite: An experimental and modeling study," *Geochimica Et Cosmochimica Acta*, 2011. **75**(21): 6584–6599.

Xu, C., et al., "Colloidal Cutin-Like SubstancesCross-Linked to Siderophore Decomposition Products Mobilizing Plutonium from Contaminated Soils," *Environmental Science & Technology*, 2008. **42**(22): 211–216.

Slow Magnetic Relaxation in a Plutonium-Based Molecular Complex

Nicola Magnani
European Commission
Joint Research Centre
Institute for Transuranium Elements
Actinide Research Unit
Karlsruhe, Germany

A common image associated with magnetism is the compass needle. This small piece of loadstone, when left free to rotate, aligns in the direction of the Earth's magnetic field; for centuries, such compasses helped countless navigators and explorers find their way.

Today, in addition to being ubiquitous on our refrigerators, magnetic materials play a critical role in various applications, from computer drives to techniques used for medical diagnostics. When kept well below its Curie temperature T_C, a good permanent magnet retains a large part of its magnetization for a long period of time, even if the external field is removed completely (Fig. 1). Such magnets can produce a stable magnetic field in a given volume of space without the need to continuously supply electrical or chemical energy.

In bulk materials, the exchange interaction keeps mutually aligned the magnetic moments of each ion. However, a significant obstacle to miniaturizing such devices is the onset of superparamagnetism. When the particle size becomes mesoscopic, the magnetization can be flipped randomly by thermal disorder, even below T_C.

In 1993, Sessoli et al. reported the first example of magnetic bistability of molecular origin in a manganese-based cluster. The measured hysteresis cycle for this Mn_{12} complex (Fig. 1, bottom-right corner) below the spin-blocking temperature T_B has essentially the same features as a permanent magnet below T_C. In this case, however, the slow relaxation of the magnetization has a purely intramolecular origin—it does not rely on any interaction between different clusters. Thus, the same hysteresis cycle is measured when the complex is diluted in a nonmagnetic matrix.

For the last 20 years, researchers have reported on a large number of molecular magnets based on transition metals, rare earths, and the actinide elements uranium and neptunium. Our work has expanded this range of elements toward the frontier of the periodic table with our discovery of slow magnetic relaxation in a plutonium-based complex.

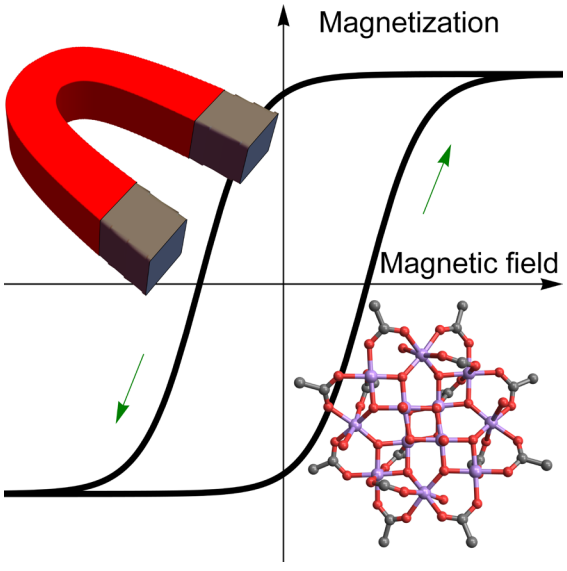

Fig. 1. This schematic shows a permanent magnet's hysteresis cycle below its Curie temperature. Once the magnetization is saturated, removing the external field does not bring it back to zero, but it does leave the sample in a metastable magnetized state (the intercept on the vertical axis is usually called remanence) with a very long lifetime. Magnetic bistability can give rise to a similar hysteresis cycle at a molecular level, as for example for the Mn_{12} cluster, depicted in the bottom-right corner. (Manganese ions are purple, oxygen is red, and carbon is gray. Hydrogen ions are not shown.)

Nicola Magnani describes the first plutonium-based single-molecule magnet ever reported.

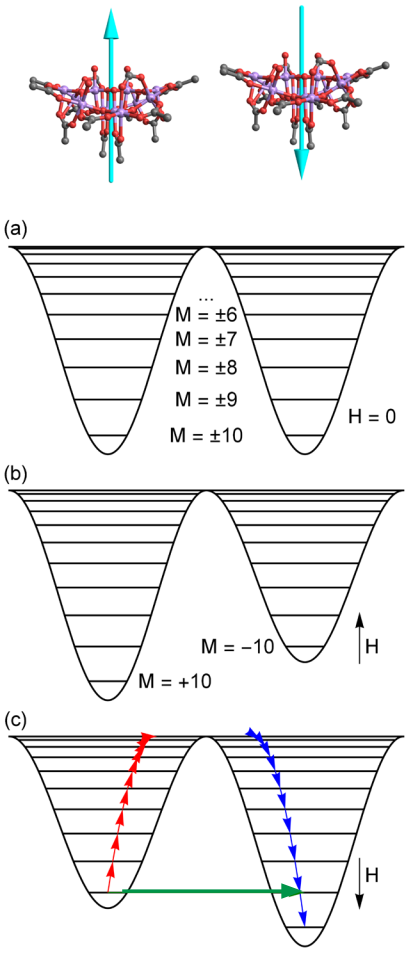

Fig. 2. This illustration shows the quantum energy levels of the Mn_{12} cluster in the "double well" model. The cyan arrows represent the orientation of the magnetization associated with the wells on each side. The panel shown in (a) has no magnetic field. The panel shown in (b) represents the situation for a magnetized cluster. The panel shown in (c) reverses the direction of the magnetic field. In this panel, the magnetization relaxes either through the absorption (red arrows) and emission (blue arrows) of several phonons or via quantum tunneling of the magnetization (green arrow).

How Does a Single-Molecule Magnet Work?

Exchange interaction is a quantum effect associated with the symmetry constraints imposed on a wavefunction upon swapping two indistinguishable particles. Such an interaction is essentially a magnetic coupling that tends to align the *spin* moments of interacting ions along the same direction. On the other hand, the *orbital* moments of a magnetic ion in a cluster preferably align along given directions determined by the crystal-field potential. This potential's symmetry reflects the local geometry of ligands around such ions.

In the case of Mn_{12}, eight trivalent manganese ions (each carrying a spin of S = 2) are coupled ferromagnetically to each other and antiferromagnetically to the other four tetravalent centers (S = 3/2), giving rise to a ground-state total spin of 10 for the whole molecule. Although inactive within the ground manifold, the spin-orbit interaction (which favors mutual alignment between the spin and the orbital moments) can still slightly mix it with excited states and is responsible for the easy-axis anisotropy that affects the magnetic moment.

A "double-well" energy spectrum [Fig. 2(a)] is obtained and the doublet with spin components $M = \pm 10$ along the easy anisotropy axis is selected as the ground state. Applying an external magnetic field breaks this last degeneracy, separating the two singlets so that one (assuming the one with $M = +10$) becomes lower in energy, as shown in Fig. 2(b). If the thermal energy is significantly lower than the splitting, the latter becomes the only populated level in the system and induces a large magnetization.

As shown in Fig. 2(c), reversing the external magnetic field causes this state to become metastable. In this case, the magnetization direction must also be reversed. In other words, the system must relax to the new ground state ($M = -10$). The main mechanism for this to happen is the spin-phonon interaction, whose Hamiltonian contains quadratic spin-operator terms so that only transitions with $\Delta M = \pm 1$ and ± 2 are allowed. Any such transition, which starts from a higher-energy to a lower-energy state (represented by blue arrows in Fig. 2), involves emitting one or more phonons that can occur directly. On the other hand, those from a lower- to a higher-energy state (red arrows) need phonon *absorption* to occur. Thus, the associated relaxation processes are thermally activated and can be effectively slowed down by lowering the temperature.

As indicated by the blue and red arrows in Fig. 2(c), a typical thermally activated relaxation process at temperature T occurs in time t according to an $m(0)exp(-t/\tau)$, with a characteristic time constant given by the Arrhenius equation $\tau = \tau_0 exp(U_{eff}/k_B T)$. In this framework, U_{eff} is defined as the *effective energy barrier*, in that it must be overcome to get from one side on the double well to the other. When the Hamiltonian that describes the double well also contains nonaxial terms, M no longer serves as a good quantum number and the eigenstates on both sides of the barrier display some amount of mixing. In this case, it is possible to initiate a direct transition from a state on one side of the barrier to one on the other, such as that indicated in Fig. 2(c) by the green arrow. Such a transition is typically referred to as

quantum tunneling of the magnetization (QTM). Because QTM transitions are not thermally activated, these "shortcuts" can compete with Arrhenius processes and ultimately result in faster relaxation at low temperatures.

A Plutonium-Based Single-Molecule Magnet

Because the spin-orbit coupling energy grows significantly with the atomic number, the anisotropy that acts against magnetization reversal is generally larger for lanthanides than for transition metals—and it is expected to be even larger for actinides. Despite this realization, the first actinide-based molecular magnet was only discovered in 2009. Since then, the number of new such complexes reported every year has been slowly but steadily increasing (Fig. 3), with the majority of them based on trivalent uranium. Nevertheless, it is highly desirable to extend work on transuranic samples to benefit fully from the rich chemistry and flexibility of actinides in the design of new molecular magnets. In this respect, the addition of plutonium to the picture is particularly interesting, given that this element can be stabilized in five oxidation states, each with a different electronic configuration and therefore potentially different magnetic properties.

The plutonium complex we studied was $Pu[\kappa^3\text{-N-HB(pyrazol-1-yl)}_3]_3$, in short $PuTp_3$. The isostructural uranium-based UTp_3 complex had already been identified as a single-molecule magnet, although with a relatively small effective barrier. The first coordination sphere of the actinide center is made by nine nitrogen atoms arranged in a tri-capped trigonal prismatic geometry.

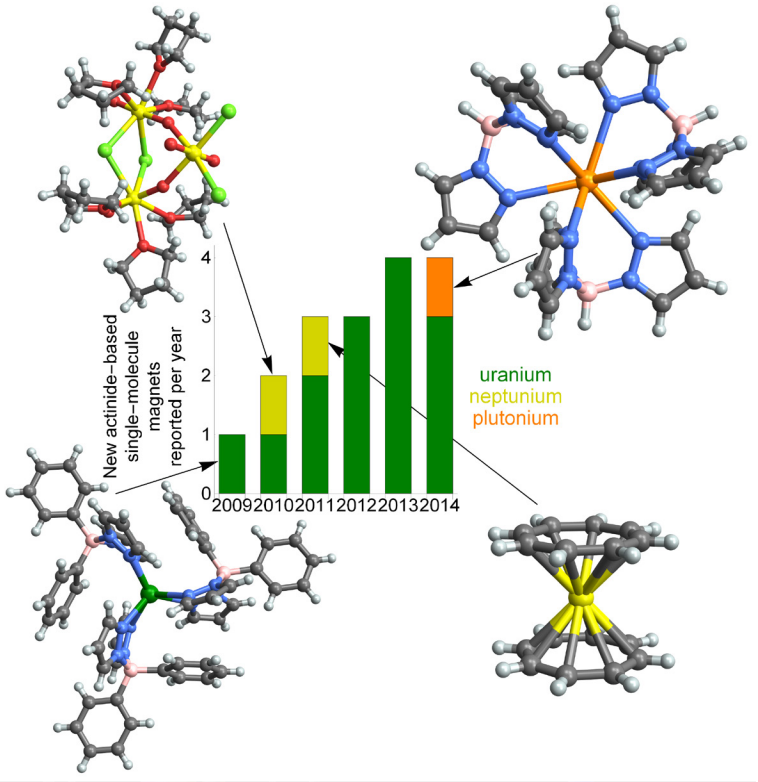

Fig. 3. This histogram shows the number of new actinide-based single-molecule magnets that have been reported yearly starting in 2009. Shown are the structures of some of these molecules, such as complexes for (bottom left) a uranium monometallic, (bottom right) neptunocene, (top left) a neptunium trimetallic, and (top right) the plutonium-based homoscorpionate discussed in the present work. The color scheme is as follows: dark green = uranium, yellow = neptunium, orange = plutonium, pink = boron, blue = nitrogen, light green = chlorine, red = oxygen, dark gray = carbon, and light gray = hydrogen.

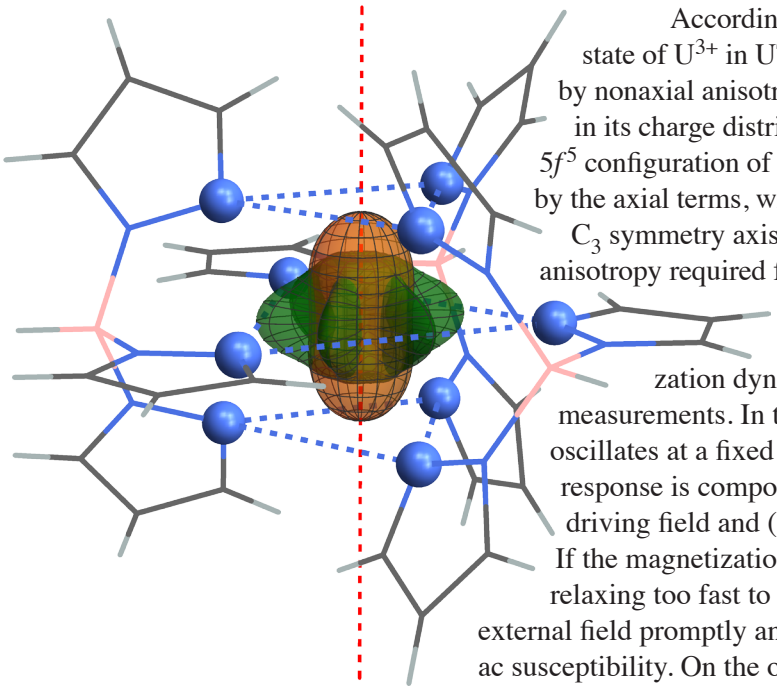

Fig. 4. This molecular model shows the calculated charge-density distribution relative to the electronic ground states of UTp_3 (green) and $PuTp_3$ (orange). The latter is elongated along the C_3 symmetry axis (indicated by a dashed red line and passing through the barycenters of the three triangles formed by the nine nitrogen atoms in the first coordination sphere, which are marked by dashed blue lines). The former shows the influence of nonaxial crystal-field energy terms. The scale used to plot the charge distribution on the actinide center is not related to the rest of the molecule, which is only sketched to depict the orientation of the reference frame.

According to crystal-field calculations, the electronic ground state of U^{3+} in UTp_3 within the $5f^3$ shell is very strongly influenced by nonaxial anisotropy terms, as can be seen by the lobes appearing in its charge distribution (Fig. 4). On the other hand, switching to the $5f^5$ configuration of Pu^{3+}, the ground state is almost entirely determined by the axial terms, with its charge distribution elongated along the C_3 symmetry axis. We expect this to result in the strong easy-axis anisotropy required for magnetic bistability.

A very informative way to determine magnetization dynamics is by using ac magnetic susceptibility measurements. In this technique, a small external magnetic field oscillates at a fixed frequency. The sample's dynamic magnetic response is composed of two different parts: one in-phase with this driving field and (2) the other out-of-phase.

If the magnetization of the magnetic complex under study is relaxing too fast to achieve bistability, the response is to follow the external field promptly and only measure the in-phase component of the ac susceptibility. On the other hand, the magnetization response in the presence of slow relaxation will be delayed with respect to the field variation, causing the development of an out-of-phase component. Figure 5 shows that $PuTp_3$ displays a significant increase of the out-of-phase susceptibility below 10 K, associated with slow magnetic relaxation. Analyzing the frequency dependence of these curves, the effective barrier was found to be $U_{eff} = 18.3\ cm^{-1}$, almost five times larger than for UTp_3.

Conclusion

Our ac susceptibility measurements proved that a marked slowing down of the magnetic relaxation of $PuTp_3$ occurs at low temperature, making it the first plutonium-based single-molecule magnet ever reported. We hope that this is a step forward in fully using the much-richer chemistry of actinides with respect to lanthanides in a synthesis-by-design approach. Furthermore, expanding the range of elements and electronic configurations that can support molecular magnetism is desirable to improve the theoretical modeling of their metastable states—which is particularly complicated for actinides because of the peculiar nature, between itinerancy and localization, of their $5f$ electronic shell.

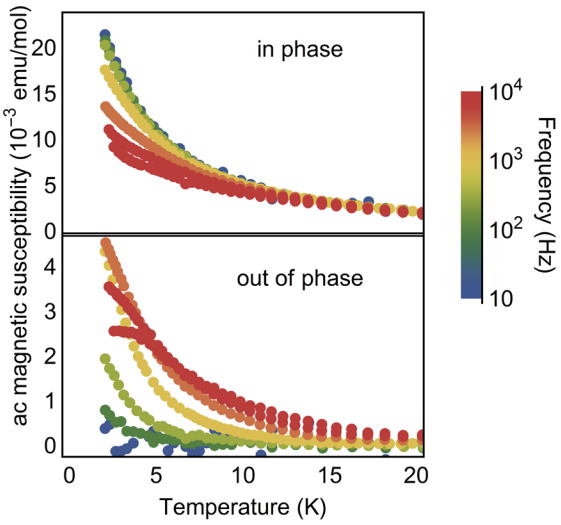

Fig. 5. This graph shows the in- and out-of-phase ac magnetic susceptibility measured for $PuTp_3$ as a function of temperature and frequency. The out-of-phase signal developing at low temperatures indicates that the magnetization dynamics are slowing down.

Atomistic Simulations

Surface Structure Peculiarities in Elemental Plutonium and Plutonium-Gallium Alloys

Vladimir V. Dremov, Gennady V. Ionov, and Alexey V. Karavaevm
Russian Federal Nuclear Center
Zababakhin All-Russia Research Institute of Technical Physics
Snezhinsk, Russia

Brandon W. Chung
Lawrence Livermore National Laboratory
Livermore, California

Vladimir Dremov discusses his work on Atomistic Simulations.

An extremely complicated phase diagram of plutonium comes about as a result of fine entropy effects linked with electronic excitations and lattice anharmonicity, as well as the fact that plutonium is on the edge between actinides with localized and delocalized 5*f* electrons. Elemental plutonium exhibits six polymorphous modifications at temperatures that range from 300 K to 950 K at ambient pressure. Thus, the energy difference between them is very small. Moreover, plutonium's phase stability may be strongly affected by small amounts of impurities, alloying additions, or radiation defects that influence the distribution of electronic density—in other words, any of these can affect the very layout of the plutonium phase diagram.

Indeed, it is well known that doping plutonium with small amounts of gallium stabilizes the high-temperature, face-centered cubic phase (δ-phase) of plutonium at ambient conditions. However, it is also known experimentally that a δ-phase plutonium-gallium alloy containing approximately 3 at.% gallium cooled down from ambient temperature partially transforms martensitically to the monoclinic alpha-prime structure starting at temperatures of approximately 150 K and below.

On the other hand, the redistribution of the electronic density may take place in the absence of any impurities or defects. In the vicinity of the surface, the local surroundings (or coordination number; i.e., the number of neighbor atoms) of atoms change, forcing the slight redistribution of electronic density. In the case of plutonium, such change may cause structural changes. Photoemission spectroscopy has provided experimental evidence for such changes. Photoemission spectra of α-Pu obtained at room temperature and above show that, as temperature increases, there is a smooth transition toward δ-Pu character (Fig. 1). One plausible explanation is that a δ-like reconstruction forms on the α-Pu surface. Hence, the following question arises: is the reconstruction an intrinsic property of plutonium or is it caused by impurities somehow accumulated on the surface of α-Pu?

We took into account various considerations when choosing tools for computer simulations designed to answer the question above. Despite the success of so-called *ab initio* electronic structure calculations (approach based on quantum theory of condensed state) and theoretical investigations into material properties based on them, such calculations and investigations still could not answer questions regarding the phase stability of actinides at finite temperatures, as well as the effect of low-concentration impurities on thermodynamic and mechanical properties.

Concurrently, Classical Molecular Dynamics (CMD) has proved an effective tool for modeling numerous phenomena in condensed matter. Because the number of particles in each CMD cell may reach several billions,

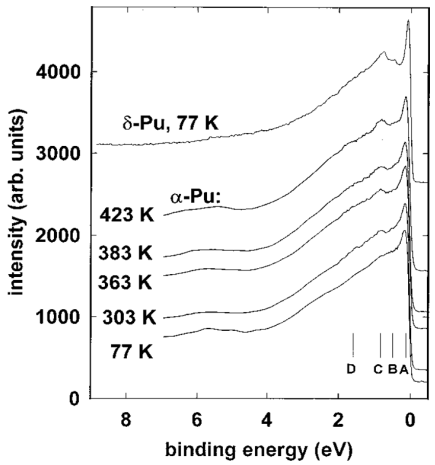

Fig. 1. These photoemission spectra show α-Pu and δ-Pu [L. Havela (2002)].

it then becomes possible to simulate directly, under specific conditions, phenomena such as plasticity and polymorphous transformations. Unlike the *ab initio* methods, CMD cells are quite large and thus can catch the nucleation of new structures whose symmetry differs from the initial. These cells can also track dislocation multiplication and mobility during straining.

Atomistic approaches to material investigation in the frame of CMD require that researchers develop sophisticated models of interatomic interaction. These models must provide high accuracy when simulating material properties and processes in them. Pair-wise, spherically symmetric potentials proved insufficient for describing material properties with low-symmetry crystal structures, thus giving way to sophisticated multi-body models.

To take into account the angular dependence of interatomic interaction in materials that have a complex electronic structure, Baskes et al. at Los Alamos National Laboratory developed the Modified Embedded Atom Method (MEAM). MEAM was successfully applied to the atomistic modeling of plutonium. The model in particular proved more than capable of reproducing the main features of plutonium-gallium alloys. Such features include martensitic transformation from high-symmetry δ-phase to low-symmetry structure, similar to alpha-prime, when the material is cooled down, and back when heated up.

Figure 2 shows thermal-cycling modeling. Samples of gallium-stabilized plutonium alloys initially having the fcc structure undergo a sudden density increase upon cooling, indicating a polymorphous transition into a low-temperature phase. Subsequent heating leads to a reverse transition, but at temperatures that exceed ambient. Thus, the so-called hysteresis loop is formed.

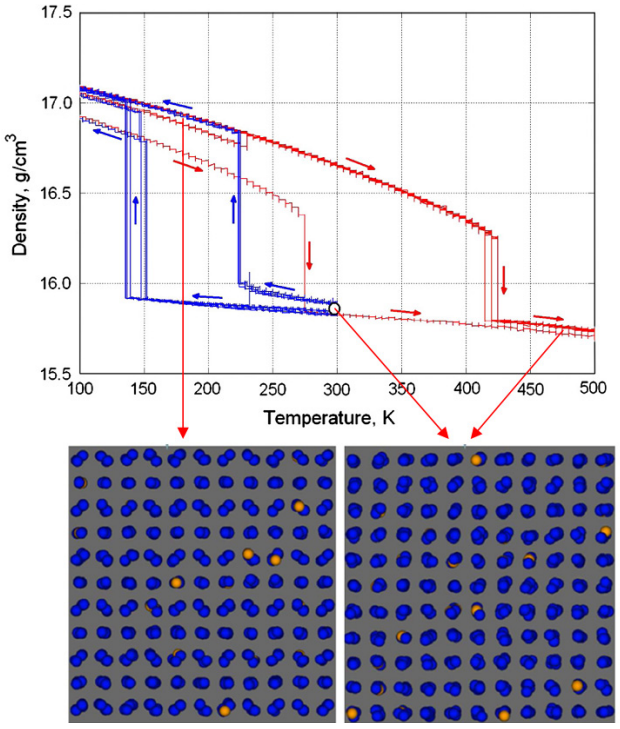

Fig. 2. This figure shows the thermal cycling of plutonium-gallium samples. In the upper plot, the blue lines are cooling trajectories and the red lines are heating trajectories. In the bottom plot, the left image shows a low-symmetry, low-temperature phase, whereas the right image shows a high-symmetry, fcc phase. Blue represents the plutonium atoms and yellow represents the gallium atoms.

When we take samples on the heating branch at temperatures less than the temperature of the reverse transition, we take samples having in the bulk a crystal structure that is different than the initial fcc. An examination of the surface of these samples gives us the following information. When looking at the atomic layers adjacent to the surface (Fig. 3), notice that just by sight the atomic arrangements are different from those in the bulk. A quantitative characteristic of the atomic arrangement—the average deviation of atoms from the perfect fcc position—shows that at the surface the atomic displacements are of the order of thermal vibrations relative to equilibrium fcc positions. That is, the structure corresponds mostly to the fcc, whereas in the bulk the average deviations are three times greater.

More convincing evidence of δ-like reconstruction on the surface comes by comparing virtual x-ray diffraction patterns (Fig. 4). An fcc pattern is noted at the surface of a low-temperature phase investigated at 120 K and 300 K. At the same time, the x-ray diffraction pattern calculated for the layers situated at a 1-nanometer depth from the surface shows a noticeable difference from the etalon fcc structure. That is, it belongs to a low-temperature phase that is of lower symmetry.

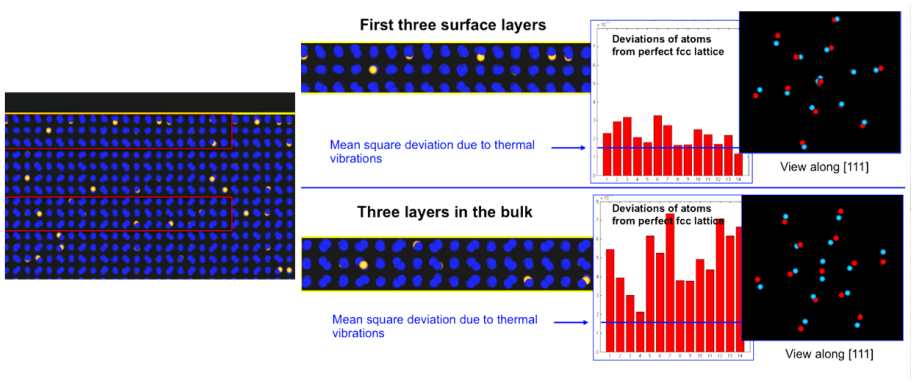

Fig. 3. This figure shows the structure of a plutonium-gallium sample in the vicinity of a free surface and in the bulk and deviations of atoms from the perfect fcc lattice nodes. The pictures on the right show the average positions of atoms. Red stands for a perfect fcc lattice and light blue stands for the sample under investigation.

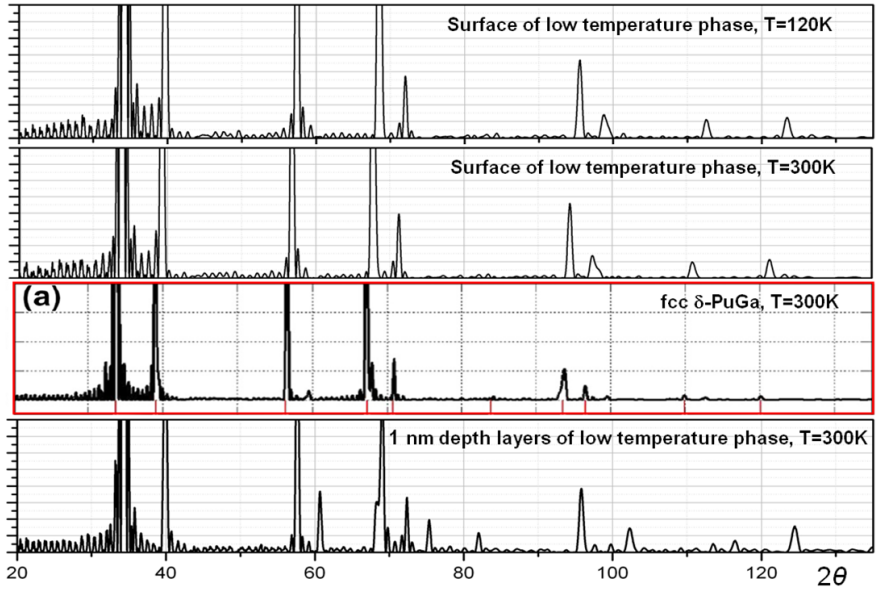

Fig. 4. These virtual (calculated) x-ray diffraction patterns are for a plutonium-gallium alloy. Red indicates the etalon pattern for the fcc structure.

The next step consists of investigating the properties of elemental plutonium. The fcc phase of elemental plutonium is not stable under ambient conditions. Nevertheless, the x-ray diffraction patterns of the surface layers were calculated at 300 K, demonstrating an almost perfect agreement with that of the etalon fcc structure (Fig. 5). However, when a sample of elemental plutonium is cooled to 200 K, the fcc structure of the surface layer decays, giving way to a transformation into the structure proper to the bulk of the low-temperature phase (compare bottom plots in Figs. 4 and 5).

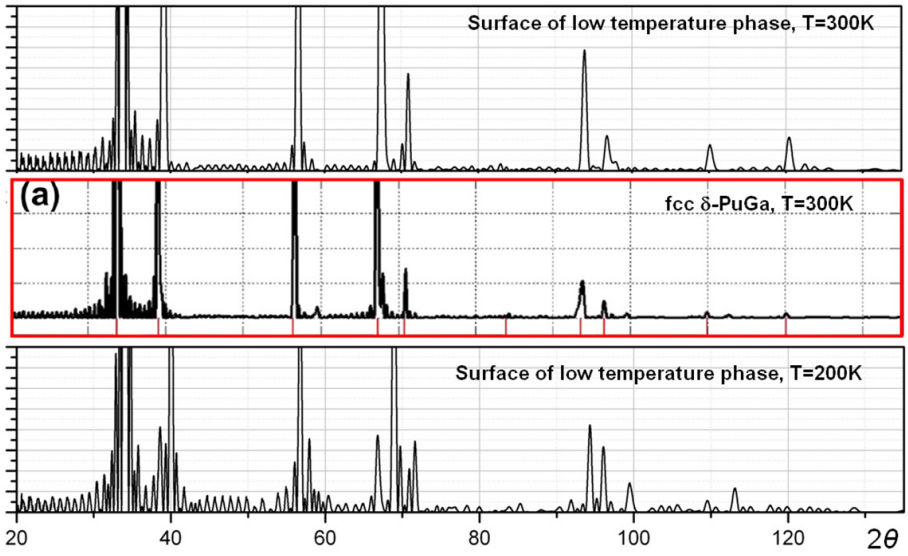

Fig. 5. These virtual (calculated) x-ray diffraction patterns are for elemental plutonium. Red indicates the etalon pattern for the fcc structure.

Thus, the CMD-MEAM simulations carried out to study the surface structure of (1) Pu-Ga alloy (3 at.% Ga) upon transition to the low-symmetry phase when cooling and (2) elemental plutonium have shown that, in the presence of gallium, the δ-reconstruction clearly takes place on the surface of the low-symmetry phase throughout the whole temperature range under consideration (120 K to 300 K).

For elemental material, the effect of δ-reconstruction clearly manifests itself at ambient temperature, although even at 200 K the effect is already strongly blurred. In all cases, when the δ-reconstruction was noticed, the depth of the reconstruction did not exceed 1 nanometer from the surface. Therefore, in the frame of current CMD-MEAM models, the δ-reconstruction on the surface is an intrinsic property of plutonium, with the effect enhanced by the presence of δ-stabilizing elements.

New Advances on Martensitic Transformation and Its Reversion

Benoit Oudot, Fanny Lalire, Brice Ravat, and Frances Dalaunay
CEA Valduc
21120 Is Sur Tille
France

Benoit Oudot explains new advances in martensitic transformation and its revision.

Nowhere is plutonium's uniquely complex character demonstrated more clearly than when it adopts as many as six different allotropic forms between room temperature and at its melting point of 640°C. Small perturbations in temperature and pressure dramatically change this material's physical properties.

One such example begins between room temperature and 112°C. At this temperature range, pure plutonium remains in its brittle phase—a simple, monoclinic structure. During its high-temperature δ-phase (its face-centered cubic, or fcc, structure), plutonium has the crystallographic symmetry and a 20% lower density that in its α-phase; it is stable between 310 and 452°C. Nevertheless, it is possible to retain this δ-phase in a metastable state under ambient conditions. Such retention is achieved through a low-percentage substitution of so-called "δ-phase-stabilizing" elements, such as aluminum, americium, cesium, and gallium.

The metastable δ-phase of Pu-Ga alloys with gallium content lower than 3 at.% can undergo a partial martensitic transformation when cooled from the fcc δ-phase to the monoclinic α'-phase. The latter is called α' rather than α because the α'-phase is supersaturated with gallium atoms trapped into the lattice—this has the effect of expanding the unit cell volume by approximately 1.8% relative to the pure α-phase, but it does not change the crystal structure.

The large volume change between the δ- and α'-phase distinguishes it from other martensitic transformations. However, there are some other notable characteristics in this transformation. Such unusual characteristics include a double C-curve kinetic in a time-temperature-transformation (TTT) diagram, as well as a large temperature span (150°C) of the thermal hysteresis from the transformation to reversion.

Upon heating, α'-phase gradually reverts back to δ-phase. Previous work indicated that such a reversion exhibits an unusual succession of sharp peaks in differential scanning calorimetry (DSC) scans that correspond to discrete, incremental steps in dilatometry. Such steps suggest autocatalytic burst martensitic events. It has been suggested that the burst-reversion process occurs because the 20% lower volume of the α'-phase generates significant matrix strains, which must be accommodated with plastic deformation. The reversion stops when the strain energy overcomes the driving force. Further transformation requires a higher temperature, which increases the driving force to initiate a new, reverted δ-phase.

Despite research performed on Pu-Ga martensitic transformation, many points remain poorly understood, such as the link between transformation and reversion mechanisms, kinetics, and martensitic morphologies. To improve our understanding of martensitic transformation, we performed a thorough study of the isothermal martensitic transformation kinetics at low temperature

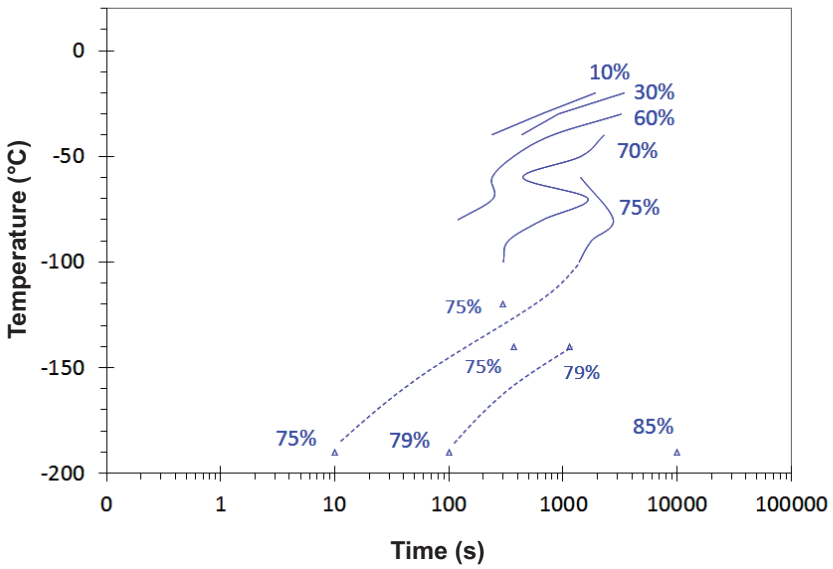

Fig. 1. This TTT diagram shows Pu-Ga 1 at.% (dotted lines are a guide for the eyes).

in Pu-Ga 1 at.% alloy. The originality of this work lies in a quantitative in situ characterization—combining XRD and linear dilatometry—of the martensitic transformation, in addition to performing a microstructures study for different transformation conditions.

We have also characterized a fully homogenized (1000 hours at 460°C) Pu-Ga 1 at.% alloy at isothermal temperatures. Although Ga is homogenized within the material, this composition does not exist at ambient temperature as fully δ-phase stable. In fact, we found that this alloy holds—at temperatures between –20°C and –196°C—an α'-phase amount. We determined this amount using Rietveld refinement of XRD diagrams. This method of phase quantization is subject to the caveat that x-rays penetrate only approximately 5 microns beneath the surface as a result of Pu absorption; surface layers of this Ga composition are prone to mechanically induced α'-phase from sample preparation. This kinetics study of the isothermal martensitic transformation in Pu-Ga 1 at.% without external stresses has confirmed that the TTT diagram (Fig. 1) exhibits a double C-curve similar to that found in prior experiments performed with higher-gallium-content alloys. An upper domain has been noticed between –20°C and –70°C, with a maximum in α'-phase amount at the end of the isothermal hold at –60°C.

This work has also highlighted different martensite morphologies for these two domains. At relatively high temperatures, we noticed a feather-like morphology associated with macroscopic strain of the sample (Fig. 2). At lower temperatures, we observed a very thin and parallel morphology involving no visible macroscopic strain (Fig. 3). These observations led us toward explaining the double C-curve occurrence by determining the influence of isothermal temperature on the accommodation mechanisms of the transformation strain.

Fig. 2. These images show a feather-like morphology obtained for the upper C.

Fig. 3. These images show thin and parallel morphology obtained for the lower C.

We propose that plasticity is active at relatively high temperatures (upper C-Curve), thereby enabling the accommodation of transformation strains by slip and leading to monovarient plates similar to lath martensite in steels. At lower temperatures, transformation strains are accommodated by (1) the formation of twinned plates, (2) self-accommodated plates, and (3) elasticity. Results indicate that controlling the transformation are a large autocatalytic effect and interaction occurrence (local stress field). In addition to the martensitic phase transformation at low temperature, we investigated within the elastic domain an external stress influence on martensitic transformation.

In situ XRD and dilatometry sample holders were developed to study transformation kinetics and microstructures under applied stresses. A comparison was then conducted between the martensitic starts temperature shifts induced by applied stress type and Patel and Cohen's theory of the thermodynamics of stress-affected martensitic transformation. This comparison produced some very good agreements. We then investigated the influence of an external uniaxial compression (100 MPa), beyond the strength yield, on the same alloy used 40 years ago by Goldberg et al., in which was observed the occurrence of new phases (γ and α) and a particular microstructure orientation in a Pu-Ga 1 at.%.

Using Rietveld refinement in our alloy exhibits the presence of a three-phase alloy at room temperature (δ, γ/γ', and α'), as previously observed by Faure et al. on another gallium-containing alloy. Moreover, optical metallography performed in a longitudinal

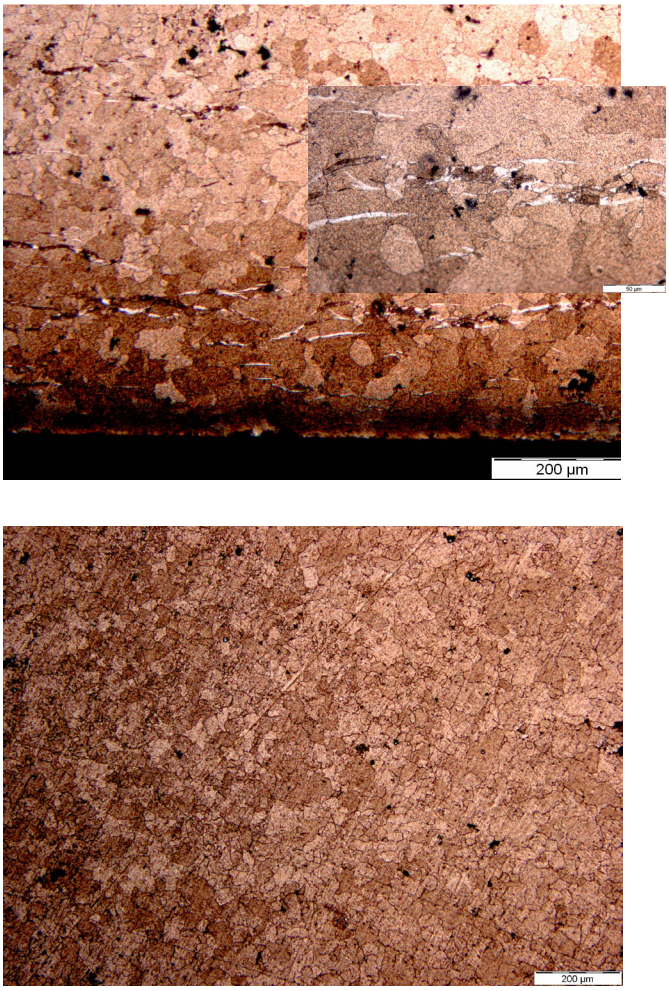

Fig. 4. These photos show a sample collected using optical metallography. Note the deformation under a uniaxial compression with a stress of 100 MPa. The top image is parallel to the compression axis, with the bottom image normal to the compression axis.

cross-section to the compression axis (Fig. 4) reveals some laths mainly aligned with their long axis normal to the stress direction. Note that the optical metallography performed normally to the compression axis does not reveal any lath. Such as difference indicates that the sample is morphologically oriented during the transformation under stress.

The other purpose of this work was to investigate the whole reversion process of a transformation induced by an applied stress to this fully homogenized Pu-Ga 1 at.% alloy. With respect to martensitic reverse transformation, our previous work reveals that the reverse transformation of the two-phase (γ-α) alloy during heating involves two competing modes, namely, direct and indirect reversion. Indirect reversion is associated with a gallium diffusion process that governs the ratio between these reversion modes.

This study suggests that the indirect reversion process consists of a diffusive process in which gallium enriches local regions of δ-phase, with adjoining local regions of β- and γ-phase of pure plutonium. Researchers have used CALPHAD-based simulations to investigate in detail the mechanisms of reverse transformation in such alloys.

The theoretical investigation of this system plays an especially important role because of the inherent difficulties in its experimental study. Such an investigation enables us to focus on the thermodynamic and kinetic aspects of the competition between direct reversion $\alpha' \rightarrow \delta$ and indirect reversion $\alpha' \rightarrow \beta+\delta_{enriched}$ (first step of indirect mode). Thermodynamic simulations indicate that both reversion modes were possible, with indirect reversion having the strongest driving force. Finally, the ratio of direct to indirect reversion depends on three factors: heating rate, initial α' phase fraction, and gallium content.

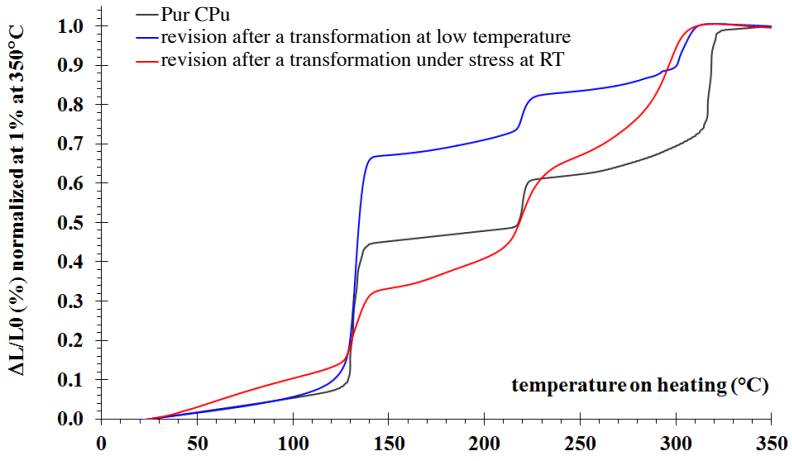

Fig. 5. This graph plots length variation vs. temperature normalized at 350°C for three different reverted samples. The black curve (pure plutonium) is used as a reference. The blue curve (reverse of an α'-phase formed at low temperature) shows the mixture of the direct (α'/δ) and indirect (α'/β) reversion process with a higher first abrupt length change (120°C/140°C) than for pure plutonium. The red curve represents the normalized length variation measure during heating after a uniaxial compression at room temperature.

All simulations were confirmed experimentally, highlighting key aspects of reversion mechanisms. The absence of burst mode on the temperature derivative of the dilatometry curve, or $d(\Delta L/L_0)/dT$, also shows the influence of the gallium content. That is, the lower the gallium content, the higher the reversion temperature. As the reversion temperature increases, it lowers the lattice stress from the direct reversion process. However, it also promotes the indirect reversion process thus limiting the strain by a lower volume variation (α'/β relative to α'/δ). We used dilatometry and XRD to study reverse transformation after the 100 MPa uniaxial compression. Figure 5 shows the length variation $\Delta L/L_0$ as a function of temperature for three different samples.

The reversion of α' phase formed at low temperature occurs as a mixture of a direct

(α'/δ) and an indirect (α'/β) reversion process with a higher first abrupt length change (120°C/140°C) than for pure plutonium. After a uniaxial compression, this time the first length change is smaller than that for pure plutonium. Indeed, it is very small, facing the third length change (T > 250°C) that corresponds to the γ/δ reversion that results from the specific orientation. It is then interesting to note that a good Rietveld refinement on XRD data is only possible after taking into account preferred orientations for γ/γ' and α'-phases, thus confirming macroscopic observations.

The close-packed lattice planes of the γ/γ' and α'-phases that resulted from applied stress were found in general to have turned perpendicular to the compression direction. The amount of the different phases was estimated (Fig. 6); such phases remain stable during heating between room temperature and 120°C. At such a temperature domain, there are at least two times more γ/γ' than α'-phases. According to previous dilatometry measurements and XRD data, the temperature range from 130°C up to 200°C corresponds to the δ+β/ β' phase region, with no more observed γ/γ' and α' phases. Nevertheless, the β/β'-phase reverts reverts to γ/γ'-phase at 220°C. Finally, for a temperature higher than 250°C the γ/γ'-phase gradually reverts to the δ-phase. The γ-phase lattice parameter was then measured (Fig. 7) to study the possibility of a reversion process occurring with gallium diffusion in a way similar to that observed after a transformation at low temperature.

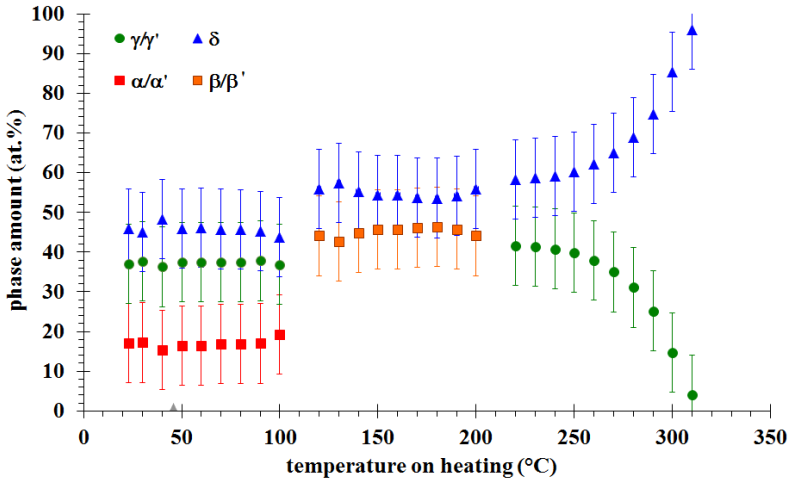

Fig. 6. This graph plots the amount of the different phases estimated (from XRD data) vs. temperature.

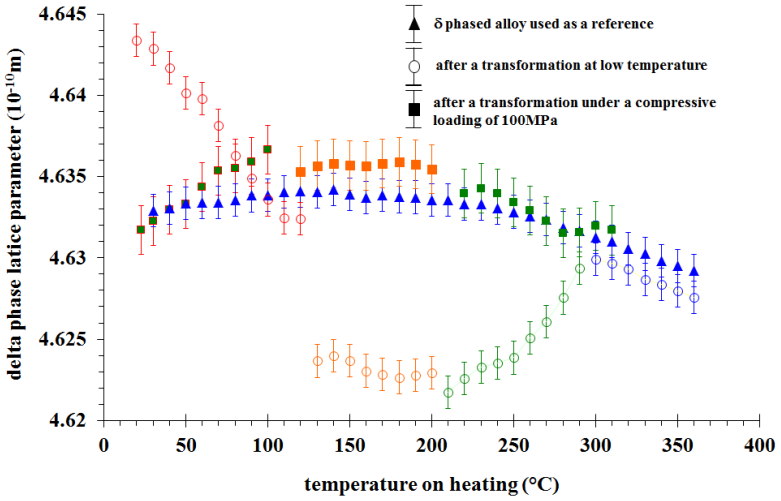

Fig. 7. This graph plots δ-phase lattice parameter vs. temperature for three different samples. The blue triangles depict the single δ-phased alloy behavior that results from δ-phase restoration at high temperature (used as a reference). Rings represent the δ-phase lattice parameter evolution during the course of the reversion process after a transformation at low temperature. Solid squares stand for the δ-phase lattice parameter after a transformation under a compressive loading of 100 MPa.

Previously associated with the first decrease of the δ-phase lattice parameter was the progressive annealing of the strain induced by the presence of α'-phase formed at low temperature. This first decrease is not observed after a transformation under stress. However, in such a case, the α'-phase amount formed is much lower than those formed under lower temperature. Moreover, the γ/γ' formed with α'-phase under stress leads to a better accommodation with a few oriented morphologies and thus induces much less stress in the δ phase. In addition to various phase orientations, the relative changes in bulk volume are determined by the bulk modulus of the phases present [F. J. Freibert, *IOP Conf. Series: Materials Science and Engineering* **9** (2010), 012096].

However, the most interesting difference between the two reversion paths is the δ-phase lattice parameter behavior on the β/ β'-phase domain. Indeed, the δ-phase lattice parameter collapsed after 120°C (temperature of the α'- to β-phase transformation) for a reversion process, following a transformation at low temperature that was previously associated with a pure γ-phase.

The redistribution of the gallium occurred as a result of the transformation of the pure γ- to δ-phase alloy, as illustrated by the progressive δ-phase lattice parameter increase in the γ-phase domain (210°C to 300°C). Such behavior is not observed on the reversion process after a transformation under stress. The question of gallium's location remains unanswered, even if a diffusional process is at work as a reversion path after such transformation. Note that the lath morphology is definitively different, even if the amount of β-phase formed during the reversion process after a transformation at low temperature or under stress is quite the same.

Under stress, the lath shape is more lenticular. At low temperature, the lath shape is more feather-like or has thin parallel morphologies. At the origin of these different behaviors is that the interface surfaces of contact and accommodation process differences for both reversion modes. Thermodynamic calculations may help us to better understand these differences, and thus more experimental data are necessary. However, these results definitively highlighted the true complexity of the martensitic transformation and its reversion. Such complexity is a result of the competition between thermodynamics and mechanics in driving the transformation path.

Sonochemistry of Actinides

Matthieu Virot, Tony Chave, Vincent Morosini, Rachel Pflieger, and Sergey I. Nikitenko
ICSM-UMR5257 CNRS/CEA/UM/ENCSM
Site de Marcoule, France

Laurent Venault and Philippe Moisy
CEA/DEN/MAR/DRCP
Nuclear Energy Division Radiochemistry and Process Department
France

Introduction

Scientists have long known that hydrogen gas and hydrogen peroxide are formed when high-power ultrasound is applied to water or aqueous solutions. This early research served to establish what was then a new field of chemistry known as "sonochemistry."

In general, ultrasound spans frequencies of roughly 15 kHz to 1 GHz. However, sonochemical effects are observed only in the range of 15 kHz to 2 MHz. Higher frequency ultrasound is used principally for medical and material diagnostics. The acoustic wavelengths of chemically active ultrasound ($1–10^{-4}$ cm) are much larger than the size of a molecule. Therefore, sonochemistry does not arise from a direct action of ultrasonic waves on molecules but rather from acoustic cavitation. Simply put, cavitation is a set of consecutive events: nucleation, growth, and implosive collapse of microbubbles of a size resonant in the applied cavitation field. Scientists generally agree that the chemical and physical effects of ultrasound are related to the extremely rapid implosion of cavitation bubbles.

We must emphasize that acoustic cavitation leads not only to the chemical transformation of the medium but also to light emission known as sonoluminescence. Recent spectroscopic studies of sonoluminescence discovered the formation of a nonequilibrium plasma inside the collapsing bubble. The photons and "hot" particles produced by the sonochemical plasma may excite nonvolatile species in solutions, thus increasing their chemical reactivity.

In principle, each cavitation bubble serves as a plasma chemical microreactor that provides highly energetic processes to the bulk solution at almost room temperature. In heterogeneous systems, the mechanical forces generated by cavitation—rather than the chemical effects—could play a much more important role. At the vicinity of a solid boundary, the bubble collapse becomes asymmetric and leads to several specific phenomena, such as acceleration of mass transfer, surface erosion, and grain-size reduction. Today, using power ultrasound to enhance the reactivity of solids has become a routine technique in a large set of processes.

Over the past few years, the sonochemistry group at the Institute for Separation Chemistry in Marcoule (ICSM) has performed research dedicated to the fundamental understanding of actinide and lanthanide chemistry under ultrasound irradiation. The first sonochemical reactions of actinides in aqueous solutions were reported more than 20 years ago. In most cases, there is no direct action of cavitation bubbles on the actinide species. Instead, ultrasonic irradiation causes a chemical transformation of the liquid medium, followed by redox interactions of the sonolytic products with actinide ions. For example, sonolysis of nitric acid solutions yields as principal products nitrous acid, HNO_2 in the liquid phase and NO_x in the gas phase.

Matthieu Virot discusses the most recent measurements of sonoluminescence of uranium and redox reactions of plutonium during acoustic cavitation.

Unlike in pure water, H_2O_2 formation is not observed in nitric acid solutions because of its rapid scavenging with HNO_2. In nuclear chemistry, nitrous acid is known as a key reagent that determines the redox kinetics of actinides in nitric acid solutions. Therefore, ultrasonic treatment seems suitable in controlling the actinide oxidation states without having to add any chemicals. This report summarizes the most recent measurements of sonoluminescence of uranium and redox reactions of plutonium during acoustic cavitation. This work results from a strong collaboration between the ICSM/LSFC and the DEN/DRCP departments of Marcoule Research Centre.

Fundamental Sonochemistry of f-Elements: Sonoluminescence of Uranyl Ion

Excited uranyl ions are known for their green fluorescence. Such ions have been used for more than 150 years for dyeing glass and performing analyses. Because they are strong oxidants [$E_\circ$ = 2.6 V vs. NHE (normal hydrogen electrode)], they are of particular interest for use in radioactive waste management, as they can oxidize organic substrates in radioactive liquid wastes. The redox properties of these ions can also be used to develop advanced actinide separation processes.

New approaches to excite uranyl ions are of particular interest today. So far, excitation pathways of uranyl ions involve UV/Vis light and radiolysis of liquid or solid systems containing uranium. Ultrasound presents similarities with both methods. Indeed, a plasma is formed during the violent collapse of cavitation bubbles. First, it emits light (sonoluminescence) that spans from the UV to the NIR, possibly photoexciting the uranyl ions. And second, formed in the bubbles are hot particles, which may excite species in solutions by collisions at the bubble-solution interface. The excitation of uranyl ions under the effect of 20-, 203-, and 607-kHz ultrasound was investigated experimentally in acidic solutions of $HClO_4$ and H_3PO_4. Interestingly, although in $HClO_4$ solutions uranyl ions exhibit extremely weak sonoluminescence, their emission in H_3PO_4 is extremely bright—it is even visible to the naked eye (Fig. 1).

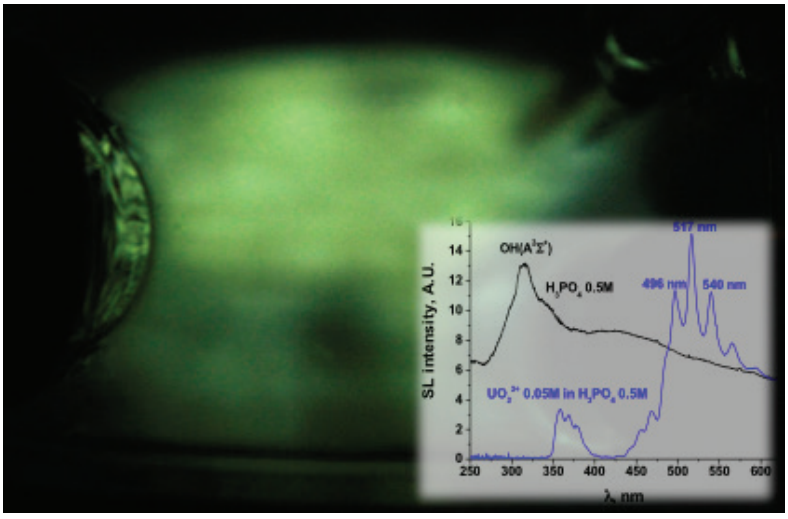

Fig. 1. This photo shows the sonoluminescence of a solution of 0.05 M UO_2^{2+} in 0.5 M H_3PO_4, sonicated at 203 kHz (35 W, 10°C) under argon flow. The inset shows the corresponding sonoluminescence spectra (blue) with that of the pure acid (black).

A first explanation of this difference is the existence of a strong quenching of UO_2^{2+}* by water molecules, either by vibrational coupling or by the abstraction of a hydrogen atom from a water molecule coordinated to uranium:

$$(UO_2^{2+})^* + H_2O \rightarrow UO_2^{+} + H^+ + OH^\bullet$$

In H_3PO_4, uranyl ions are protected by complexation. Also, an additional source of quenching was observed, one that is ultrasound-specific: quenching by sonolytical products

(H_2, H_2O_2), whose formation rates also decrease in the presence of uranyl ions. The suggested mechanism is the following:

$$(UO_2^{2+})^* + H_2 \rightarrow UO_2^{+} + H^+ + H$$
$$(UO_2^{2+})^* + H \rightarrow UO_2^{+} + H^+$$
$$(UO_2^{2+})^* + H_2O_2 \rightarrow UO_2^{+} + H^+ + HO_2^{\bullet}$$
$$UO_2^{+} + OH^{\bullet}\ (HO_2^{\bullet}, H_2O_2) \rightarrow UO_2^{2+}$$

After observing uranyl's bright sonoluminescence in H_3PO_4, we investigated its mechanism of excitation by varying the concentration of UO_2^{2+}. If the mechanism is photoexcitation, we expected that the intensity of uranyl luminescence should vary linearly with its concentration. On the other hand, we expected in the collisional excitation mechanism that uranyl's reciprocal light emission would vary linearly with the reciprocal UO_2^{2+} concentration. Our experiments show that sonophotoluminescence dominates in diluted solutions, and that collisional excitation adds its contribution at higher UO_2^{2+} concentrations ($[UO_2^{2+}] > 0.035$ M).

Sonochemistry in Homogeneous Media: Redox Behavior of Plutonium Ions

The sonochemical adjustment of the actinide oxidation states in solution may represent an original and interesting alternative to conventional processing methods. Accurate tuning of parameters enables the sonication of aqueous solutions to generate in situ redox species with controlled kinetics—without having to add salt or a concentrated reagent to the solution. Oxidant or reducing species therefore may be generated as a function of solution chemistry.

Figure 2 illustrates one of the sonochemical setups in a glovebox available at Atalante facility in Marcoule. It is in such a reactor that there have been studies about the sonochemical behavior of plutonium ions in aqueous nitric solutions. In a 1 M nitric medium, we observed the rapid and catalytic oxidation of Pu(III) to Pu(IV) (followed by absorption spectroscopy, respectively, at 602 and 476 nm). Such oxidation is attributed to nitrous acid generation as a result of nitric acid sonolysis.

Very stable in sonicated 1 M nitric acid, Pu(IV) can be reduced to Pu(III) in the presence of 0.1 M antinitrous reagents (Fig. 3). The reduction

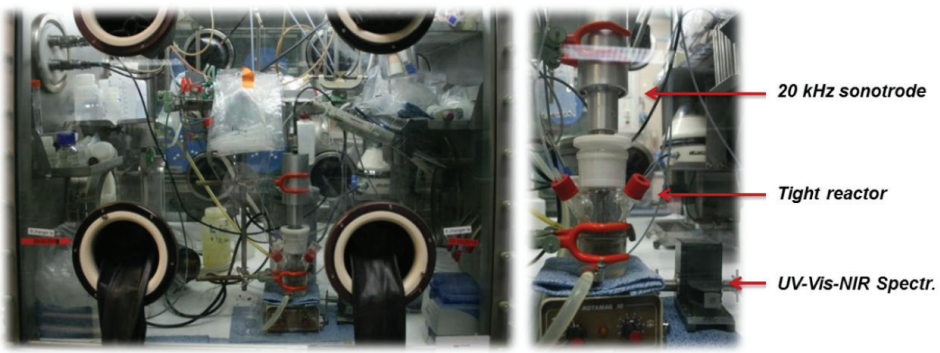

Fig. 2. This experimental setup was used to perform 20 kHz sonochemical experiments at the Atalante facility in Marcoule. This system consists of a tight reactor that can control temperature, a circulator of carrier gases, and even the sampling of solution during sonolyses. The cell is cooled from outside the box and an UV-Vis-NIR spectrophotometer is also connected to the enclosure.

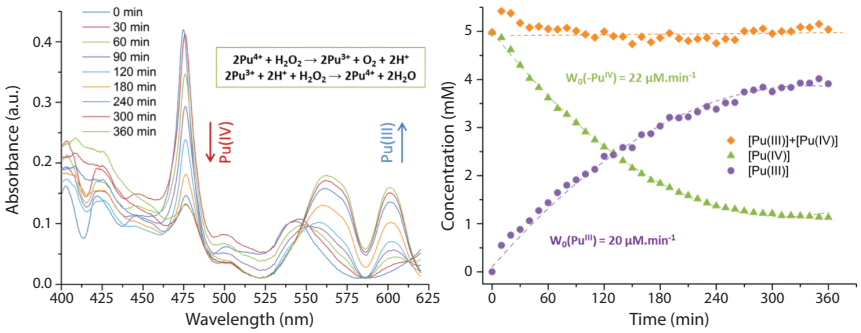

Fig. 3. The image on the left shows UV-Vis absorption spectra measured during the sonication of a Pu(IV) solution in 1 M HNO_3 – 0.1 M NH_2SO_3H. The image on the right shows plotted concentrations measured for Pu(IV) and Pu(III) in similar conditions (at 476 and 602 nm, respectively). The left figure's insert shows the overall chemical reactions that occur under sonication. These reactions agree with the literature with respect to corresponding experiments without ultrasound.

process follows a first-order reaction law whatever the reactant: with $k' = 5.7 \times 10^{-3}$ min^{-1} in the presence of sulfamic acid (at 0.45 $W.mL^{-1}$), with $k' = 7.5 \times 10^{-3}$ min^{-1} in the case of hydrazinium nitrate (at 0.52 $W.mL^{-1}$). The slight reported difference on the apparent rate constants results from the additional reducing property of hydrazinium nitrate towards Pu(IV). Note also that the Pu(IV) reduction rate increases with applied acoustic pressure and that the reduction process is uncompleted—it remains a steady state in which Pu(III) and Pu(IV) exhibit constant concentrations for extended sonolyses (Fig. 3).

Furthermore, no additional redox states of plutonium are observed in solution during Pu(IV) sonolysis under these conditions. The absence of H_2O_2 in solution during sonication suggests its contribution in the reduction process that agrees with plutonium's classical solution chemistry. By sonicating a Pu(III) solution in 1 M HNO_3 – 0.1 M $[N_2H_5][NO_3]$, we noticed the accumulation of Pu(IV) in solution. We therefore attributed the observed steady state (for extended sonolyses) to the partial back oxidation of Pu(III) with sonochemically generated H_2O_2. Indeed, H_2O_2 can be considered as both an oxidizing (1.77 V vs. NHE for H_2O_2/H_2O couple) and a reducing agent (0.68 V vs. NHE for O_2/H_2O_2 couple).

These overall redox processes agree with what has been observed in the literature without ultrasound (Fig. 3). Note that reducing Pu(IV) is supposed to occur by forming soluble peroxo complexes that decompose in acidic media to form Pu(III). However, these complexes were not observed in our experimental conditions, possibly because of their low amount and instantaneous decomposition.

This study demonstrates that the in situ generation of reactive species provided by high-power ultrasound may help stabilize actinide redox states without adding chemicals during the process. Although observed with low rates, the considered kinetics may be optimized with appropriate settings for frequencies, concentration of solutes, gaseous atmosphere, presence of catalysts, etc.

Sonochemistry in Heterogeneous Systems: Sonochemical Preparation of Plutonium Intrinsic Colloids

Fundamentally understanding colloid formation and its characterization today play a critical role in actinide chemistry because of environmental concerns related to contamination, waste disposal, and migration in the environment. Industrial separation processes (e.g., PUREX) also generate actinide colloids during equipment cleaning. Beneficial to such companies would be a predictive model that describes colloid behavior, formation, and subsequent separation.

Pu(IV) is particularly prone to hydrolysis (even under very acidic conditions), which further leads to intermolecular condensation reactions and the formation of multinuclear metal oligomers. We showed that the extended sonication of PuO_2 (180 mg, calcinated at 600°C, S_{BET}= ~10 $m^2 \bullet g^{-1}$) under argon atmosphere in pure water leads (after centrifugation to remove large PuO_2 particles) to the formation of intrinsic colloids that are stable for several months.

We compared these colloids to classical hydrolytic colloids obtained by diluting in pure water a known concentration of Pu(IV) initially stored in nitric acid. Besides the different green color tones (Fig. 4), the resulting Vis-NIR absorption spectra indicate that both colloids show some structural similarities but also some significant differences, including a strong Mie scattering for the sonolytic colloid resulting possibly from the presence of larger aggregates. Among the various oxides studied in our lab (CeO_2, ThO_2, etc.), PuO_2 is the only material having such a behavior under acoustic cavitation.

Although sonication in heterogeneous systems is known to increase erosion of surfaces and fracturing of grains, complementary experiments performed with ThO_2 emphasized that the mechanical action resulting from acoustic cavitation is not responsible for forming plutonium colloids. Therefore, we considered chemical reactions driven by acoustic cavitation, and we were surprised to observe that plutonium colloid formation depends strongly upon the gaseous atmosphere during sonication. In the presence of Ar/O_2 (80/20, v/v), plutonium colloids are not observed, whereas an increased rate of formation is observed under Ar/CO (90/10, v/v). Previous investigations showed that this phenomenon results from the ability of these gases to favor the generation of either H_2 or H_2O_2.

In pure argon, the sonolysis of pure water leads to the homolytic dissociation of H_2O, followed by the recombination of the formed radicals to

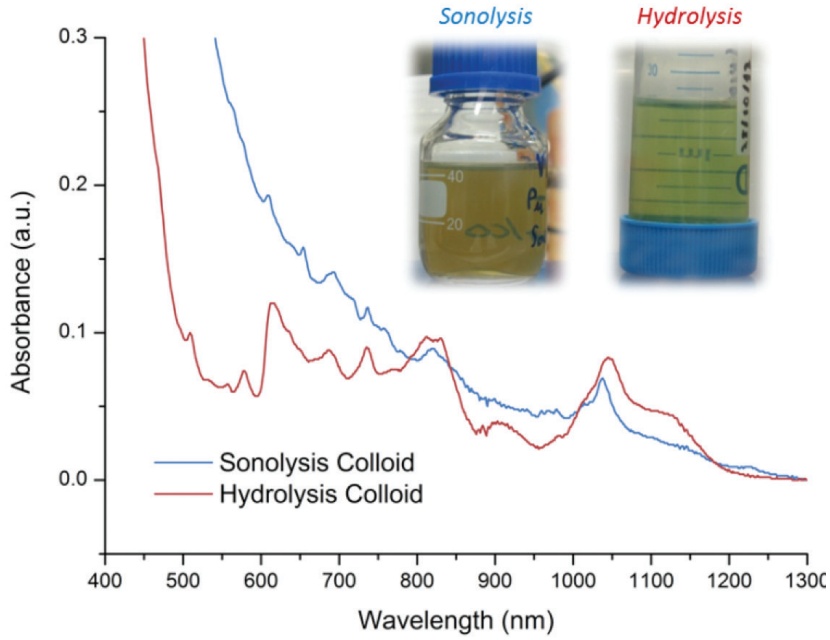

Fig. 4. This figure shows Vis-NIR absorption spectra observed for "hydrolysis" and "sonolysis" colloids. Hydrolysis colloids were obtained by diluting Pu(IV) in pure water (final concentration: $7 \times 10^{-3} - 9 \times 10^{-3}$ M). Sonolysis colloids were obtained by sonicating (20 kHz, argon, 0.34 $W.mL^{-1}$) 180 mg of PuO_2 in 50 mL H_2O (followed by centrifugation at 9000 rpm, with a final concentration of ~1.5×10^{-3} M). The insert shows the pictures of these colloids.

Further Reading

S. I. Nikitenko, L. Venault, R. Pflieger, T. Chave, I. Bisel, and P. Moisy, "Potential Applications of Sonochemistry in Spent Nuclear Fuel Reprocessing: A Short Review," *Ultrason. Sonochem.* **17**, 1033 (2010).

C. Ekberg, K. Larsson, G. Skarnemark, J. Odegaard, and I. Persson, "The Structure of Plutonium(IV) Oxide as Hydrolyzed Clusters in Aqueous Suspensions," *Dalton Trans.* **42**, 2013 (2013).

R. Pflieger, V. Cousin, N. Barré, and S. I. Nikitenko, "Sonoluminescence of Uranyl Ions in Aqueous Solutions," *Chem. Eur. J.* **18**, 410 (2012).

L. Soderholm, P. M. Almond, S. Skanthakumar, R. S. Wilson, and P. C. Burns, "The Structure of the Plutonium Oxide Nanocluster $[Pu_{38}O_{56}Cl_{54}(H_2O)_8]^{14-}$," *Angew. Chem. Int. Ed.* **47**, 298 (2008).

M. Virot, L. Venault, P. Moisy, and S. I. Nikitenko, "Sonochemical Redox Reactions of Pu(III) and Pu(IV) in Aqueous Nitric Solutions," *Dalton Trans.* **44**, 2567 (2015).

R. Pflieger, T. Chave, M. Virot, and S. I. Nikitenko, "Activating Molecules, Ions, and Solid Particles with Acoustic Cavitation," *JoVE* **86**, e51237 (2014).

C. Walther and M. A. Denecke, "Actinide Colloids and Particles of Environmental Concern," *Chem. Rev.* **113**, 995 (2013).

D. Clark, S. Hecker, G. Jarvinen, and M. Neu, in *The Chemistry of the Actinide and Transactinide Elements*, eds. L. Morss, N. Edelstein, and J. Fuger, Springer Netherlands, 2011, ch. 7, pp. 813-1264.

M. Virot, T. Chave, S. I. Nikitenko, D. G. Shchukin, T. Zemb, and H. Mohwald, "Acoustic Cavitation at the Water Glass Interface, *J. Phys. Chem. C* **114**, 13083 (2010).

Acknowledgments

The authors gratefully acknowledge Mireille Guigue, Jérôme Maurin, and Jackie Vermeulen for their help in experiments and useful discussions.

H_2 or H_2O_2. In the presence of an Ar/O_2 mixture, O_2 can react with hydrogen radicals and decrease dramatically the generation of H_2 while H_2O_2 is increased. By contrast, OH radicals may be scavenged under a CO atmosphere and thus favor the formation of H_2. The main related reactions are summarized as follows:

In pure water under Ar	*In pure water under Ar/O_2*	*In pure water under Ar/CO*
$H_2O \rightarrow))) \rightarrow H + OH^{\bullet}$	$H + O_2 \rightarrow HO_2^{\bullet}$	$HO^{\bullet} + CO \rightarrow CO_2 + H$
$H + H \rightarrow H_2$	$2HO_2^{\bullet} \rightarrow H_2O_2 + O_2$	
$HO^{\bullet} + HO^{\bullet} \rightarrow H_2O_2$		

We find that plutonium colloid formation is most likely governed by a redox mechanism and results from sonochemically induced reactions in which H_2 first reduces $Pu(IV)_s$ to $Pu(III)_l$. The local transient heating driven by bubble collapse at the solid–liquid interface possibly may activate this process. Pu(III) is then oxidized in solution by remaining $OH^{\bullet}/H_2O_2$ species, yielding Pu(IV) colloids. Although Pu(IV) colloids are generally reported as highly charged polynuclear species with coordinated anions originating from electrolyte salts, we show in this work that high-power ultrasound may provide the opportunity to prepare stable colloids without any salts or stabilizing agents, which is of paramount interest in the study of their behavior.

Conclusion

The few examples outlined in this article bring to light some of the actinide activities performed by the sonochemistry group in Marcoule. Such work demonstrates the potential and diversity of applying sonochemistry in the actinide area. Of particular interest to nuclear chemistry is the possibility of generating in situ active species without adding other chemicals. In nuclear chemistry, dilution of solutions should be avoided because of hydrolysis concerns. Sonication also contributes to the generation of smaller volumes of effluents—this is particularly attractive in nuclear reprocessing (e.g., waste amounts, concentration of feed solutions).

Experimental parameters (such as field intensity, applied frequency, carrier gases, and concentration of solutions) offer a large range of applications that could contribute to efficient and specific chemical systems. Large-scale ultrasonic devices are available today for high volumes with a huge number of potential applications, such as batch or continuous processing, multifrequencies, coupling with other techniques, and noncontact sonication. In this sense, the fundamental understanding of the acoustic cavitation and related sonochemistry has to be studied further to improve kinetics and propose future directions.

Behavior of Actinide Oxides under Extreme Environments

Cameron Tracy and Rodney Ewing
Stanford University

Maik Lang
University of Tennessee

Actinide oxides play important roles throughout the nuclear fuel cycle. Uranium is extracted from the ore minerals uraninite (UO_{2+x}) and coffinite ($USiO_4$). Nuclear reactors are typically fueled with UO_2 pellets, which are sometimes mixed with PuO_2. Many proposed waste-management scenarios involve geologic disposal of transuranic wastes in solid solution with UO_2 spent fuel. There are several advantages to the use of actinide dioxides, including their chemical stability, resistance to radiation-induced amorphization, and ability to retain the fluorite structure to very high melting temperatures.

The ubiquity of these phases in the fuel cycle means that they must perform under diverse conditions. Many of these operating environments are quite extreme in terms of temperature, pressure, and chemistry. For example, heating by radionuclide decay and actinide fission produces elevated temperatures in fuels and waste forms. The accumulation of insoluble fission gases and helium in bubbles can produce pressures of several GPa. High pressures are also encountered in geological conditions associated with the mineralogy of actinide materials and the sequestration of waste forms. In reactor accidents and long-term spent fuel storage, exposure to coolant can cause oxidation and hydration of actinide materials. To ensure the safe and efficient performance of actinide components in nuclear energy systems, we must have a thorough understanding of actinide oxide phase behavior under these extreme environments.

Highly ionizing radiation is an additional, poorly understood contributor to the phase behavior of actinide oxides. Particles with specific energies above approximately 1 MeV/atomic mass unit, including alpha particles and fission fragments, deposit tremendous amounts of energy to a nanometric volume of material along their paths. Such deposition occurs primarily through the excitation of electrons, resulting in energy densities of up to several keV/nm^3. This energy is then transferred to a material's atoms during electron relaxation, subsequently forming a damaged ion track within which atoms have been displaced from their initial sites. Although this process does not induce phase transformations or amorphization in actinide dioxides at ambient conditions, researchers have yet to determine the precise nature of the damage it causes. Furthermore, it is generally not known how irradiation in this high-energy regime affects phase behavior under the extreme environments described above.

We have recently developed techniques for the systematic exposure of actinide materials to high temperatures, high pressures, diverse chemical environments, and high-energy ion irradiation (Fig. 1a). These conditions can be applied individually or in tandem, allowing for simulation of the conditions experienced by nuclear-energy components. These techniques were developed as part of the *Materials Science of Actinides* Energy Frontier Research Center established by the Department of Energy, Office of Basic Sciences (DE-SC0001089).

Cameron Tracy discusses the behavior of actinide oxides in various extreme environments.

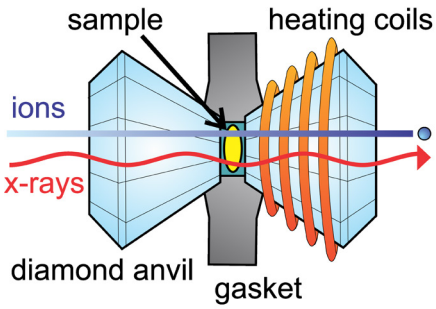

(a)

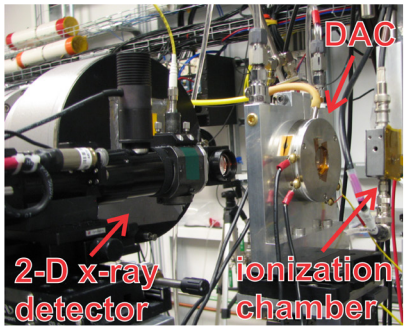

(b)

Fig. 1. (a) This illustration shows the experimental setup in which diamond anvils compress the sample chamber, which contains a pressure-transmitting medium and is safely sealed by a gasket. Resistive heating coils control the sample temperature. (b) In this photo of a synchrotron beam line, an x-ray travels from the right side, passing through an ionization chamber, the DAC, and a second ionization chamber before hitting a 2D detector. Comparing the photon counts from the ionization chambers yields absorption data. The detector records diffraction rings.

Our approach uses diamond anvil cells (DACs) to squeeze micrometer-scale samples between two ultrahard diamonds, thus generating pressures of up to approximately 70 GPa. DACs also serve to safely seal actinide samples. Various fluids can be added to the cells as pressure-transmitting media. These include water (to study hydration during coolant exposure) or inert gases (to prevent reaction with the sample).

Resistive heating allows for control of the sample temperature up to approximately 1000 K, taking advantage of the diamond anvils' high thermal conductivity. Advanced particle-accelerators can inject into the cells swift heavy ions similar in mass and energy to fission fragments. Suitable accelerator facilities include the GSI Helmholtz Centre for Heavy Ion Research in Darmstadt (Germany) and the Flerov Laboratory of Nuclear Reactions in Dubna, Russia.

These unique sample environments and containment requirements necessitate the use of advanced characterization methods because the material inside the cells is inaccessible using conventional probes. Thus, we use synchrotron x-rays in transmission mode. Such x-rays can easily penetrate the diamond anvils and deliver suitable signal intensities (Fig. 1b). X-ray diffraction (XRD) provides information on structural changes in materials, whereas x-ray absorption spectroscopy (XAS) is used to track associated changes in sample chemistry, such as the oxidation state of constituent elements. Similarly, Raman and IR spectroscopy can probe the short-range atomic arrangements of materials. These complementary techniques provide a complete picture of the mechanisms underlying phase modification in extreme environments.

We first sought to understand the specific modifications that highly ionizing radiation causes in actinide dioxides. Of particular interest was this radiation's effect on cation valence, as previous studies of fluorite-structured CeO_2 have shown that fission-fragment irradiation partially reduces the material's Ce^{4+} to Ce^{3+}. Such an effect is particularly important in the case of actinide oxides because their accessible electronic configurations and redox behavior vary dramatically across the actinide series. For example, ThO_2 exists only in this stoichiometry with tetravalent thorium, whereas UO_2 is easily oxidized to U_3O_8 or UO_3, where U is U^{6+}. PuO_2 is easily reduced to Pu_2O_3, where Pu is Pu^{3+}.

XRD results from ion-irradiated fluorite-structured dioxides (Fig. 2a) revealed two modifications: (1) angular shifts in diffraction peak positions that indicate structural expansion and (2) broadening of the peaks that indicates heterogeneous structural distortion. Comparing ThO_2 with CeO_2—an analogue of the reducible actinide oxides—revealed clear differences in damage accumulation between the two materials. In the absence of chemical changes, radiation damage in ThO_2 results from atomic displacement and the subsequent formation of crystallographic defects. In contrast, XAS results confirmed that the damage produced in CeO_2 results,

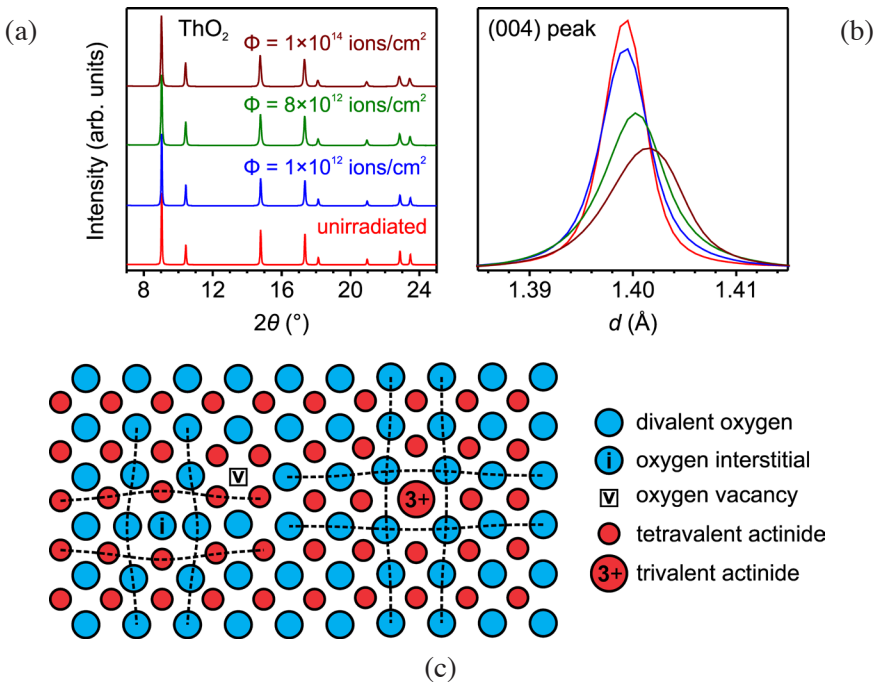

Fig. 2. The top graph (a) shows XRD data taken from irradiated ThO_2 obtained by performing azimuthal integration of imaged diffraction rings. With increasing ion fluence, the diffraction peaks shift and broaden (b). The bottom illustration (c) shows a fluorite structure viewed along the [100] direction. Shown are the two forms of radiation damage observed. In the absence of actinide valence changes, the dominant source of structural modification is the displacement of an atom to an interstitial site, leaving behind a vacancy (left side of the illustration). In materials with valence reduction, changes to ionic radii and bonding cause the same distortion and expansion (right side of the illustration).

in part, from modifications to bonding and ionic radius concomitant with cation valence reduction (Fig. 2b). In this way, the structural and chemical effects of highly ionizing radiation on actinide oxides are coupled. Thus, it is possible to predict to some extent radiation tolerance based on a material's redox behavior. This work was reported by Tracy et al. in an article titled "Redox Response of Actinide Materials to Highly Ionizing Radiation" in *Nature Communications*, January 2015.

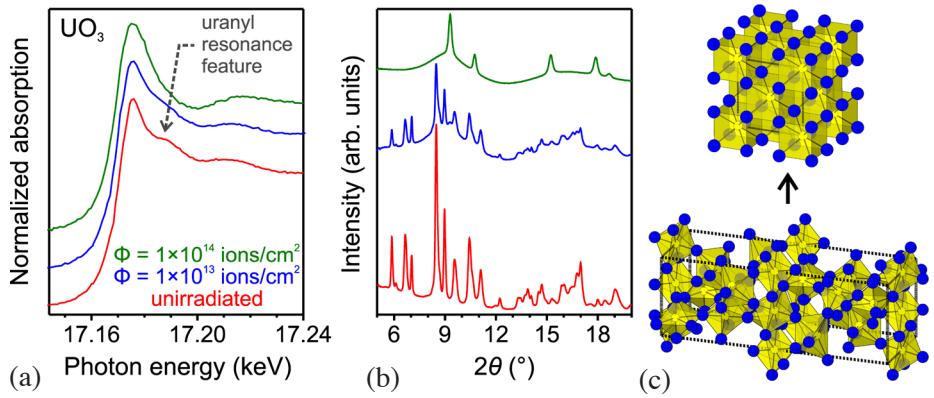

Fig. 3. The left graph (a) shows XAS spectra collected from irradiated UO_3. Increasing ion fluence attenuates the features that indicate the presence of hexavalent uranyl, with the spectra becoming characteristic of tetravalent uranium. The center graph (b) shows XRD results confirming that the γ-UO_3 phase (with octahedral uranium coordination) transforms to a fluorite-structured UO_{2+x} phase (with cubic uranium coordination). The illustration on the right (c) shows the structures of γ-UO_3 (bottom) and fluorite UO_2 (top).

These results suggest that highly ionizing radiation might strongly influence phase stability in materials with structures based on actinide elements in high oxidation states (for example, U^{6+}). Nuclear fuel exposed to water or air at high temperatures forms hexavalent uranium compounds. We simulated these conditions, producing the oxidation product γ-UO_3 and the hydration products α-$UO_2(OH)_2$ (uranyl hydroxide) and $[(UO_2)_8O_2(OH)_{12}](H_2O)_{10}$ (metaschoepite). We then irradiated these materials with swift heavy ions.

XAS results showed that U^{6+} was reduced to U^{4+} (Fig. 3). Because the structures of these compounds are based on uranyl coordination complexes, they cannot accommodate this chemical change. Thus, all three materials transformed to a fluorite-structured UO_{2+x} phase. These experiments illustrate a case in which failure to account for the chemical effects of radiation exposure could lead to erroneous predictions of actinide oxide behavior in fuel-cycle conditions.

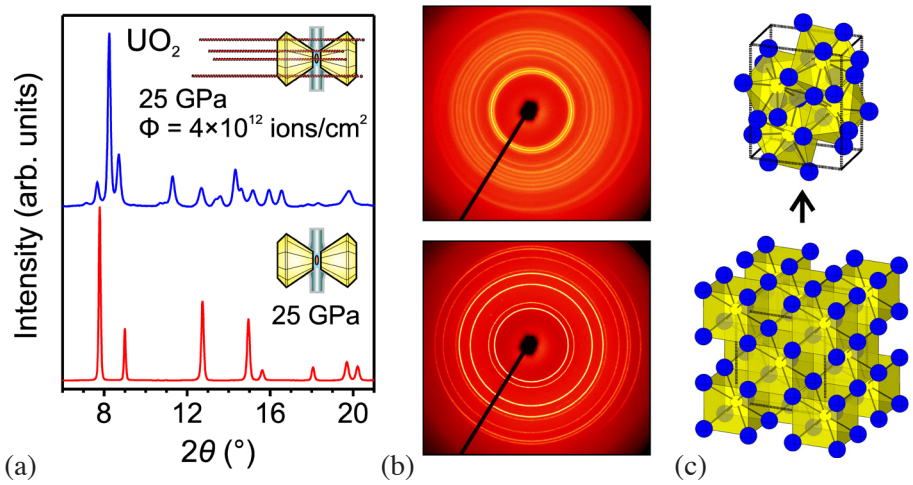

Fig. 4. The left graph (a) shows XRD patterns collected from pressurized UO_2 before and after irradiation. They indicate a transformation from the fluorite structure to the cotunnite structure. The center graphic (b) shows 2D x-ray detector images with diffraction rings, which were azimuthally integrated to yield these XRD patterns. The right illustration (c) shows fluorite (bottom) and cotunnite (top) structures determined from the XRD patterns. The transformation involves a change in uranium coordination from 8-fold to 9-fold.

Exposure to highly ionizing radiation also strongly influences the response of actinide dioxides to high pressure. Without the influence of radiation, these materials undergo a high-pressure transformation to a phase with the cotunnite structure (isostructural with $PbCl_2$). This transformation involves the motion of atoms in (111) cation planes toward adjacent anion planes. In the absence of irradiation, the onset pressure for this process is 42 GPa for UO_2.

Ionizing radiation modifies the kinetics of this atomic rearrangement through changes to bonding and anion occupancy. We observed a complete transformation to the cotunnite phase (Fig. 4) after irradiating UO_2 with swift heavy ions at approximately 25 GPa. Radiation exposure greatly extends the stability field of the high-pressure phase, thus destabilizing the fluorite structure.

These experiments make clear the pronounced effects of highly ionizing radiation on the phase space of actinide materials in extreme environments. We must better understand these effects so that we can accurately predict the performance of fuel cycle materials under such conditions.

Equilibrium Thermodynamics of Radiation Defects and Helium in the fcc 5*f* Metal

Alexey V. Karavaev, Vladimir V. Dremov, and Gennady V. Ionov
Russian Federal Nuclear Center
Zababakhin All-Russia Research Institute of Technical Physics
Snezhinsk, Russia

Brandon W. Chung
Lawrence Livermore National Laboratory
Livermore, California

Alexey Karavaev addresses the equilibrium thermodynamics of radiation defects and helium in the fcc 5f metal.

Plutonium today remains one of the most fascinating and complicated elements for theoretical and experimental study. Although plutonium does not exist in nature in large quantities, it is enormously important for the world's nuclear arsenals and in the production of energy. This element has been mass synthesized in fission reactors since the early 1940s.

Although plutonium has been around and extensively studied for more than 70 years, it continues to puzzle nuclear material scientists because of its variety of properties. Making metallurgy extremely nontrivial is the complicated low-pressure phase diagram of plutonium and its alloys. Making matters more complicated is that plutonium is a radioactive material continuously undergoing α-decay, as well as subsequent self-irradiation resulting from the high-energy decay products. Thus, self-irradiation during long-term storage—known as radioactive aging—modifies the mechanical and thermodynamic properties of plutonium and its alloys. Researchers have for the last couple of decades focused their studies on plutonium's radioactive aging process.

The self-irradiation of elemental plutonium and its alloys and compounds continuously produces radiogenic helium and leads to the primary radiation defects of crystal structure formation, their accumulation, diffusive migration in the lattice, clustering, and so on. Subjects of great importance are (1) the morphology of the point-defect cluster (i.e., equilibrium size and shape, the fraction of free and clustered defects) and (2) the interaction of the defect clusters with preexisting materials defects. Both subjects directly impact material properties, such as elastic-plastic properties, static and dynamic strength, transport coefficients, and phase stability. Atomistic simulations to date have enabled scientists to develop an estimate of the source of primary radiation defects caused by ^{235}U α-decay product nucleus in the form of localized regions extending approximately 10 nm in which 200–250 single vacancies and highly mobile interstitial atoms are produced.

The other particles produced in the α-decays are α-particles with the energy of approximately 5 MeV. These particles travel in the face-centered cubic (fcc) lattice of Pu-Ga alloys much farther away from the vicinity of the α-decay events. They produce approximately 200 additional Frenkel pairs each, lose most of their kinetic energy through electronic excitations, grab two electrons—thus closing their electronic shells, and become neutral helium atoms. These atoms occupy the nearest vacancies in the fcc lattice of Pu-Ga alloys or create and occupy vacant sites by knocking out plutonium or gallium lattice atoms that are generating interstitial atoms.

A nucleus of a helium gas bubble forms if two diffusing helium atom-vacancy complexes meet. In the late 1980s, many scientists used Transmission Electron Microscopy (TEM) to observe helium bubbles in naturally aged material. Such work ranged from simple observations and numerical calculations to observing size distribution functions and even making real-time movies of bubble migration and coalescence.

The observed average size of the helium bubbles was approximately 1.4 nm. This value, along with the helium concentration inside the bubbles (2–3 helium atoms per vacant size), remains practically the same as the material ages.

The strongly peaked distribution of bubble sizes, coupled with the nearly constant helium atom to vacancy ratio in naturally aged material, suggests there are factors that limit the growth and define the bubbles' equilibrium parameters. The purpose of this present study is to investigate the solubility of helium in the fcc lattice of δ-phase Pu–Ga alloys, use classical molecular dynamics (CMD) to determine the nature of the attractive/repulsive interactions of helium atoms with the bubbles, and discover the possible mechanism that limits bubble size and equilibrium bubble parameters (size and helium concentration—the number of helium atoms per vacant site) under ambient conditions.

The diffusive dynamics of interstitial atoms in the fcc lattice of Pu–Ga alloys is accessible by direct CMD simulations even below ambient temperatures as a result of their high mobility. However, characteristic activation energies for the motion of vacancies and helium atoms are rather high for direct CMD simulations. Consequently, diffusive migration times of vacancies and helium atoms are in the range from seconds to hours at room temperature. Such characteristics make the simulation of their dynamics impossible within a reasonable computation window.

In our present study, instead of tracking defects' dynamics we use Helmholtz free energy to evaluate the relative thermodynamic stability of metastable microconfigurations of an ideal crystal with artificially introduced systems of defects of various morphologies. To investigate a system's relative thermodynamic stability at finite temperatures, it is not sufficient to calculate and compare only the internal energies of the system's different states.

At finite temperatures, the entropy term of the Helmholtz free energy plays an important role. If it were possible to calculate the "absolute" values of free energy for the different metastable microconfigurations of a system under the same external conditions, it would also be possible to draw unambiguous conclusions about the relative thermodynamic stability of such states. Unfortunately, the absolute values of thermodynamic potentials cannot be calculated in a simple CMD simulation as an average of some quantity or expressed as a function of some averages. Such values cannot be determined using real-life experiments. However, it is possible to evaluate absolute values of free energy in the frame of CMD using the so-called thermodynamic integration method (TIM). TIM is based on a reversible quasi-equilibrium transition of a system from the state of interest to a reference state for which it is possible to calculate the free energy.

Figure 1 shows the results of the CMD calculations. Note that both the internal energy difference and the free-energy difference are negative across the entire range of helium concentrations and bubble sizes. That is, for all sizes of bubbles and all helium concentrations, both the internal and free energies of the systems gain from the joining of helium atoms to any of the bubbles. In a thermodynamic sense, it is preferable to produce configurations with a helium bubble of increased size. If a helium atom migrates in the lattice under ambient conditions, it tends to join one of the helium bubbles rather than remain a single substitutional atom in the lattice. In other words, helium atoms under ambient conditions do not dissolve in Pu–Ga alloys.

A second important feature found in Fig. 1 is the dramatic difference between the character of the internal energy surface and that of the free energy. The surface of the free-energy difference has a minimum at the point C=2.7 and R=1.1 nm, where C is the vacancy-site ratio and R is the bubble ratio. If helium atoms were to join to a helium bubble of such size and concentration, it would result in the greatest decrease in the system's Helmholtz energy. Thus, the values of C=2.7 and R=1.1 nm can be treated as estimates for the thermodynamic equilibrium parameters of helium bubbles in the Pu–3 at.% gallium fcc alloy under ambient conditions.

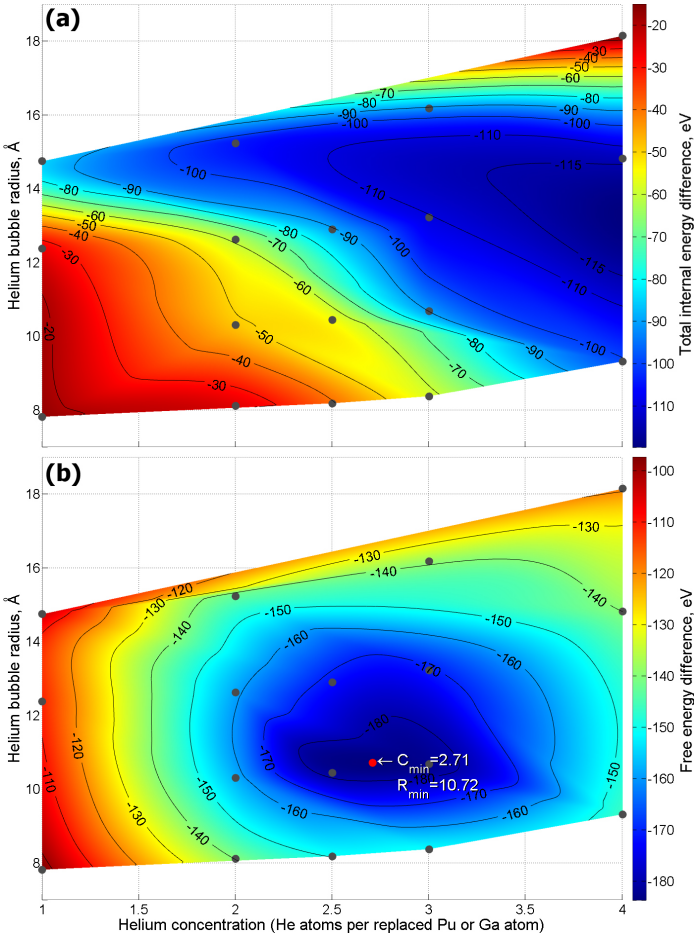

Fig. 1. These graphs show internal (a) and free-energy (b) differences between systems with all helium atoms placed in the bubbles and systems with helium bubbles and 50 additional helium atoms that are distributed away from the bubbles as a function of helium concentration (number of helium atomics per vacant site) and the size of the initial bubbles. In other words, these graphs show internal and free-energy "profit" that results from the joining of 50 helium atom-vacancy complexes in the helium bubbles of various sizes and helium concentrations.

The calculated equilibrium size is slightly higher than the experimentally observed average radius, which is of the order 0.7–0.8 nm, whereas the obtained equilibrium helium concentration value, C = 2.7, agrees well with the experimentally observed values of 2–3 helium atoms per vacant site. The chemical potential, μ, can be calculated as the derivative of the free energy with respect to the number of particles, *N*. Combining the dependence of the chemical potential, μ, and the dependence of the equilibrium helium bubble radius, *R*, on the number of particles, *N* (obtained in the simulations), we can get μ(*R*) dependence and can construct the distribution function, f(*R*), of helium bubbles with the fixed concentration C=2.7, shown in Fig. 2 as a dashed blue line, compared with an experimentally observed one (shown as bars).

As shown in Fig. 2, calculations and TEM show that overall characters of the distribution functions are quite similar. To establish greater agreement between CMD simulations with experimental data, we must continue to improve our model, incorporating real-material-structure effects and accounting for variations in helium concentration from bubble to bubble.

Vacancy defects (isolated vacancies and particularly vacancy clusters) play a significant role in the radiation damage of metals and alloys. Vacancy clusters from the displacement cascades effectively drain point defects

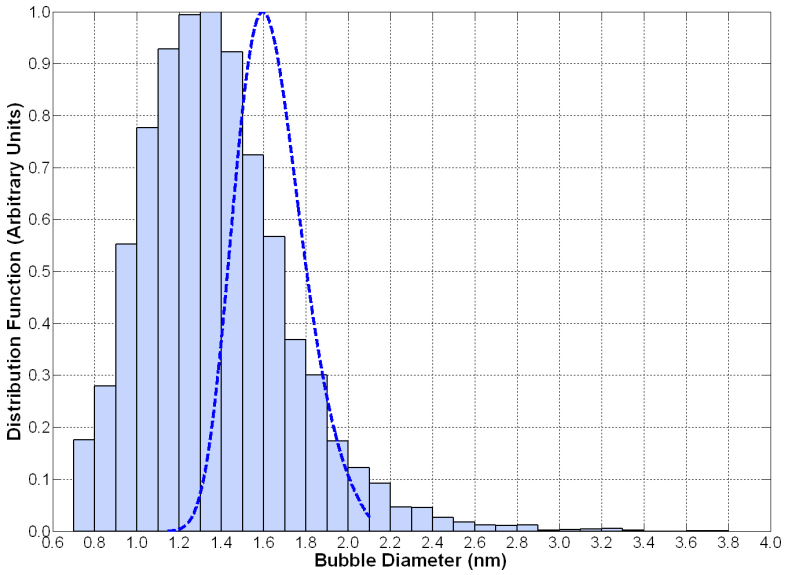

Fig. 2. This graph compares the calculated helium-bubble distribution function with a fixed helium concentration of C = 27 (dashed blue line) with an experimentally observed distribution function.

and influence the diffuse length of defect migration. Such clusters can interact with extended defects, such as dislocations and grain boundaries, thus influencing the elastic/plastic properties of the materials. As already mentioned above, a cluster can form in the vicinity of a α-decay event in a region of approximately 20×20×20 unit cells with approximately 200 vacancies. This study continues to explore the still-unknown evolution of such clusters.

Much can happen within a localized vacancy cluster. For example, if the vacancies effectively repel one another (unlikely), the cluster will gradually spread over the material and form a rarefied cloud of isolated vacancies. It is more likely that vacancies will effectively attract one another. Because they are initially localized, such vacancies are likely to form pores, which will serve as effective drains of point defects (isolated vacancies, interstitial atoms, or radiogenic helium).

Also a subject of our research is the further evolution of pores, their equilibrium sizes, their geometry, etc. In principle, heat may cause vacancy clusters to dissociate, thus becoming a source of isolated vacancies. If there are internal stresses, the pores may collapse. Such collapses can generate, for example, stacking faults or dislocation loops. Some pores may be filled with radiogenic helium, which is known to be present in the material in the form of bubbles. In the paragraphs that follow, we will attempt to explain some of these phenomena.

We begin with our investigation regarding the nature of the interaction between vacancies in the fcc lattice of Pu-Ga alloys at the ambient conditions. Our principal concern is whether such vacancies would repel each other or would instead mutually attract each other. To address this concern, we used TIM to calculate the internal and free energies of the Pu-Ga alloy samples, with 200 vacancies added in the form of "spherical clouds" with 3D Gaussian random distribution of the vacancies of different width. As a reference state, we took a system in which 200 vacancies were randomly and uniformly distributed in the entire sample that corresponds to a maximum average distance between them. Additional calculations were performed for the system with a regular "spherical pore," generated by removing 200 atoms nearest to the sample's center.

Figure 3 shows the calculated dependence of the internal and Helmholtz free energies on the width of the Gaussian-like distribution. The figure shows that under the ambient conditions there exists an effective attraction between the vacancies. Moreover, vacancy clustering is favorable with respect to internal energy and Helmholtz free energy, a criterion for thermodynamic stability. If the vacancies attract one another, their diffusive motion should lead to pore-formation in the bulk of the material, so long as there are no other drains (e.g., extended defects of crystal structure such as dislocations or grain boundaries).

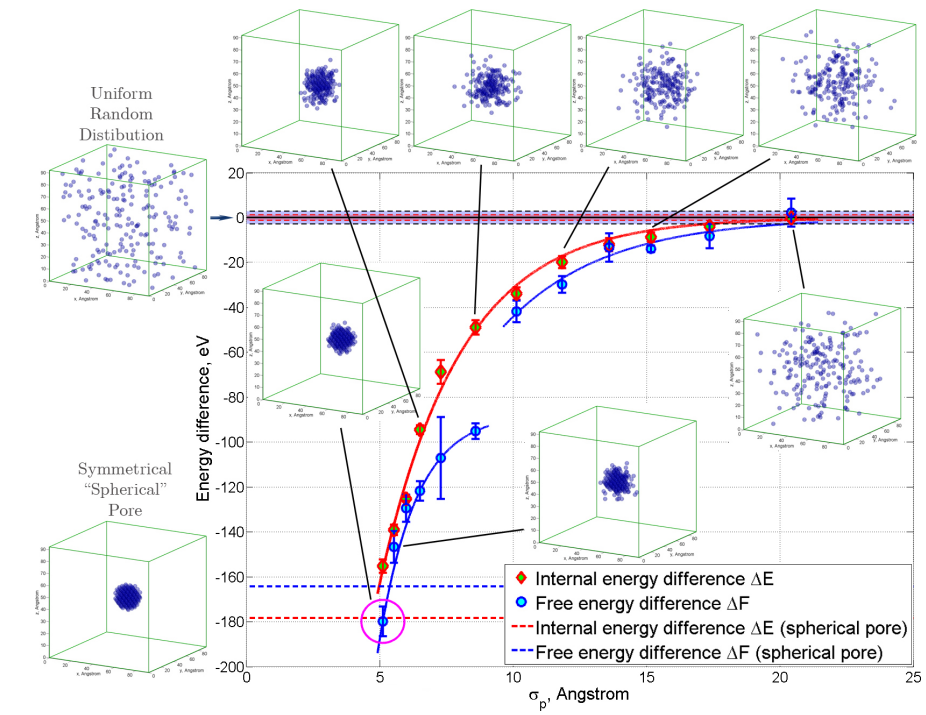

Fig. 3. This figure shows the dependence of the internal E and free F energies of 200 vacancies on the size of the vacancy "cloud." Zero energy corresponds to uniform random distribution of 200 vacancies in the samples. Red and blue horizontal dashed lines represent internal and free energies of the system, with a "spherical" pore made by removing of 200 atoms nearest to the center of the sample. Red diamonds and blue circles represent internal and free energies of systems with 3D Gaussian-like random distribution of 200 vacancies of various width σ.

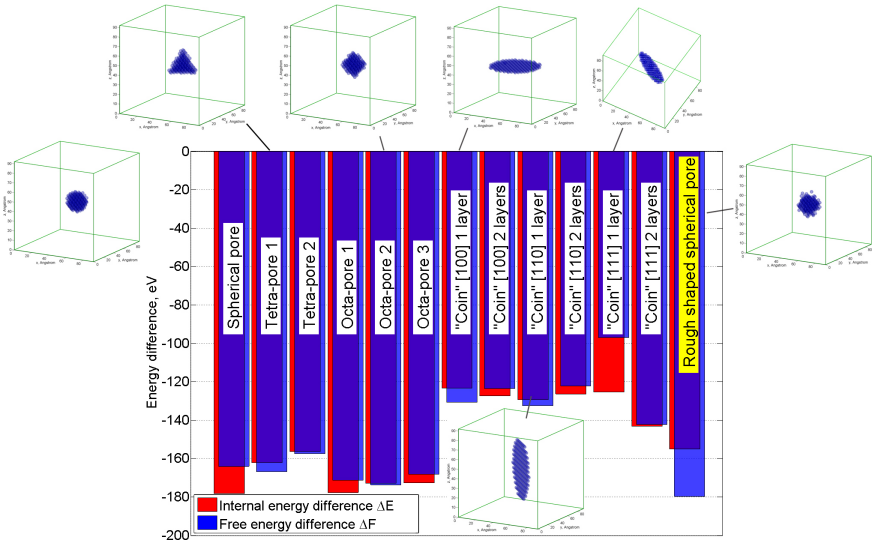

Fig. 4. This figure compares internal and free energies of a system with differently shaped pores of 200 vacancies. Zero values correspond to the system in which the vacancies are randomly and uniformly distributed over the entire sample.

The next part of our investigation involved calculating and comparing internal and free energies of the systems with 200 vacancy pores of different shapes. Such shapes included voids shaped like tetrahedra and octahedra of different orientations with respect to the crystal axis and coin-like cavities of 1 and 2 monoatomic layers parallel to the crystallographic planes [100], [110], and [111]. Figure 4 shows a histogram of calculated values of internal energy E and free energy F for systems with differently shaped pores of 200 vacancies.

As the origin, we used energies of the system with uniformly distributed 200 vacancies. Of all the configurations considered, the spherical pore has

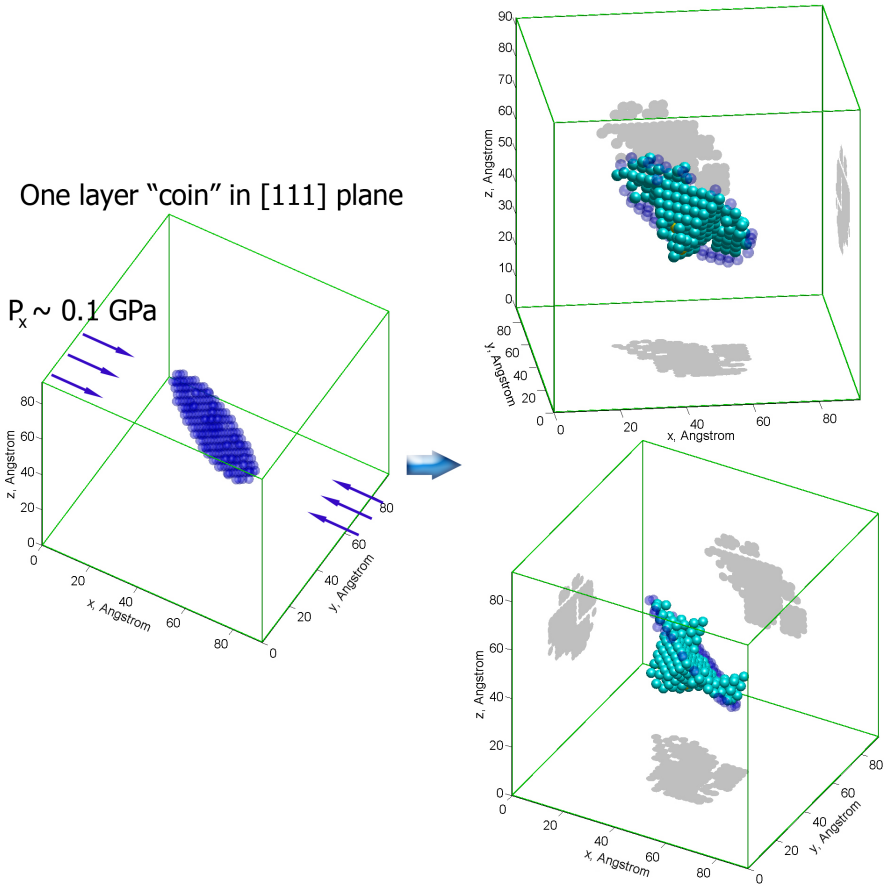

Fig. 5. This figure shows one layer in a [111] plane coin-pore of 200 vacancies (left) collapsing into a system with stacking-fault tetrahedral (right) under uniaxial pressure. Blue semi-transparent spheres represent residue after the collapse vacancies. Cyan spheres represent plutonium and gallium atoms in stacking fault positions.

the lowest internal energy *E* because of its lowest specific surface. Octa-pores are more favorable with respect to the free energy as a result of the discrete structure and the crystal's fcc symmetry. The planar coin-like structures under these conditions appear energetically and thermodynamically unprofitable compared with compact 3D pores. A spherical pore with a randomly disordered surface was found to have the lowest free energy *F*. Hence, it was the most thermodynamically stable.

Applying a relatively small uniaxial stress (~0.1 GPa) in the <100> direction to the system with a coin-shaped pore of one molecular layer in the [111] plane caused the pore to collapse and form a system of stacking fault tetrahedra (SFT) of different sizes. Figure 5 shows this system of residual defects after the stress release and relaxation. After the stress relaxation, the free energy *F* of the system with these defects appeared to be lower than that of the initial system with the coin pore. However, the free energy *F* was still approximately 20 eV higher than the free energy of the system with the roughly shaped spherical pore. Of all the considered pores of 200 vacancies in the bulk of the fcc crystal of Pu-Ga alloys, we found that the spherical pore obtained by removing 200 atoms closest to the center of the sample has the lowest internal energy *E*. The pore that had the lowest Helmholtz free energy *F* was the spherical pore with the randomly disordered surface.

Quite natural for fcc materials is the transformation under the stress of the disk of vacancies in the [111] plane (in essence, the Frank loop) into the system of SFTs. It is well known that SFTs are dominant configurations of vacancy clusters in many fcc metals with relatively low stacking fault energies. On the other hand, the CMD calculation demonstrates that at the ambient conditions for all the sizes of vacancy clusters, it is the compact voids that are favored over the SFTs in internal energy and in thermodynamics. According to the results of our CMD calculations under ambient conditions, we found that if vacancy clusters formed in the bulk of the material, they would take the form of a compact spherical void rather than an SFT. This result has indirect experimental confirmation.

We were unable to find any report of experimental observation of SFTs in gallium-stabilized δ-phase plutonium in spite of long history of TEM observations of plutonium and its alloys since the late 1960s. This means that the SFTs do not form in Pu-Ga alloys under ambient conditions or they are too small for us to identify them using TEM microphotographs.

If we calculate the equilibrium void size using a similar method used for helium bubbles, we find that the equilibrium void size in the fcc lattice of Pu-Ga alloys is approximately 325 vacancies (~2 nm in size pore). The existence of the equilibrium void size with minimal chemical potential limits void growth within the lattice. According to our CMD calculations, there should be no swelling in the material, which is in accordance with long-term observations of the δ-phase Pu-Ga alloys.

However, the picture changes if we take into account the real structure of the material—namely, the presence of dislocations. CMD simulations demonstrate that voids formed on dislocations are more thermodynamically preferable than that in the bulk of the fcc lattice, and that the dislocations in the Pu-Ga alloys are effectively drained of vacancies. The most thermodynamically stable formation of vacancy cluster on the dislocations consists of a nearly spherical void with a thermodynamically equilibrium size of approximately 110 vacancies Fig. 6.

According to our CMD calculations, the formation of small (nanometer) pores on the edge dislocations is the most thermodynamically preferable mechanism of the vacancy cluster evolution. The nanometer pores seated on the dislocations cause pining of them, leading to an impediment of the

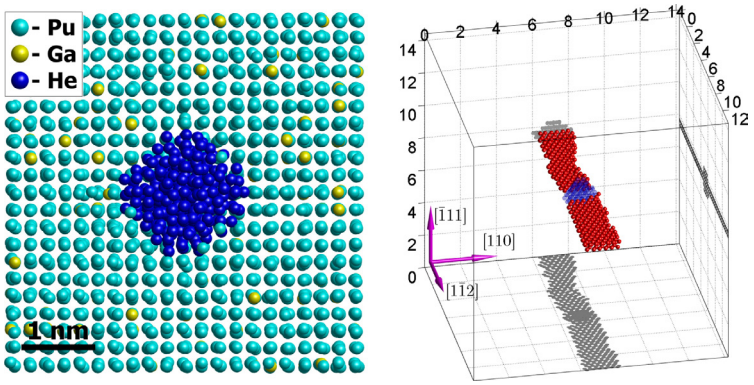

Fig. 6. The figure on the left shows thermodynamic equilibrium under ambient conditions, with a helium bubble in the fcc lattice of a Pu-Ga alloy of 205 atoms with a helium atom to a vacant-site ratio of C≈2.7. The figure on the right shows thermodynamic equilibrium under ambient conditions with a void of 110 vacancies seated on the edge dislocation. The scale here is in nanometers. Red spheres represent plutonium and gallium atoms of the stacking fault area bounded by partial dislocations. Blue spheres represent vacancies. Not shown is the host fcc lattice.

Acknowledgments

The work was partially performed through a collaboration authorized under Contract No. B593480 between the Russian Federal Nuclear Center—Zababakhin Institute of Technical Physics and Lawrence Livermore National Laboratory.

dislocation sliding. The latter effect causes, for example, an increase in static yield stress with the material's age, which is observed in experiments.

Based on CMD simulations used to calculate thermodynamic potentials and determine the relative thermodynamic stability of various microconfigurations of defects, we conclude that TIM is an effective tool to study thermodynamics and predictions of the behavior of lattice defects whose dynamics are inaccessible by using direct CMD modeling. Our approach provides insightful answers to important materials science questions, such as the following: Why is there no observed swelling in the δ-phase Pu-Ga alloys? What controls the equilibrium size and helium concentration in helium bubbles? What increases of the static yield stress and ultimate tensile strength of the aged material?

Actinide Research Quarterly

Actinide Research Quarterly (ARQ) is published by Los Alamos National Laboratory and is a publication of the Glenn T. Seaborg Institute for Transactinium Science, a part of the National Security Education Center. ARQ highlights research in actinide science in areas such as process chemistry, metallurgy, surface and separation sciences, atomic and molecular sciences, actinide ceramics and nuclear fuels, characterization, spectroscopy, analysis, and manufacturing technologies.

LA-UR-16-28436

Address correspondence to

Actinide Research Quarterly
c/o Editor
Mail Stop T-001
Los Alamos National Laboratory
Los Alamos, NM 87545

ARQ can be read online at

www.lanl.gov/arq

If you have questions, comments, suggestions, or contributions, please contact the ARQ staff at
arq@lanl.gov or (505) 665-0858

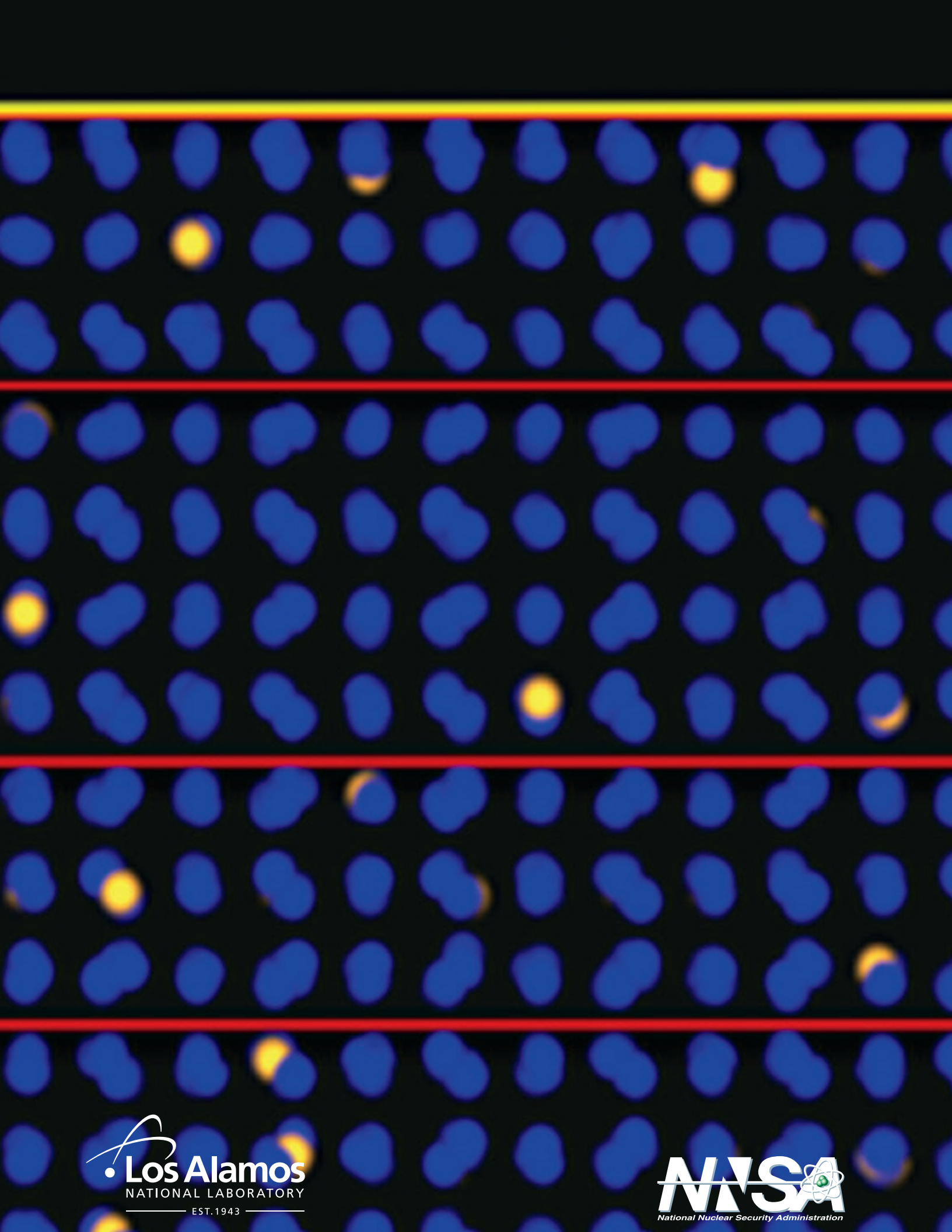

Los Alamos
NATIONAL LABORATORY
EST. 1943

NNSA
National Nuclear Security Administration